Bulletin of The Marine Geology

Volume 37, No. 1, June 2022

ISSN : 1410 - 6175

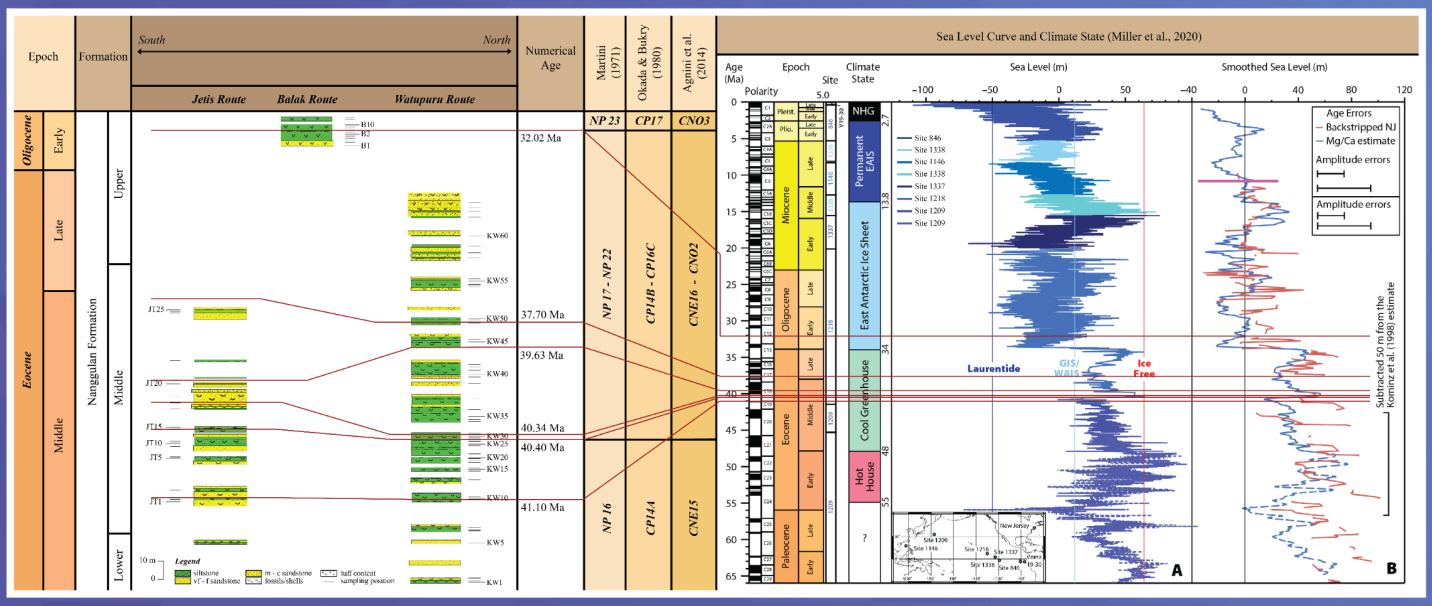

MARINE GEOLOGICAL INSTITUTE
GEOLOGICAL AGENCY
MINISTRY OF ENERGY AND MINERAL RESOURCES

BALAI BESAR SURVEI DAN PEMETAAN GEOLOGI KELAUTAN
BADAN GEOLOGI
KEMENTERIAN ENERGI DAN SUMBER DAYA MINERAL

Bull. of The Marine Geology	VOL. 37	NO. 1	Page 1 - 55	BANDUNG June 2022	ISSN 1410 - 6175

Accredited :
National Research and Innovation Agency
200/M/KPT/2020

BULLETIN OF THE MARINE GEOLOGY

Vol. 37, No. 1, June 2022

INSURED EDITOR

Director of Marine Geological Institute

CHIEF OF EDITORIAL BOARD

Dr. Luli Gustiantini, S.T., M.T.

VICE CHIEF OF EDITORIAL BOARD

Imam Setiadi, S.Si., M.T.

EDITORIAL BOARDS

Siti Marina, S.T., M.Phil. *(Marine Geological Institute of Indonesia)*
Yulinar Firdaus, S.Si., M.T. *(Marine Geological Institute of Indonesia)*
Nazar Nurdin, S.T., M.T. *(Marine Geological Institute of Indonesia)*
Andrian Wilyan Djaja, S.Si., M.T. *(Marine Geological Institute of Indonesia)*
Sony Mawardi, S.T. *(Marine Geological Institute of Indonesia)*
M. Andri Syahrir, S.T. *(Marine Geological Institute of Indonesia)*
Dra. Ai Yuningsih *(Marine Geological Institute of Indonesia)*
Shaska Ramadhan Zulivandama, S.T., M.T. *(Marine Geological Institute of Indonesia)*
Dr. rer. Nat. Maria Sekar P., M.Sc., S.T. *(Bandung Institute of Technology)*
Tumpal B. Nainggolan, S.T., M.T. *(National Research and Innovation Agency)*
Dr. Eng. Budi Muljana, S.T., M.T. *(Padjajaran University)*
Dr. Ir. Noor Cahyo Dwi Aryanto, M.T. *(National Research and Innovation Agency)*

SCIENTIFIC REVIEWERS

Dr. Emma Rochima, S.Pi., M.Si. *(Padjajaran University)*
Dr. Rully Setiawan *(Centre for Geological Survey)*
Rendy, S.T., M.Eng. *(Trisakti University)*
Dr. Ir. Khoiril Anwar Maryunani, M.T. *(Bandung Institute of Technology)*
Syamsurijal Rasimeng, S.Si., M.Si. *(Lampung University)*

PUBLISHER BOARDS

Ir. Immaculata Christiana, M.T.
Drs. Judy Muliawan Eddy
Dery Rochiman, A.Md.
Dwinanda Pratya Annisa M., S.pd.
Nanang Suryana

GRAPHIC DESIGN

Arif Suprayitno, S.Kom., M.Kom.

For communication of this publications, please contact :
MARINE GEOLOGICAL INSTITUTE
Dr. Junjunan 236, Bandung-40174, Indonesia
Telephone : +62-22-6032020, 6032201, Fax : +62-22- 6017887
E-mail : ejournal.p3gl@gmail.com

Cover Figure : Correlation between the Nanggulan Formation's depositional history and the globalsea-level curve (by : Jatiningrum 2022)

Preface

This is the first edition since the restructuring of our institute, the Marine Geological Institute (MGI). Rest assured, our Bulletin of the Marine Geology still complies with its purpose of sharing knowledge between scientists, academicians, practitioners, and others who have an interest in the improvement of marine science and technology.

Without further ado, we are pleased to present the first edition of the year 2022, which includes valuable knowledge derived from the following five papers: Multi-Model Variation of the Enhanced Asian Rainfall and Continent-Ocean Thermal Gradient from Pre-Industrial to Mid-Holocene, a research partnership between Earth Science Study Program, Faculty of Earth Sciences and Technology, Institut Teknologi Bandung (ITB) and the National Research and Innovation Agency (BRIN); the second paper, entitled Ash Layers from South Andaman Sea: Probably Sourced from Toba Caldera, presented by the Geological Survey of India; the third title of Sedimentation Rates and Calcareous Nannofossil Biostratigraphy of Nanggulan Formation, Kulon Progo, Indonesia, a collaboration project between Geological Engineering Program Study, Faculty of Exploration and Production Technology, Pertamina University and Akita University, as well as PT Geoservices; a contribution from BRIN under a title of Marine Geomagnetic Anomalies Belt and its Relationship to the Remnant Tectonic-Arc in the North-western Java Sea-Indonesia, listed as the fourth; and last but not least, a paper of Pb Ratio Analysis of Foraminifera to Observe Paleoceanographic Changes during Holocene in Arafura Sea yielded by MGI and Faculty of Geological Engineering, Padjadjaran University, teaming with BRIN and Korea Institute of Ocean Science and Technology (KIOST).

The editors wish to express their appreciation for everyone's outstanding contributions to this edition, especially those made by the authors. Readers will undoubtedly find their work to be exceptional after learning about their expertise in marine research. Let's create harmony with nature.

Chief of Editorial Board

ISSN 1410-6175

BULLETIN OF THE MARINE GEOLOGY

Vol. 37, No. 1, June 2022

CONTENTS

MULTI-MODEL VARIATION OF THE ENHANCED ASIAN RAINFALL AND CONTINENT-OCEAN THERMAL GRADIENT FROM PRE-INDUSTRIAL TO MID-HOLOCENE

VARIASI MULTI-MODEL PADA PENINGKATAN HUJAN ASIA DAN GRADIEN SUHU BENUA-LAUT DARI PRA-INDUSTRI SAMPAI HOLOSEN TENGAH

Adinda Maharani[1*], Yudha Setiawan Djamil[2], Rima Rachmayani[3]

[1] Program Studi Sains Kebumian, Fakultas Ilmu dan Teknologi Kebumian Institut Teknologi Bandung (ITB), Jl.Ganesha No.10, Bandung, Jawa Barat, Indonesia

[2] Pusat Riset Iklim dan Atmosfer (PRIMA), Badan Riset dan Inovasi Nasional (BRIN), Jl. Dr. Djunjunan No. 133, Bandung, 40173, Indonesia

[3] Kelompok Keahlian Oseanografi, Fakultas Ilmu dan Teknologi Kebumian, Institut Teknologi Bandung (ITB),Jl.Ganesha No.10, Bandung, Jawa Barat, Indonesia

*Corresponding author: adndamahrani@gmail.com

(Received 30 May 2022; in revised from 30 May 2022; accepted 25 August 2022)

DOI : 10.32693/bomg.37.1.2022.762

ABSTRACT : Rainfall over the Asian continent during the mid-Holocene was higher than today as shown by the rainfall proxy records. During the mid-Holocene, increased rainfall over the Asian Continent has been suggested to be associated with the strengthening of the Asian Summer Monsoon (ASM) following a sharper continent-ocean thermal gradient. This study examined multi-model variation between changes of the continent-ocean thermal gradient and the increased rainfall over Asia during the mid-Holocene as compared to the pre-Industrial. We analyzed surface temperature, precipitation, and wind at 850mb from nine Global Climate Models (GCMs) which are all obtained from the database of the Paleoclimate Modeling Intercomparison Project Phase-3 (PMIP3). Multi-model analysis shows that changes in a continent-ocean thermal gradient has a positive correlation with ASM wind. However, a negative correlation occurs between changes in the continent-ocean thermal gradient with Asian rainfall. Models that simulate large changes in the continent-ocean thermal gradient produced the smallest increase in the Asian rainfall and vice versa. Such inverse relation is likely due to the cooling of Indian Ocean SST since its correlation scores with Asian rainfall is much higher than the one with the warming of the Asian continent. Thus, multi-model variation of the increased rainfall over the Asian continent between mid-Holocene and today is mainly related to the multi-model variation of the cooling in the Indian Ocean SST.

Keywords: Asian Summer Monsoon, Indian Ocean, Multi-model, Sea Surface Temperature, PMIP3

ABSTRAK*: Curah hujan di benua Asia selama Holosen Tengah mengalami peningkatan dibandingkan masa sekarang berdasarkan catatan proksi curah hujan. Selama Holosen Tengah, peningkatan curah hujan di Benua Asia diduga berhubungan dengan penguatan fenomena Muson Asia (ASM) di musim panas yang diakibatkan oleh gradien suhu benua-laut yang meningkat. Studi ini mengkaji variasi multi-model antara perubahan gradien suhu benua-laut dan peningkatan curah hujan di Asia saat Holosen Tengah dibandingkan dengan era Pra-Industri. Parameter yang dianalisis adalah suhu permukaan, curah hujan, dan angin 850mb dari sembilan Global Climate Models (GCMs) yang diperoleh dari database Paleoclimate Modeling Intercomparison Project Phase-3 (PMIP3). Analisis multi-model menunjukkan bahwa perubahan gradien suhu benua-samudera memiliki korelasi positif dengan angin ASM. Namun, korelasi negatif terjadi antara perubahan gradien suhu benua-laut dengan curah hujan Asia. Model yang mensimulasikan perubahan terbesar dalam gradien suhu benua-laut menghasilkan peningkatan terkecil dalam curah hujan Asia dan sebaliknya. Hubungan terbalik tersebut kemungkinan disebabkan oleh pendinginan SPL di Samudera Hindia karena skor korelasinya dengan curah hujan Asia jauh lebih tinggi dibandingkan dengan korelasi antara peningkatan hujan dengan pemanasan benua Asia. Dengan demikian, variasi multi-model dari peningkatan curah hujan di benua Asia antara pertengahan Holosen dan masa kini utamanya terkait dengan variasi multi-model dari pendinginan SPL di Samudra Hindia.*

Kata Kunci: *Asian Summer Monsoon, Indian Ocean, Multi-model, Suhu Permukaan Laut, PMIP3*

INTRODUCTION

Mid-Holocene, a period around six thousand (~6,000) years ago (ka), is known as a period with a maximum warm climate phase (Yafeng et al., 1993). During mid-Holocene, increased insolation occurred in the northern hemisphere during boreal summer as compared to the Holocene period (Berger, 1978). The increased insolation strengthened the Asian Summer Monsoon (ASM), which is one of the most fundamental phenomena in the global circulation of the atmosphere (Braconnot et al. 2000; Cheng et al. 2021; Joussaume et al. 1999; Wang and Fan 1999; Zhao et al. 2005). ASM affects the climate in the Asian continent due to the heat and moisture transfer from the ocean to the continent at high latitudes (Chen et al., 2008). ASM is associated with rainfall in the Asian continent, due to the large-scale transport of water vapor from Indian Ocean to Asian Continent (Ding & Chan, 2005; Ohgaito & Abe-ouchi, 2007).

ASM has been suggested to be stronger in the mid-Holocene than today (Rawat et al., 2021). Previous studies on rainfall proxy during the Holocene have suggested that the increased rainfall in Asia during mid-Holocene was due to changes in the interhemispheric thermal gradient during the boreal summer (Cheng et al. 2016a). Moreover, the paleo isotope records of oxygen and deuterium showed increased rainfall in southern and northern China (Rao et al., 2016). Additionally, some pollen and microfossil data revealed an intensified rainfall in most of China (Bartlein et al., 2011). During the mid-Holocene, in northern China, the peak rainfall occurred during boreal summer as indicated by sediment core record of Hulun Lake and Daihai Lake (Wen et al., 2010; Xiao et al., 2009).

In addition to proxy records, numerical simulations were carried out to describe ASM and rainfall conditions in Asia during the mid-Holocene. Wetter-than-today ASM is well-simulated by the Paleoclimate Model Intercomparison Project Phase-2 (PMIP2), which exhibited an enhanced rainfall of East Asia during boreal summer in the mid-Holocene, compared to that of the pre-Industrial (Dallmeyer, 2011; Tao et al., 2010). This is in line with the other simulations of PMIP2, which show rainfall intensification of China during boreal summer in the mid-Holocene by 10.5% than today (Jiang et al., 2013). Thus, model study under PMIP has revealed that the ASM during the mid-Holocene was stronger and wetter than today.

During the mid-Holocene, proxy records and model simulations indicate intensification of ASM and rainfall in Asia as a respond to the enhanced insolation in the northern hemisphere. The increase insolation raises the Asian surface temperature (Polanski et al., 2012). Rising Asian surface temperature changes the thermal gradient between Asian continent and Indian Ocean (Cheng et al. 2016a; Wohlfahrt et al, 2004). Previous studies verified that changes in the inter-hemispheric thermal gradient, lead to a higher rainfall in the northern hemisphere (Schneider et al., 2014). Thus, the difference in the surface temperature gradient in Asian continent and Indian Ocean between during mid-Holocene and today is expected to change the magnitude of ASM.

Many numerical studies were done to understand the mechanisms of the increased Asian rainfall between mid-Holocene and today (Dallmeyer et al., 2011; Hewitt & Mitchell, 1996; Ren et al., 2021; Tao et al., 2010). However, study on multi-model variation (multi-model analyses), in terms of physical quantities associated with stronger-than-today ASM during the mid-Holocene, has not been conducted. Multi-model analysis has been previously used to analyze the general relationship between climate seasonality and ENSO on several paleoclimate scenarios (Emile-Geay et al., 2015). Therefore, the aim of our research is to analyze the multi-model variation from the output of GCMs involved in PMIP3, regarding the shifting impacts in the continent-ocean thermal gradient to the Asian rainfall enhancement between mid-Holocene and pre-Industrial scenarios. This study consists of several sections. Detail specifications of GCM and the methods are described under the section 2. Moreover, Section 3 displays the result from the changes among the physical parameters and their correlations during the mid-Holocene. Section 4 discusses relationship between all physical parameters with suggested mechanisms. Additionally, Summary and conclusions are defined in Section 5. Every section is explained below.

METHODS AND MATERIAL

Data

This study compared simulation output from 9 GCMs based on the mid-Holocene and pre-Industrial climate scenarios. Mid-Holocene scenario is mainly defined by a stronger-than-today insolation in the northern hemisphere during boreal summer (Berger, 1978). Pre-Industrial scenario is a period before industrial revolution (~1850) when the climate was not yet influenced by the rising concentration of greenhouse gases from fossil fuels or known as the anthropogenic forcing (Mahowald et al., 2006). These simulations are part of the Paleoclimate Model Intercomparison Project - Phase 3 (PMIP3), which their output is openly accessible in a website administered by the German Climate Computing Center (cera-www.dkrz.de). The 9 GCMs are BCC-CSM1, CCSM4, CESS FGOAL-S2, CSIRO MK-3-6-0, IPSL-CM5A-LR, MPI ESM-P, MIROC ESM, MRI-CGCM3, and NASA GISS-E2. Physical quantities used in this study are monthly rainfall, surface temperature, and horizontal (zonal and meridional) wind at 850mb. General specification of each GCM is described in Table 1.

Methodology

Stronger-than-today insolation on the northern hemisphere during the mid-Holocene is known to strengthened continent-ocean thermal gradient, ASM wind, and Asian rainfall following the northward

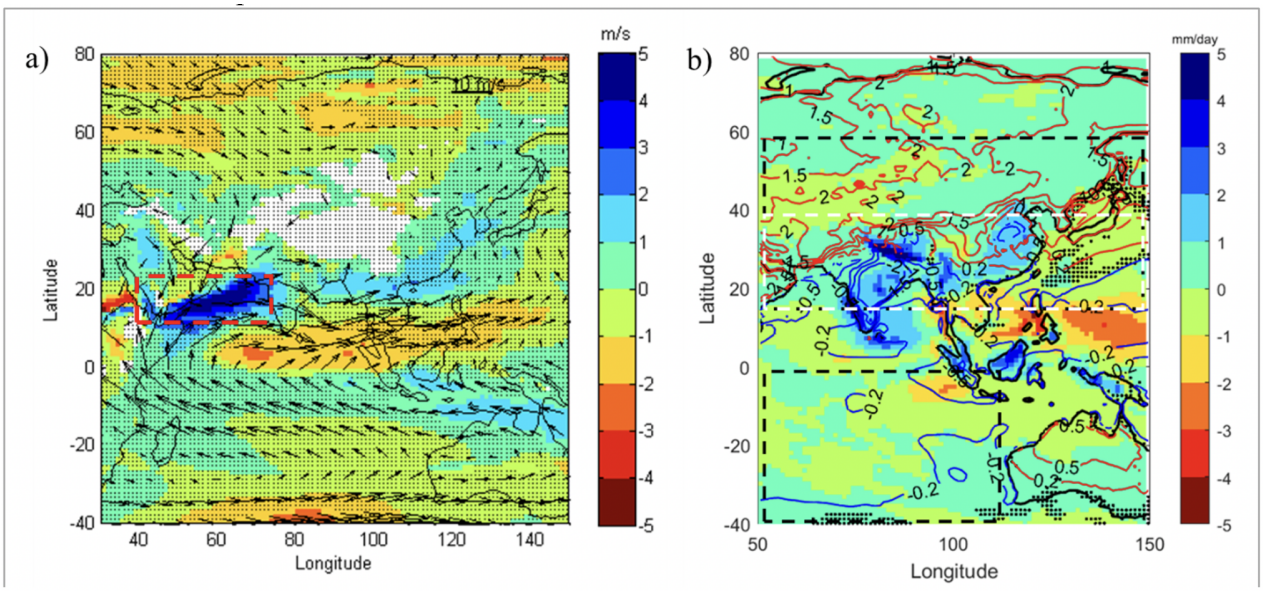

Figure 1. Seasonal mean of (a) the wind magnitude (shaded colour, in m/s) and direction (arrow), (b) the rainfall (shaded color, in mm/day) and surface temperature (contour, in K) during boreal summer for the mid-Holocene minus pre-Industrial simulations by the MRI-CGCM3. Contours in red and blue represent positive and negative changes in temperature respectively. Dotted areas are not significant at 95% confidence level for the rainfall change. Red dashed rectangles are areas to calculate area-averaged of ASM wind, black dashed rectangles are areas to calculate area-averaged of surface

Table 1. General description of the nine GCMs involved in this study. All models are part of the PMIP3 which their simulation output are freely accessible in cera-www.dkrz.de. (https://wiki.lsce.ipsl.fr/pmip3/doku.php/pmip3:database:status).

Model name	**Country**	**Number of horizontal grid and vertical layers**	**Length of simulation per-scenario (Year)**		**Cite**
			pre-Industrial	**mid-Holocene**	
BCC-CSM1	China	128 x 64 x L21	1500	100	(Wu & Xin, 2015)
CCSM4	USA	288 x 192 x L26	1503	903	(Otto-Bliesner, 2014)
CESS FGOALS-S2	UK	192 x 145 x L38	30	30	(LASG 2015)
CSIRO MK-3-6-0	Australia	64 x 56 x L1	1353	153	(Jeffrey et al., 2016)
IPSL-CM5A-LR	Prancis	96 x 95 x L39	2703	1203	(Braconnot et al., 2016)
MIROC ESM	Japan	36 x 43 x L40	277	243	(JAMSTEC et al., 2015)
MPI ESM-P	Japan	196 x 98 x L47	603	273	(Jungclaus et al., 2012)
MRI-CGCM3	Japan	364 x 160 x L48	1203	273	(Yukimoto et al., 2015)
NASA GISS-E2-R	USA	40 x 60 x L40	63	63	(NASA 2014)

migration of Inter-tropical Convergence Zone (ITCZ) in orbital time-scale (Schneider et al., 2014; (Tapio Schneider et al., 2014)Rawat et al., 2021). Changes of all three parameters during boreal summer are defined as the differences in their mean between the two climate scenarios (mid-Holocene minus pre-Industrial) during June, July and August (JJA). The seasonal mean during boreal summer is calculated based on the area averaged within 50E – 150E, 20N-60N for Asian surface temperature, 40E – 70E, 10N-20N for ASM wind, 50E – 150E, 20N-40N for rainfall, and 50E - 150E, 0 – 40S for Indian Ocean SST (Figure 1a & 1b). All these areas are chosen since significant changes relative to its surroundings have been identified. The ASM wind intensity for our study is based on the low-level wind at 850mb since it is also used by the Indian Monsoon index (Wang and Fan, 1999; Wang et al., 2001).

The differences (Δ) between the mid-Holocene (*mH*) and pre-Industrial (*piC*) simulations for the seasonal mean of the surface temperature between Asian Continent and Indian Ocean ($\partial\Delta T$), the ASM wind (ΔAm_{as}) and rainfall over the Asian Continent (ΔP_{as}) are define as follow:

$$\Delta T_{oc} = T_{oc\_mH} - T_{oc\_piC} \quad (1)$$

$$\Delta T_{as} = T_{as\_mH} - T_{as\_piC} \quad (2)$$

$$\partial\Delta T = \Delta T_{as} - \Delta T_{oc} \quad (3)$$

$$\Delta AM_{as} = AM\_mH - AM\_piC \quad (4)$$

$$\Delta P_{a\,s} = P_{as}\_mH - P_{as}\_piC \quad (5)$$

Where T_{oc} and T_{as} are the seasonal mean of the Indian Ocean SST and Asian continent surface temperature, respectively.

Seasonal mean changes of all the above parameters are compared to each other in order to check the consistency of the multi-model variation to the coherency of these parameters as previously suggested (Schneider et al., 2014; Rawat et al., 2021). For example, models with much (less) sharper continent-ocean thermal gradients are hypothesized to produce stronger (weaker) ASM wind and higher (lower) Asian rainfall. Thus, multi-model variations of these comparisons are quantified by calculating linear regressions and Pearson's correlation scores.

RESULTS

Multi-model variation in terms of relationship between continent-ocean thermal gradient (∂ΔT) with Asian monsoon wind (ΔAMas), as well as with continent-ocean thermal gradient is displayed in Figure 2(a). On the other hand, the relationship between continent-ocean thermal gradient and Asian monsoon wind with Asian rainfall presented in Figure 2(b) and 2(c). Continent-ocean thermal gradient consists of Asian surface temperature and Indian Ocean SST. Hence, the relationships of the surface temperature on each location (Asian continent and Indian Ocean) are also presented in Figure 2(c) and 2(d). Temperature changes in each location (Asia and Indian Ocean), continent-ocean thermal gradient, Asian monsoon wind, and Asian rainfall between the mid-Holocene and pre-Industrial simulations are described in Table 2.

Among models, continent-ocean thermal gradient rises with range of 0.83K to 1.45K, similar to the variability of Asian average rainfall which also increases between 0.23 to 0.68 mm/day, and Asian monsoon wind that enhances between 0.35 and 2.45 m/s (Table 2). The seasonal mean change of Asian surface temperature among models also increased by 0.57K to 1.09K, while the Indian Ocean SST relatively drop between (-0.22K) to (-0.63K). All changes are statistically significant at 95% confidence level.

Figure 2 (a) represent the relationship of multi-model variation between the continent-ocean thermal gradient and Asian monsoon wind, which indicate a positive high correlation (R score ~0.78). The range of the changes in the continent-ocean thermal gradient and Asian monsoon wind are between 0.57 to 1.09 K and 0.35 to 2.45 m/s respectively. The smallest change was simulated by GISS E2-R while the largest one was done by MRI CGCM3. GISS E2-R produces the tiniest change of the ocean-continent thermal gradient and monsoon wind at 0.83 K and 0.35 m/s respectively. While MPI-ESM-P shows the largest change of Asian monsoon wind at 2.45 m/s, instead of the ocean-continent thermal gradient.

Figure 2(b) shows multi-model variation between Asian monsoon wind and rainfall. GISS E2-R and CCSM4 indicate discernible distances from the rest on the model. Thus, two regressions were conducted. Solid line is the regression of all models, and dashed line is the regression without GISS E2-R and CCSM4. Both regression lines and correlation scores of the multi-model variation denote negative correlation (correlation score of ~(-0.43) and ~(-0.78) for the solid and dashed line). These suggest that models with much stronger ASM wind is associated with weaken Asian rainfall. The shifting range of Asian rainfall is between 0.19 to 0.68 mm/day. The correlation score without GISS E2-R and CCSM4 is higher compared to that of involving all models.

Figure 2(c) displays multi-model variation between thermal gradient and Asian rainfall. Similar to Figure 2(b), a group of models indicate anti-correlation between the two parameters. The models are: BCC-CSM1, FGOALS-G2, CSIRO MK-3-6-0, IPSL-CM5A-LR, MPI ESM-P, and MRI-CGCM3. The other two models, CSSM4 and

Table 2 Mean of the investigated physical quantities during boreal summer for the mid-Holocene minus pre-Industrial of the nine GCMs. See equations 1 to 5 for the detail calculations. All means are significant at 95% confidence level.

No	Global Model Data	ΔT_{as} (K)	ΔT_{oc} (K)	$\partial\Delta T$ (K)	ΔP_{as} (mm/day)	ΔAM_{as} (m/s)
1	BCC-CSM1	1.03	-0.42	1.45	0.27	2.16
2	CCSM4	0.70	-0.32	1.02	0.25	0.74
3	FGOALS G2	0.84	-0.63	1.47	0.19	2.14
4	CSIRO MK3-6-0	1.09	-0.22	1.32	0.68	0.91
5	IPSL CM5A	0.99	-0.34	1.33	0.43	1.62
6	MIROC ESM	0.72	-0.60	1.32	0.47	0.69
7	MPI ESM P	0.77	-0.37	1.14	0.56	1.22
8	MRI CGCM3	1.08	-0.32	1.40	0.37	2.45
9	NASA GISS E2 R	0.57	-0.26	0.83	0.41	0.35

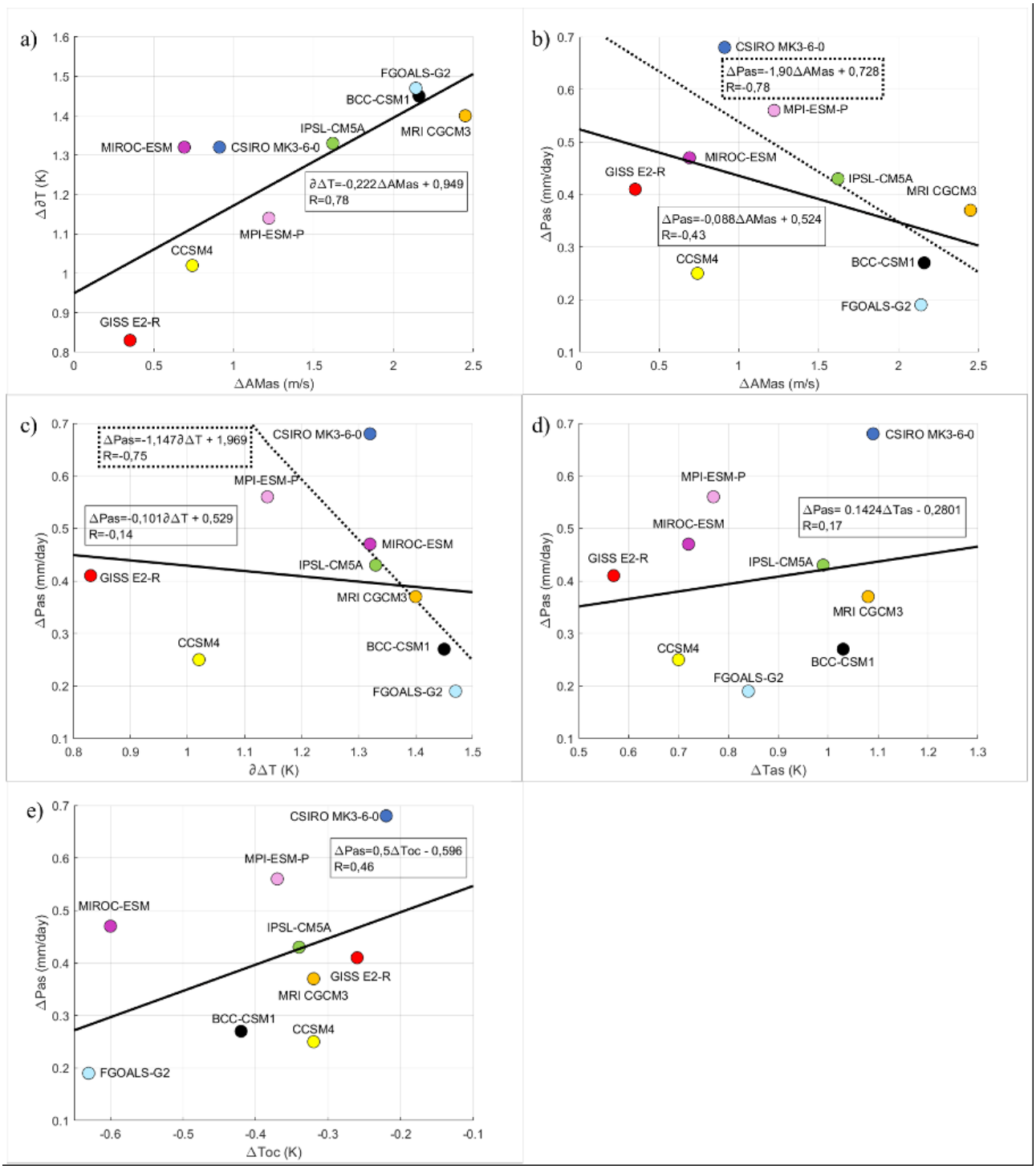

Figure 2 Link between seasonal mean of (a) ASM wind (ΔAMas) with continent-ocean thermal gradient (∂ΔT), Asian summer rainfall (ΔPas) with (b) ASM wind (ΔAMas), (c) continent-ocean thermal gradient (∂ΔT), (d) Asian surface temperature (ΔTas), and (e) Indian Ocean SST (ΔToc) for the mid-Holocene minus pre-Industrial as simulated by the nine GCMs from PMIP3. Solid lines are based on the linear regression of all GCMs, while dashed lines are regressed without CCSM4 and GISS E2-R (b,c). Text boxes contain correlation scores and linear equations of the nearest regression line.

NASA GISS-E2-R reveal noticeable distances compared to the other models. Thus, two regressions were conducted, solid line is the regression line based on all models (R=~-0.14), while the dashed line is the regression devoid CCSM4 and NASA GISS-E2-R (R=~-0.75). Negative correlation scores demonstrate that Asian rainfall variability are inversely proportional to the variability of the continent-ocean thermal gradient. It suggests that a model with small changes of the thermal gradient will have much enhanced rainfall over Asia. From a group model without CSSM4 and NASA GISS-E2-R, the smallest change of the thermal gradient (1.14K) was

simulated by MPI-ESM-P, resulting maximum rainfall of 0.56 mm/day. While the largest variability of thermal gradient (1.47K) was simulated by FGOALS-G2, resulting minimum rainfall of 0.19 mm/day.

Anti-correlation between thermal gradient and Asian monsoon wind with rainfall derived from the result in Figure 2(b) and 2(c) might be related to the variability of surface temperature either in Asia or Indian Ocean. Thus, multi-model variations between each surface temperature with Asian rainfall were also investigated. Figure 2(d) displays multi-model variation of the Asian surface temperature and Asian rainfall. The two quantities have a weak relationship since their correlation score is ~0.17. From the plot, NASA GISS-E2-R reveals the minimum Asian surface temperature up to 0.57 K, however NASA GISS-E2-R does not exhibit minimum rainfall values. Meanwhile CSIRO MK-3-6-0 shows a maximum change in both surface temperature (1.09 K) and rainfall (0.68 mm/day). Figure 2(e) represents multi-model variation of the Indian Ocean SST and Asian rainfall. Multi-model variation in Figure 2(e) demonstrates positive correlation score of ~0.45 which are higher than the one shown in Fig 2(d). FGOALS-G2 is a model that simulates the largest change in Indian Ocean SST at -0.63K, in contrast CSIRO MK-3-6-0 simulates the least change of SST at -0.22K.

DISCUSSION

All models showed significant changes in all of their involved physical quantities between the mid-Holocene and pre-Industrial simulations (Table 2). Those changes are the increase in continent-ocean thermal gradient, Asian rainfall intensity, ASM wind and Asian surface temperature; and a decrease in the Indian Ocean SST. Warmer (colder) than pre-Industrial surface temperature (SST) in Asia (Indian Ocean) during the mid-Holocene is considered as the implication of the stronger insulation during mid-Holocene compared to that during pre-Industrial on the northern Hemisphere during boreal summer (Polanski et al., 2012). Thus, changes in surface temperature in Asian continent and Indian Ocean are expected to change the thermal gradient between the two locations. These results are consistent with previous studies, which exhibit a larger-than-today inter-hemispheric thermal gradient under a stronger-than-today insolation during the mid-Holocene (Wohlfahrt et al., 2004; Zheng et al., 2013). Stronger ASM wind during the mid-Holocene is also consistent with proxy study about the strengthening of ASM during the mid-Holocene based on lake sediment records from Central Himalaya (Rawat et al., 2021).

During mid-Holocene, each model reveals stronger ASM wind and ocean-continent thermal gradient compared to these during the pre-Industrial (Table 2). Furthermore, variation of GCMs demonstrate a strengthening of the ASM wind in association with the increase of continent-ocean thermal gradient. Thus, the correlation score of the multi-model variation suggests that models with the largest increase in temperature gradient resulting the largest increase in their ASM wind. This result is consistent with the monsoon theory, which noted that the higher temperature gradient leads to the higher wind speed (Desai et al., 2009).

Multi-model variation between changes in ASM wind and continent-ocean thermal gradient with the changes in Asian rainfall indicate an inverse correlation, particularly when GISS E2-R and CCSM4 are excluded (Figure 2b and 2c). This result implies that models with the smallest increase in ASM wind and temperature gradient lead to greater rainfall over Asia. This inverse correlation is inconsistent with the general understanding of the ASM variability (Cheng et al., 2016b; Ren et al., 2021; Schneider et al., 2014). ASM wind and rainfall are known to vary in-coherent with continent-ocean thermal gradient as their main driver. Thus, the discrepancy between multi-model variation with the general understanding of ASM indicates serious issues may actually be occurred by the multi-model. Previous research has also found a misdistribution of the GCMs in comparison with proxies for the relationship between El Nino Southern Oscillation (ENSO) with seasonal cycle (Emile-Geay et al., 2015). In conclusion, multi-model variation actually encounters various issues, and one of them is observed by our study.

The inverse correlation may actually be caused by the changes of the Indian Ocean SST (which indicates cooling trend) since it is a negative factor in Equation 3. This is confirmed by the multi-model analyses which demonstrated that a stronger-than-today Asian rainfall during the mid-Holocene is more correlated with less cold than-today Indian Ocean SST rather than with much warmer-than-today Asian surface temperature. Such relationship is further confirmed by the scores of their partial correlations, which emphasized the independent effect of each surface temperatures to the Asian rainfall by eliminating the other influences. Changes of the Indian Ocean SST has a partial correlation up to ~0.43 with the changes of the rainfall in Asian continent. While the partial correlation between changes of surface temperature in the Asian continent with the changes in Asian rainfall is only ~0.1. Thus, a model that simulates a less cold-than-today Indian Ocean SST produces a much wetter-than-today Asian climate during the mid-Holocene.

Multi-model analyses revealed the significant role of Indian Ocean SST in changing rainfall over Asian continent in orbital time scale (Figure 2e). Correlation of the multi-model variation between the two parameters shows that a less cold SST in the Indian Ocean produces a much higher rainfall over Asia. In order to speculate on the underline mechanism, we may assume that model with less cold SST on the Indian Ocean might also have more areas of unchanged or even warmer SST. The unchanged and/or warmer SST might be related to the moisture supply of the ASM which is associated with the evaporation in the Indian Ocean. In boreal summer, evaporation in Indian Ocean is the source of horizontal

moisture flux and ASM eventually. Thus, a less cold Indian Ocean SST will have a less suppressed evaporation on the ocean surface. Surface evaporation in Indian Ocean gives a contribution to the supply of the atmospheric water vapor, which is the source of rainfall in Asia.

Positive correlation between Indian Ocean SST and rainfall over Indian sub-continent are already known to occur within biennial (2-3 years) time-scales (Li et al., 2001). Long-term positive anomaly of the SST in some part of the Indian Ocean increases surface moisture due to the increase in evaporation. As a consequence, a heavy monsoon rainfall over Indian sub-continent occurred resulted from stronger moisture fluxes into the ASM region. Similar mechanism, but in an orbital time-scale, could be suggested to explain the role of Indian Ocean SST in increasing Asian rainfall, simulated in our multi-model analyses. Model with a less cold Indian Ocean SST suppresses much less evaporation compared to the other models do. This perhaps due to more pockets of unchanged/warmer SST. Along these lines, our speculated mechanisms are in accordance to the results of the multi-model. CESS FGOAL-S2 is a model that apply the coldest Indian Ocean SST to simulate a smallest increase of Asian rainfall. While CSIRO MK-3-6-0 is a model that shows the least cold SST simulates a much higher Asian rainfall. Thus, moisture content dynamic over the Indian Ocean is important for the increase of ASM during the mid-Holocene climate change relative to the pre-Industrial.

Correlation score of the multi-model variation between higher-than-today Asian rainfall to the colder-than-today Indian Ocean SST (~-0.45) is higher than the one with the warmer-than-today Asian continent (~0,17) (Fig. 2c & 2d). However, warmer-than-today Asian continent remains arguably important since the correlation between the higher-than-today Asian rainfall to the changes of continent-ocean thermal gradient (~-0.75) is much higher than the one with the Indian Ocean SST (Fig. 2b & 2c). Such a high correlation score emphasizes on the important role of a warmer-than-today Asian continent in the multi-model variation, based on the calculation of the continent-ocean thermal gradient (Equation 3). Further investigation of multi-model variation of the ever-changing ASM throughout various climate scenarios remains crucial to get a better understand multi-model behavior, which is needed to evaluate the precision of the future climate projection (Chhin & Yoden, 2018).

CONCLUSIONS

This research can be concluded that the changes in continent-ocean thermal gradient has a positive correlation with ASM wind. However, a negative correlation occurs between changes in continent-ocean thermal gradient with Asian rainfall. Models that simulate large changes in the continent-ocean thermal gradient produce the smallest increase in the Asian rainfall and vice versa. Such inverse relation is likely due to the cooling of Indian Ocean SST since its correlation scores with Asian rainfall is much higher than the one with the warming of the Asian continent. Thus, multi-model variation of the increased rainfall over the Asian continent between mid-Holocene and today is mainly related to the multi-model variation of the cooling in the Indian Ocean SST.

ACKNOWLEDGEMENTS

This research is part of projects titled “Marine Science & Technology Cooperation between Korea and Indonesia (20180319)” and “Ocean and Coastal Basic Survey and Capacity Enhancement in Cirebon, Indonesia (G52440)” which are funded by the Ministry of Oceans and Fisheries, Korea.

AUTHOR CONTRIBUTION

Adinda Maharani acquired and analyzed all GCMs simulations output from the PMIP3 online database, and also wrote the manuscript. Yudha Setiawan Djamil proposed the main idea, designed the analytical approach, and actively involved in the discussion, also correction and comments on the manuscript. Thus, Adinda Maharani and Yudha Setiawan Djamil are considered as the main contributors of this manuscript. Author member: Rima Rachmayani contributes to the discussion of the main idea, gave permission to use computer equipment for data processing, also correction and comments on the manuscript.

REFERENCES

Bartlein, P. J., Harrison, S. P., Brewer, S., Connor, S., Davis, B. A. S., Gajewski, K., Guiot, J., Harrison-Prentice, T. I., Henderson, A., Peyron, O., Prentice, I. C., Scholze, M., Seppa, H., Shuman, B., Sugita, S., Thompson, R. S., Viau, A. E., Williams, J., & Wu, H. 2011. Pollenbased continental climate reconstructions at 6 and 21 ka a global synthesis. *Climate Dynamics*, 37(3–4): 775–802. https://doi.org/10.1007/s00382-010-0904-1.

Berger, A. 1978. Long-term variations of daily insolation and Quaternary climatic changes. *Journal of the Atmospheric Sciences*, 35(12): 2362–2367.

Braconnot, P., Denvil, S., Foujols, M. A., Caubel, A., Marti, O., Dufresne, J.-L., Bopp, L., Cadule, P., Ethé, C., Idelkadi, A., Mancip, M., Masson, S., Mignot, J., Ionela, M., Balkanski, Y., Bekki, S., Bony, S., Brockman, P., Codron, F.,Vuichard, N. 2016. *IPSL-CM5A-LR model output prepared for CMIP5 midHolocene experiment, served by ESGF*. World Data Center for Climate (WDCC) at DKRZ. https://doi.org/https://doi.org/10.1594/WDCC/CMIP5.IPILmh. https://www.wdc-climate.de/ui/ accessed at 2021-08-20.

Braconnot, P., Marti, O., Joussaume, S., & Leclaineche, Y. 2000. Ocean Feedback in Response to 6 kyr BP Insolation. *Journal of Climate*, 13: 1537–1553.

Chen, F., Yu, Z., Yang, M., Ito, E., Wang, S., Madsen, D. B., Huang, X., Zhao, Y., Sato, T., Birks, H. J. B., Boomer, I., Chen, J., An, C., & Wunnemann, B. 2008. Holocene moisture evolution in arid central Asia and its out-of-phase relationship with Asian monsoon history. *Quaternary Science Reviews*, 27: 351–364. https://doi.org/10.1016/j.quascirev.2007.10.017.

Cheng, H, Edwards, R., Sinha, A., Spötl, C., Yi, L., Chen, S., Kelly, M., Kathayat, G., Wang, X., Li, X., & Kong, X. 2016a. The Asian monsoon over the past 640,000 years and ice age terminations. *Nature*, 534(7): 609–640.

Cheng, H., Spötl, C., Breitenbach, S. F. M., Sinha, A., Wassenburg, J. A., Jochum, K.P., Scholz, D., Li, X., Yi, L., Peng, Y., Lv, Y., Zhang, P., Votintseva, A., & Loginov, V., 2016b. Climate variations of Central Asia on orbital to millennial timescales. *Scientific Reports,* 5: 36975. DOI: 10.1038/srep36975. PMID: 27833133; PMCID: PMC5105073.

Cheng, J., Wu, H., Chen, H., Lu, H., Liu, Z., Gu, P., Wang, J., Zhao, C., & Li, Q. 2021. Vegetation feedback causes delayed ecosystem response to East Asian Summer Monsoon Rainfall during the Holocene. *Nature Communications*. https://doi.org/10.1038/s41467-021-22087-2.

Chhin, R., & Yoden, S. 2018. Ranking CMIP5 GCMs for model ensemble selection on regional scale: case study of the Indochina Region. *Journal of Geophysical Research: Atmospheres*, 123(17): 8949–8974.

Dallmeyer, A. and Claussen, M., 2011. The influence of land cover change in the Asian monsoon region on present-day and mid-Holocene climate. *Biogeosciences,* 8: 1499-1519. 10.5194/bg-8-1499-2011.

Desai, A. R., Austin, J. A., Bennington, V., & Mckinley, G. A. 2009. Stronger winds over a large lake in response to weakening air-to-lake temperature gradient. *Nature Geoscience*, 2(12): 855–858.

Ding, Y., & Chan, J. C. L. 2005. The East Asian summer monsoon : an overview. *Meteorog. Atmos. Phys*, 142: 117–142. https://doi.org/doi.org/10.1007/s00703-005-0125-z.

Emile-Geay, J., Cobb, K. M., Carré, M., Braconnot, P., Leloup, J., Zhou, Y., Harrison, S. P., Corrège, T., Mcgregor, H. V, Collins, M., Driscoll, R., Elliot, M., Schneider, B., & Tudhope, A. 2015. Links between tropical Pacific seasonal, interannual and orbital variability during the Holocene. *Nature Geoscience*, 1–7. https://doi.org/10.1038/ngeo2608.

Hewitt, C. D., & Mitchell, J. F. B. 1996. GCM Simulations of Climate of 6 kyr BP: Mean Changes and Interdecadal Variability. *Journal of Climate*, 9: 3505–3529.

<https://www.wdc-climate.de/ui/> [Accessed at 20 August 2021].

<https://wiki.lsce.ipsl.fr/pmip3/doku.php/310822 - BoMG_Vol37_No1_Jatiningrum_etalpmip3:database:status> [Accessed at 4 May 2022].

JAMSTEC, AORI, & NIES. 2015. *MIROC-ESM model output prepared for CMIP5 midHolocene, served by ESGF*. World Data Center for Climate (WDCC) at DKRZ. https://doi.org/https://doi.org/10.1594/WDCC/CMIP5.MIMEmh. https://www.wdc-climate.de/ui/ accessed at 2021-08-20.

Jeffrey, S., Rotstayn, L., Collier, M., Dravitzki, S., Hamalainen, C., Moeseneder, C., Wong, K., & Syktus, J. 2016. *CSIRO-Mk3-6-0 model output prepared for CMIP5 midHolocene (Version 2015), served by ESGF*. World Data Center for Climate (WDCC) at DKRZ. https://doi.org/https://doi.org/10.1594/WDCC/CMIP5.CQMKmhv2015. https://www.wdc-climate.de/ui/ accessed at 2021-08-20.

Jiang, D., Tian, Z., & Lang, X. 2013. Mid-Holocene net precipitation changes over China : model e data comparison. *Quaternary Science Reviews*, 82: 104–120. https://doi.org/10.1016/j.quascirev.2013.10.017.

Joussaume, S., Taylor, K. E., Braconnot, P., Mitchell, J. F. B., Kutzbach, J. E., Harrison, S. P., Prentice, I. C., Broccoli, A. J., Abe-Ouchi, A., Bartlein, P. J., Bonfils, C., Dong, B., Guiot, J., Henerich, K., Hewitt, C. D., Jolly, D., Kim, J. W., Kislov, A., Kitoh, A., Wyputt, U. 1999. Monsoon changes for 6000 years ago: Results of 18 simulations from the Paleoclimate Modeling Intercomparison Project (PMIP). *Geophysical Research Letters*, 26(7): 859–862.

Jungclaus, J., Giorgetta, M., Reick, C., Legutke, S., Brovkin, V., Crueger, T., Esch, M., Fieg, K., Fischer, N., Glushak, K., Gayler, V., Haak, H., Hollweg, H.-D., Kinne, S., Kornblueh, L., Matei, D., Mauritsen, T., Mikolajewicz, U., Müller, W., Stevens, B. 2012. *CMIP5 simulations of the Max Planck Institute for Meteorology (MPI-M) based on the MPI-ESM-P model: The midHolocene experiment, served by ESGF*. World Data Center for Climate (WDCC) at DKRZ. https://www.wdc-climate.de/ui/ accessed at 2021-08-20.

LASG, Institute of Atmospheric Physics, C. A. of S. (IAP-L. 2015. *FGOALS-g2 model output prepared for CMIP5 midHolocene, served by ESGF*. World Data Center for Climate (WDCC) at DKRZ. https://doi.org/https://doi.org/10.1594/WDCC/CMIP5.LSF2mh. https://www.wdc-climate.de/ui/ accessed at 2021-08-20.

Li, T., Chang, C., & Wang, B. 2001. On the relationship between Indian Ocean sea surface temperature and Asian Summer Monsoon. *Geophysical Research Letters*, 28(14): 2843–2846.

Mahowald, N. M., Yoshioka, M., Collins, W. D., Conley, A. J., Illmore, D. W., & Coleman, D. B. 2006. Climate response and radiative forcing from mineral aerosols during the last glacial maximum, pre-industrial, current and doubled-carbon dioxide climates. *Geophysical Research Letters*, 33(20): 1-4.

NASA Goddard Institute for Space Studies (NASA/GISS). 2014. *NASA-GISS: GISS-E2-R model output prepared for CMIP5 mid-Holocene, served by ESGF.* World Data Center for Climate (WDCC) at DKRZ. https://doi.org/https://doi.org/10.1594/WDCC/CMIP5.GIGRmh. https://www.wdc-climate.de/ui/ accessed at 2021-08-20.

Ohgaito, R. & Abe-Ouchi, A., 2007. The role of ocean thermodynamics and dynamics in Asian summer monsoon changes during the mid-Holocene. *Climate Dynamic,* 29: 39-50. 10.1007/s00382-006-0217-6.

Otto-Bliesner, B. 2014. *CCSM4 coupled simulation for CMIP5 with mid-Holocene conditions, served by ESGF*. World Data Center for Climate (WDCC) at DKRZ. https://doi.org/https://doi.org/10.1594/WDCC/CMIP5.NRS4mh. https://www.wdc-climate.de/ui/ accessed at 2021-08-20.

Polanski, S., Rinke, A., Dethloff, K., Lorenz, S. J., Wang, Y., & Herzschuh, U. 2012. Simulation and comparison between mid-Holocene and Pre-Industrial Indian summer monsoon circulation using a regional climate model. *The Open Atmospheric Science Journal*, 6: 42–48.

Rao, Z., Jia, G., Li, Y., Chen, J., Xu, Q., & F., C. 2016. Asynchronous evolution of the isotopic composition and amount of precipitation in north China during the Holocene revealed by a record of compound-specific carbon and hydrogen isotopes of long-chain n-alkanes from an alpine lake. *Earth and Planetary Science Letters*, 466: 68–76. https://doi.org/10.1016/j.epsl.2016.04.027.

Rawat, V., Rawat, S., Srivastava, P., Negi, P. S., Prakasam, M., & Kotlia, B.S. 2021. *Middle Holocene Indian summer monsoon variability and its impact on cultural changes in the Indian subcontinent*. *Quaternary Science Reviews, 255(2021)*.https://doi.org/10.1016/j.quascirev.2021.106825.

Ren, X., Sha, Y., Shi, Z., & Liu, X. 2021. Response of summer extreme precipitation over East Asia during the mid-Holocene versus future global warming. *Global and Planetary Change*, 197: 103–398.

Schneider, T, Bischoff, T., & Haug, G. H. 2014. Migrations and dynamics of the intertropical convergence zone. *Nature*, 513(7516): 45–53.

Tao, W., Huijun, W., & Dabang, J. 2010. Mid-Holocene East Asian summer climate as simulated by the PMIP2 models. *Palaeogeography, Palaeoclimatology, Palaeoecology*, 288(1–4): 93–102. https://doi.org/10.1016/j.palaeo.2010.01.034.

Wang, B., & Fan, Z. 1999. Choice of South Asian Summer Monsoon Indices. *Bulletin of the American Meteorological Society,* 80(4): 629–638.

Wang, B., R, Wu., K-M, Lau. 2001. Inter Annual variability of Asian summer monsoon: contrast between the Indian and western North Pacific-East Asian monsoon. *Journal of Climate,*14: 4073-4090.

Wen, R., Xiao, J., Chang, Z., Zhai, D., Xu, Q., Li, Y., Itoh, S., & Lomtatidze, Z. 2010. Holocene climate changes in the mid-high-latitude-monsoon margin re fl ected by the pollen record from Hulun Lake , northeastern Inner Mongolia. *Quaternary Research*, 73(2): 293–303. https://doi.org/10.1016/j.yqres.2009.10.006.

Wohlfahrt, J., Harrison, S. P., & Braconnot, P. 2004. Synergistic feedbacks between ocean and vegetation on mid- and high-latitude climates during the mid-Holocene. *Climate Dynamics*, 22: 223–238.

Wu, T., & Xin, X. 2015. *bcc-csm1-1 model output prepared for CMIP5 midHolocene experiment, served by ESGF*. World Data Center for Climate (WDCC) at DKRZ. https://doi.org/https://doi.org/10.1594/WDCC/CMIP5.BCB1mh. https://www.wdc-climate.de/ui/ accessed at 2021-08-20.

Xiao, J., Chang, Z., Wen, R., Zhai, D., Itoh, S., & Lomtatidze, Z. 2009. Holocene weak monsoon intervals indicated by low lake levels at Hulun Lake in the monsoonal margin region of northeastern Inner Mongolia , China. *Holocene*, 19: 899–908.

Yafeng, S., Zhaozheng, K., Sumin, W., Lingyu, T., Fubao, W., Tandong, Y., Xitao, Z., Peiyuan, Z., & Shaohua, S. 1993. Mid-Holocene climates and environments in China. *Global and Planetary Change*, 7(1–3): 219–233.

Yukimoto, S., Adachi, Y., Hosaka, M., Sakami, T., Yoshimura, H., Hirabara, M., Tanaka, T., Shindo, E., Tsujino, H., Deushi, M., Mizuta, R., Yabu, S., Obata, A., Nakano, H., Koshiro, T., Ose, T., & Kitoh, A. 2015. *MRI-CGCM3 model output prepared for CMIP5 midHolocene, served by ESGF.* World Data Center for Climate (WDCC) at DKRZ. https://doi.org/https://doi.org/10.1594/WDCC/CMIP5.MRMCmh. https://www.wdc-climate.de/ui/ accessed at 2021-08-20.

Zhao, Y., Braconnot, P., Marti, O., Harrison, S. P., Hewitt, C., Kitoh, A., & Weber, S. L. 2005. A multi-model analysis of the role of the ocean on the African and Indian monsoon during the mid-Holocene. *Climate Dynamics*, 25(7–8): 777–800. https://doi.org/10.1007/s00382-005-0075-7.

Zheng, B., Wu, J., He, Y., & Yu. 2013. The East Asian Summer Monsoon at mid-Holocene: results from PMIP3 simulations. *Climate Past*, 9: 453–466. https://doi.org/10.5194/cp-9-453-2013.

ASH LAYERS FROM SOUTH ANDAMAN SEA: PROBABLY SOURCED FROM TOBA CALDERA

Sachin Kumar Tripathi[1*], Manoj R.V.[2], Mritunjay Chaturvedi[1], and Resmi S.[1]

[1] Geological Survey of India, Northern Region, Lucknow.

[2] Marine and Coastal Survey Division, Geological Survey of India, Mangalore

*Corresponding author: sachin.tripathi@gsi.gov.in

(Received 26 July 2022; in revised from 31 July 2022; accepted 5 September 2022)

DOI : 10.32693/bomg.37.1.2022.765

ABSTRACT: Deep Sea sediment core PC-1 from the South Andaman Sea (7˚19.85' N; 94˚ 39.26' E; in East Andaman Basin) below the water depth of 3144 m contain discrete ash layers at various depths. According to morphological study, these ash layers contain glass shards of different varieties *i.e.* Type-I, Type-II, Type-III, Type-IV and Type-V and it is comparable to glass shards of Toba volcanic reported from other parts of the world. This observation is also supported on the basis of relative biostratigraphic datum observed in the core PC-1. The Layer-A (56 cm thick) at 210 cm bsf is just above the biostratigraphic datum of *ca.* 0.12 Ma, correspond to Youngest Toba Tuff (YTT), followed by Layer-C belongs to Middle Toba Tuff (MTT) and Layer-D inferred as Oldest Toba Tuff (OTT). This interpretation is further supported by the geochemical data obtained from the EDX analysis, which suggest high silica and alkali contents of rhyolitic composition. Hence, geochemical composition, morphology and biostratigraphic data of these discrete tephra layers show identical characteristics to the products of Toba eruptions, including YTT, MTT and OTT.

Keywords: Glass shards, Andaman Sea, Toba ash, YTT, MTT and OTT

INTRODUCTION

The Toba caldera on the Sumatra Island is the largest known explosive volcanism on earth during the Quaternary period, at least in the last 100,000 years (Smith and Bailey, 1968; Rose and Chesner, 1987; Zielinski et al., 1996; Oppenheimer, 2002). Over the past 1.2 Ma, there have been four ash flow tuff eruptions noticed from the caldera complex (Chesner and Rose, 1991; Chesner et al., 1991). The youngest Toba tuff (YTT) was erupted at 74 ka (Ninkovich *et al.,* 1978; Chesner et al., 1991) and has a minimum volume of 2800 km^3 (Rose and Chesner, 1987). The other Toba eruptive products are the Middle Toba Tuff (MTT) erupted at *ca.* 0.50 Ma ($^{40}Ar/^{39}Ar$), Chesner et al., 1991) and the Oldest Toba Tuff (OTT) eruption was at *ca*. 0.84 Ma ($^{40}Ar/^{39}Ar$, Diehl *et al.,* 1987). The total erupted rock volume of YTT was approximately 3 orders of magnitude greater than Mount St. Helens' 1980 eruption (Robock et al., 2009).

The Toba ash layer and dispersed glass shards from the Toba caldera eruption in northern Sumatra have been reported from Malaysia, the northern and central Indian Ocean, Arabian Sea and South China Sea (Figure 1; Ninkovich et al., 1978; Dehn et al., 1991; Schulz et al., 1998; Pattan et al., 1999; Bühring and Sarthein, 2000, Pattan et al., 2002; Liu et al., 2006; Pattan et al., 2010). Apart from Sumatra Island and the northern Indian Ocean, Toba tephra has been found in Quaternary sediments throughout the eastern and central part of Indian peninsula, particularly in lower Narmada basin and central Narmada valley (William and Royce, 1982; William and Clarke, 1984; Rose and Chesner, 1987; Basu et al., 1989; Biswas et al., 1989; Acharyya and Basu, 1993; and Rachna, 2008). Toba eruptive products have also been reported from other parts of India, including along the Kukadi River at Bori, Maharashtra (Korisettar et al., 1989), Mahanadi and Brahmani River basins (Devdas and Meshram, 1991) Goguparhu, Kareni and Guruwara (Acharyya and Basu, 1993), Vansadhara and Nagavali River basins (Devdas and Meshram, 1991), and Sagileru River basin, Andhra Pradesh (Acharyya and Basu, 1993).

Moreover, other researchers also reported detailed analysis from site-758 core and identified the presence of multiple ash layers at various depths represented as layer A, C, D and E (Dehn et al., 1991, Pattan et al., 2010; Pearce et al., 2014). These different eruptive episodes of Toba correspond to layer A as YTT (1.5 m to 1.84 m), layer C corresponds to MTT (7.12 m to 7.35 m), layer D to E corresponds to OTT (10.8 m to 10.93 m; 11.62 m to 11.67 m) respectively. Similarly, we documented the presence of several ash layers in the South Andaman Sea (7˚19.85' N; 94˚ 39.26' E; in East Andaman Basin; at a water depth of 3144 m) during onboard R. V. Samudra Ratnakar expedition cruise of Geological Survey of India. In 28.95 m length of Piston Core (PC-1), distinct ash layers were discovered at depths of 2.10 m to 2.66 m**,** 13.50 m to 14.50 m and 18 m to 24 m below sea floor (bsf). Geochemical,

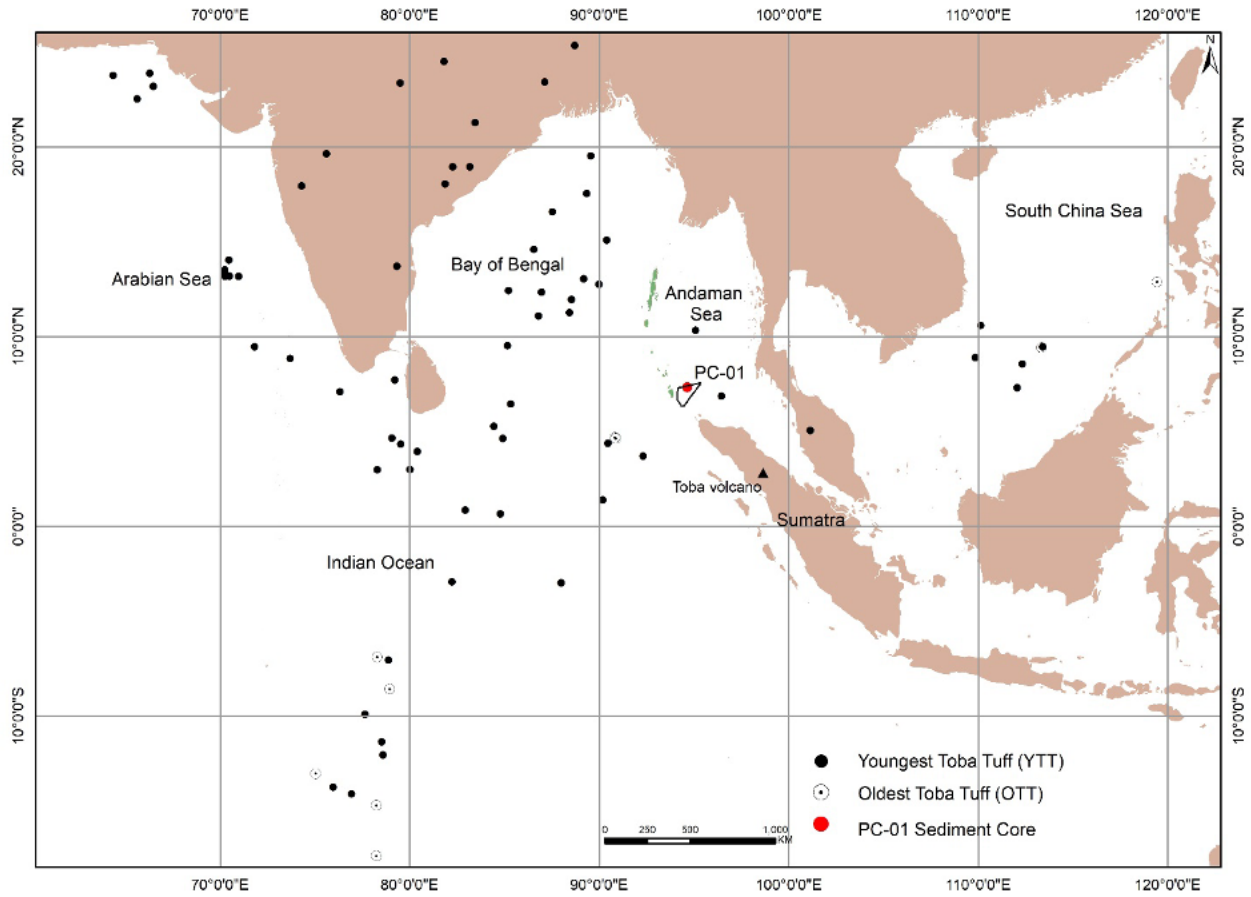

Figure 1. Toba Tuff distribution map around northern part of Indian Ocean, Bay of Bengal, Indian Subcontinent, South China Sea and Andaman Sea along with core location (modified after Liu et al., 2006).

morphological and stratigraphical, analyses were performed in this study to better understand the relationship between these ash layers and Toba Volcanics.

Geological setting of study area

Study area is located at East Andaman basin in a complex back-arc extensional setting, along highly oblique convergent margin of overriding Eurasian Plate and subducting Indo-Australian Plate (Figure 2; McCaffrey, 1991; Curray, 2005; and Cochran, 2010). Initially, a proto-Andaman Sea is thought to have existed as an extensional basin in place of the present Mergui-North Sumatra that shifted westward probably as a consequence of the Early Miocene intercontinental under thrusting to a location between the Alcock and Sewell seamount complexes (Curray, 2005). The north-south ridge system opened the eastern Andaman Sea by drifting from the main land of Malay Peninsula during early Tertiary (Curray, 2005). Later, the extension of the Andaman Sea kept on changing which was initially almost E-W and WNW-ESE during Late Palaeogene and highly oblique extension (NNW-SSE) during Neogene (Morley, 2017). The plate edge assumed to be the Sagaing Fault (SF) that was directly associated with the former West Andaman Fault (WAF) in the Early Oligocene (Curray, 2005). The present plate edge is the Sagaing Fault in Myanmar, which passes through the system of short spreading axes and transform faults to the longer spreading axis, then southward on the WAF, Seulimeum fault system (SEU) and Sumatran fault system (SFS) (Figure 2).

The WAF and SFS separate the geomorphic configuration of back-arc region of the East Andaman Basin and North Sumatra basin from the fore-arc basin. However, the western boundary of the sample area is adjacent to the SEU, in the southern part having mixed response of strike-slip as well as normal-fault (Curray, 2005; Figure 3). The WAF on the other hand, runs roughly N-S direction as a prominent tectonic and physiographic feature extends for more than 1000 km, in the western part of the Andaman Sea and eventually merging with SFS around Great Nicobar and finally abutting to the Sunda Subduction Zone (Curray, 2005; Figure 2). An active SEU traced along the submarine volcanic arc and extends up to the West Sewell Ridge (WSR), and converges with the SFS at 5˚N. A series of submarine volcanoes with well-developed craters aligned parallel to the Subduction zone exist along the SEU fault system (Tripathi et al., 2018; Figure 3).

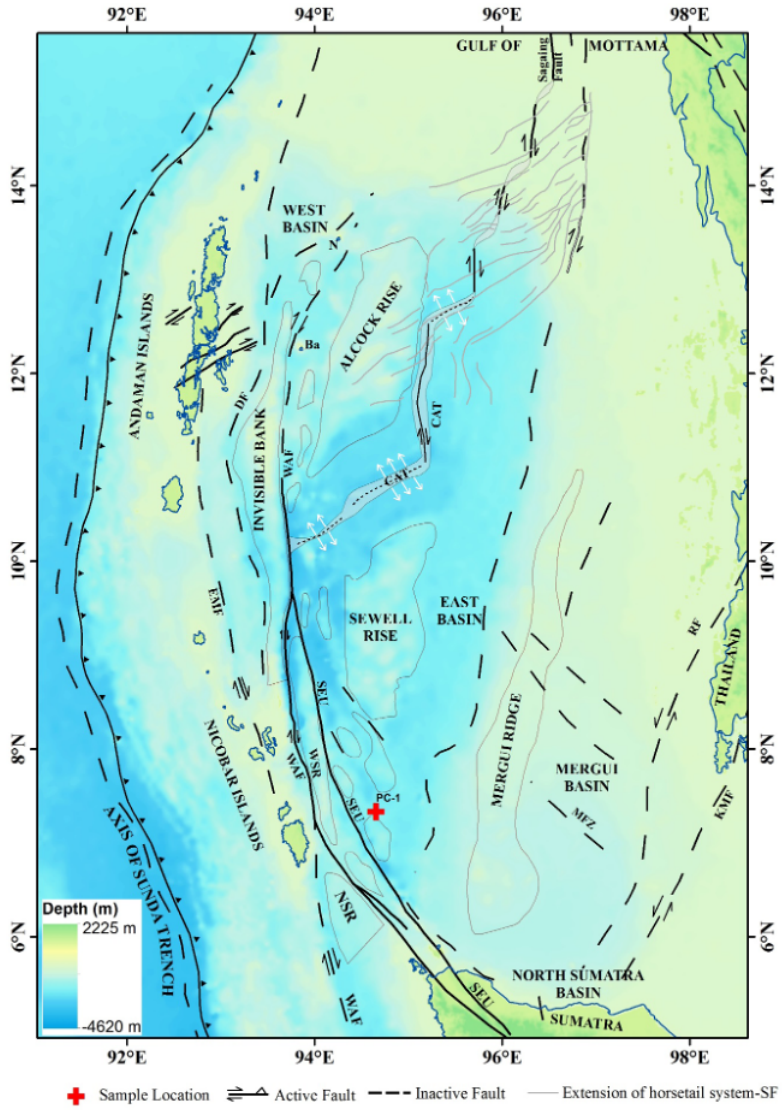

Figure 2. Map depicts disposition of major lineaments in the Andaman Sea. Abbreviations for this figure: Ba= Barren Island, N = Narcondam Island, DF = Diligent Fault, EMF= Eastern Margin Fault, NSR = North Sumatra Ridge, SEU = Seulimeum fault, WAF= West Andaman Fault, CAT= Central Andaman Trough, White arrow shows extension regime within the CAT spreading axis (after Curray, 2005 and Diehl et al., 2013).

METHODOLOGY

The study is primarily focused on the ash layers discovered at a depth of 2.10 m to 2.66 m bsf, with sediments showing variation from the silty clay to clayey silt (Figure 4). The colour of the ash layer is pale grey. It is also noticed that the glass shards abundant in range between 2.10 m to 2.36 m and down to 2.36 m, pumice is gradually increasing and glass shards are significantly reducing (Figure 4). Apart from 2.10 m ash layer, many other discrete glass shards layers were observed at various depths with the main zones at 13.50 m to 14.50 m and 18 m to 24 m. Entire sediment core was sampled at 2 cm interval for coarse fraction study. To eliminate organic components, subsampled ash layers were treated with 6% hydrogen peroxide. To remove the carbonate material, mild hydrochloric acid was added later. The ash layers were then wet sieved through > 63 µm mesh and oven dried for further study. The glass shards were handpicked under a binocular microscope and separated samples were then subjected to a detailed morphological study under Scanning Electron Microscopy (SEM). To determine the origin of the ash layers, the major element composition was determined by using the technique developed by Westgate and Gorton (1981), utilising an Energy Dispersive X-ray Spectroscope (EDX). SEM-BSE-EDX analysis on representative glass shards separated from PC-1 sediment core was performed using ZEISS EVO 40 of Carl Zeiss AG that installed at NCEGR, GSI, Kolkata. The separated and handpicked glass/pumice shards were mounted on the carbon tapped stubs that had been carbon coated and scanned under electron microscope to study the morphological aspects and achieve high resolution images. All the elements were analysed using normalized standards of MAC (25mm × 5mm Brass). To determine the elemental composition of shards components, X-ray

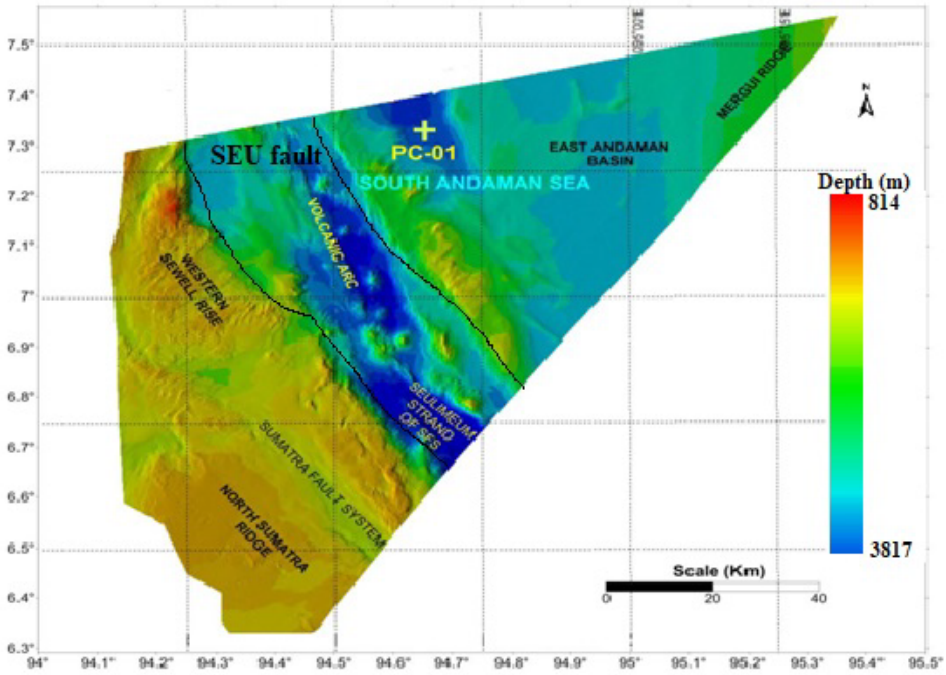

Figure 3. Swath bathymetric map depicting major morpho-tectonic features of South Andaman sea.

spectroscopy (EDX) analysis was done. As operational parameters, an accelerating voltage of 10 - 20 kV and an electron beam current of 12 nA focused to 1 µm spot size were used for the analyses. Along with sedimentological studies, micropalaeontological studies were also carried out to determine the relative age of the sediments and their depositional environment.

RESULTS AND DISCUSSION

The microscopic study of the coarse fraction indicates the presence of radiolarians, biotite, rock fragments and glass-pumice shards of varying abundance. The glass shards are fresh, unaltered, colourless and blocky in nature, whereas pumice shards are white to colourless and extremely vesiculated in nature. The average size of the glass shards ranges between 10 and 300 µm. Glass shards with blocky fractures are completely absent at the top of representative sample and scarce at the bottom indicating a prominent source. A detailed study has been carried out below to establish the possible link with Toba volcanic to pinpoint the possible source.

Morphology

In SEM study, various types of glass shards were noticed as mentioned in Figure 5. Shards are colorless, fresh, unaltered, and isotropic in nature with typical bubble wall junction morphology. Shards are mainly > 63 microns size and can be classified into five types (Figure 5). Type-I, glass shards are flat/oval in shape and are formed by disintegration of large flattened bubbles (Pattan

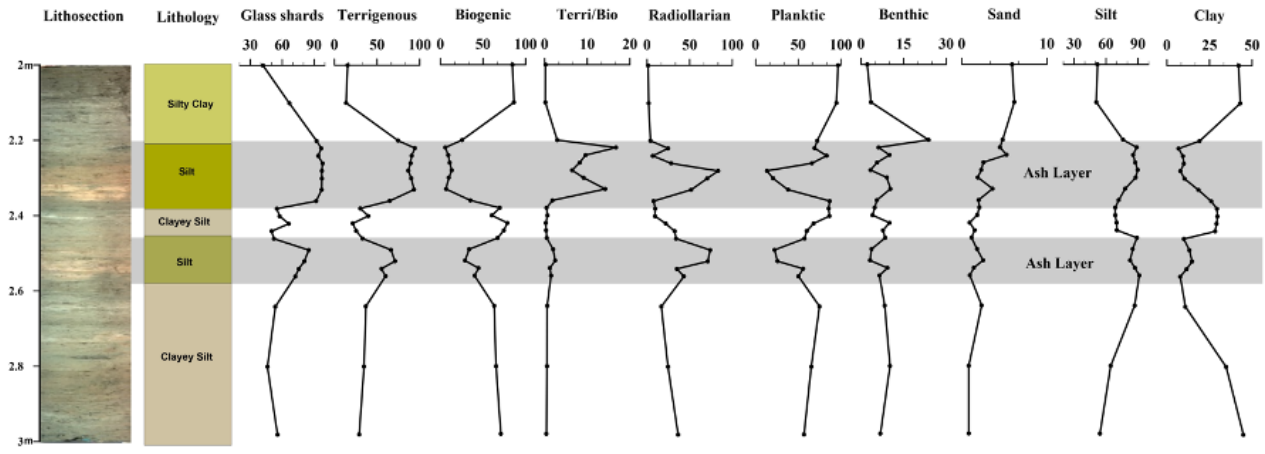

Figure 4. Coarse fraction data representing biogenic, terrigenous and glass shards data between 2 to 3 m of the studied core PC-1, depicts two prominent peaks of ash layer corresponding to YTT.

et al., 2002; Rose and Chenser, 1987). Type-II is distinguished by two to three bubble wall junctions, whereas Type-III are characterized by more than three or multiple bubble wall junctions. Type-IV forms the pumice shards with elongated vesicles, which are comparatively bigger in size and Type-V shards have fluid/gas inclusions. The glass shards consist of wall of tiny shattered bubbles or junction of bubbles formed by the vesiculation of silicic magma. Furthermore, Izett et al. (1981) proposed that pumice shards, bubble walls and shard wall junctions formed from high viscosity rhyolitic magma. A similar observation is seen in the analysed glass shards. The bubble wall nature and the characteristics of the glass shards indicate a subaerial volcanic source, which is almost similar to Toba ashes reported from Central Indian Ocean Basin (Dehn et al., 1991), Indian Subcontinent, Bay of Bengal (Rose and Chesner, 1987), South China Sea (Bühring and Sarnthein, 2000 and Liu et al., 2006).

Geochemical study

Major elemental compositions identified by X-ray spectroscopy (EDX) of the selected samples of glass shards is given in Table 1. The glass shards are high in silica and alkali contents; the SiO_2 content ranges from 77 to 82 wt %, and the alkali content ranges from 5 to 6 wt % that display a very little variation both within and between samples (Table 2). The EDX results of glass shards samples were plotted to TAS classification diagram of Le Maitre et al. (1989), and samples suggest rhyolitic composition (Figure 6). Major elemental composition gives high silica along with other associated elements Al_2O_3 (~10.5-12.5wt%) and FeO (~0.50-2.5 wt%). Silica versus K_2O plots demonstrate that the shards are falling in high K-field (Figure 7). Overall, geochemical contents of PC-1 glass shards showing its affinity with ash layers reported from CIOB (Pattan et al., 1999), Bay of Bengal (Gasparotto et al., 2000; Dehn et al., 1991), Indian Subcontinent (Shane et al.,1995), Northern Sumatra (Chesner, 1988) and South China Sea (Bühring et al., 2000; Song et al., 2000; Liang et al., 2001). Further, bivariant plots of SiO_2 vs Al_2O_3 and SiO_2 vs Na_2O shows comparable YTT characteristics. The comparative analysis of the glass shards suggest that the shards were probably derived from the Toba eruptions.

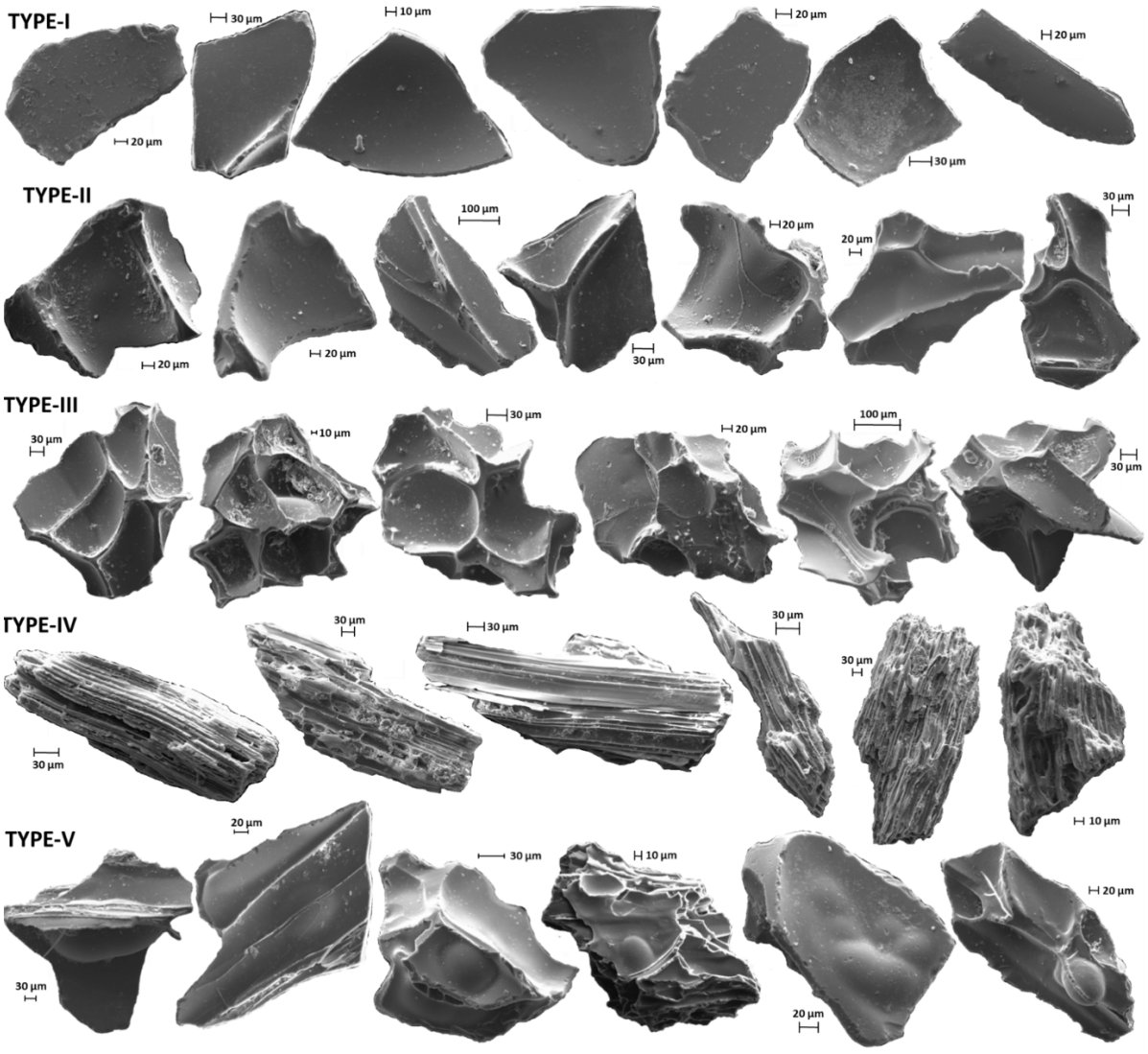

Figure 5. Types of glass shards based on the bubble wall junction morphology from Core PC-1 (Type-I: flat / oval shaped, Type-II: two- three bubble wall junctions, Type-III: more than three or multiple bubble wall junctions, Type-IV: pumice shards with elongated vesicles and Type-V: shards with fluid/gas inclusions).

Table 1: Major elemental composition (wt%) of the glass shards examined using energy dispersion spectrum (EDX) for 7 subsamples from the core PC-1.

Sl no.	*Sample no*	*Si*	*O*	*Al*	*Ca*	*Fe*	*K*	*Zn*	*Na*	*Cl*
1	PC-1/105	41.97	43.69	6.75	0.85	1.11	5.63	-	-	-
2	PC-1/110	42.01	42.81	6.78	0.2	2.09	5.89	0.22	-	0
3	PC-1/111	40.59	39.55	6.27	2.49	1.11	5.71	0.51	0.77	3.02
4	PC-1/112	35.33	54.37	5.89	0.28	0.16	3.83	0.13	-	-
5	PC-1/115	36.55	52.49	6.19	0.22	0.41	4.14	-	-	-
6	PC-1/116	34.98	53.71	6.14	0.57	0.4	3.93	-	0.53	-
7	PC-1/117	43.26	42.36	6.75	0.81	0.96	5.84	-	-	-

Table 2. Comparison of EDX results of major elemental composition of selected glass shards from sediment core PC-1 with major oxide compositions data taken from various selected literatures.

Sl no	*Location*	*Sample number*	*SiO_2*	*Al_2O_3*	*CaO*	*FeO*	*K_2O*	*Na_2O*
1	South Andaman Sea (PC-1)	*PC-1/105*	*80.21*	*11.39*	*1.06*	*1.28*	*6.06*	*0.00*
2	South Andaman Sea (PC-1)	*PC-1/110*	*79.72*	*11.36*	*0.25*	*2.37*	*6.29*	*0.00*
3	South Andaman Sea (PC-1)	*PC-1/111*	*77.87*	*10.63*	*3.12*	*1.28*	*6.17*	*0.93*
4	South Andaman Sea (PC-1)	*PC-1/112*	*82.22*	*12.11*	*0.42*	*0.23*	*5.02*	*0.00*
5	South Andaman Sea (PC-1)	*PC-1/115*	*81.69*	*12.22*	*0.32*	*0.55*	*5.21*	*0.00*
6	South Andaman Sea (PC-1)	*PC-1/116*	*80.32*	*12.45*	*0.84*	*0.55*	*5.08*	*0.76*
7	South Andaman Sea (PC-1)	*PC-1/117*	*80.69*	*11.12*	*0.99*	*1.08*	*6.13*	*0.00*
8	*Northern Bay of Bengal*	*Gasparotto et al., 2000*	*77.08*	*12.87*	*0.75*	*0.84*	*5.26*	*3.13*
9	*Southern Bay of Bengal*	*Dehn et al., 1991*	*77.54*	*12.53*	*0.8*	*0.83*	*5.15*	*3.02*
10	*CIOB*	*Pattan et al., 1999*	*76.81*	*12.8*	*0.8*	*0.96*	*5.06*	*3.4*
11	*Indian Subcontinent*	*Shane et al., 1995*	*77.15*	*12.67*	*0.78*	*0.86*	*5.08*	*3.26*
12	*South China Sea*	*Lui et al., 2006*	*76.78*	*13.09*	*0.8*	*0.97*	*4.26*	*2.75*

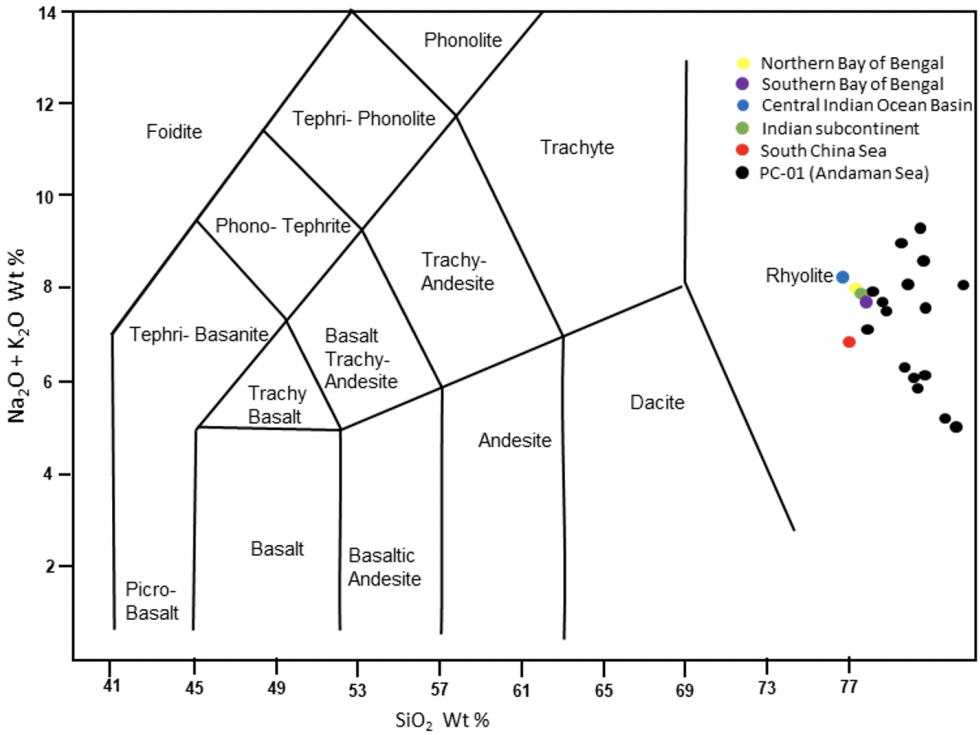

Figure 6. Total alkali silica diagram (TAS) used for volcanic rock nomenclature (Le Bas et al., 1986).

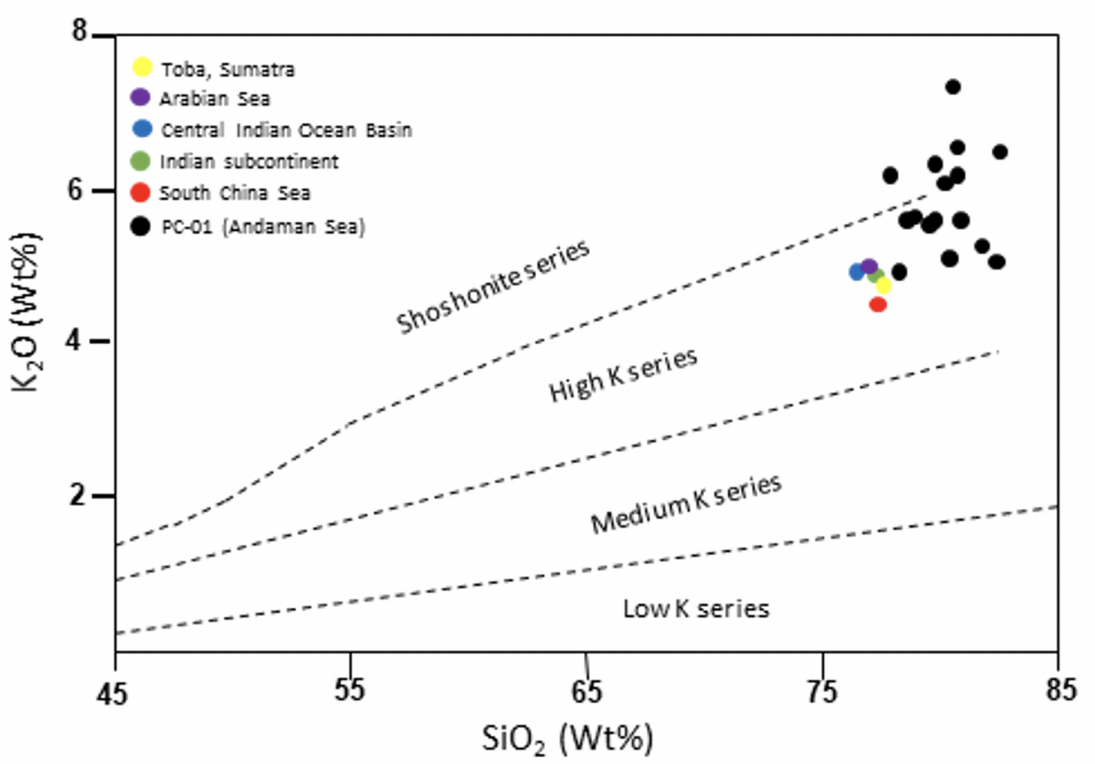

Figure 7. Bivariant diagram showing SiO_2 vs K_2O in which majority of the data fall in the High-K Series (add reference of data)

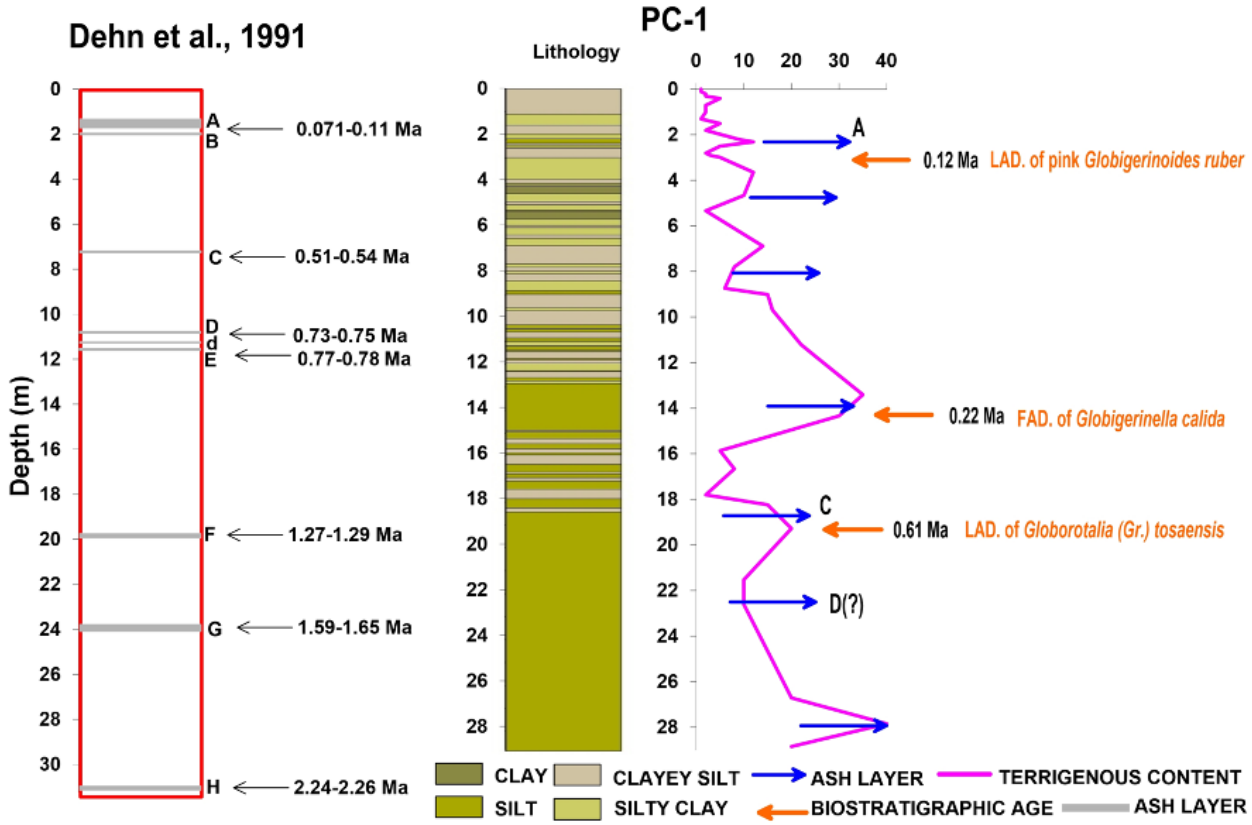

Figure 8. Comparative study plots of ash layers from ODP Site 758 (Dehn et al., 1991) and PC-1 core from South Andaman Sea. Ash layers of PC-1 are marked with the help of relative biostratigraphic datum and also with various ash layer A, B, C and H reported by Dehn et al., 1991 for site 758.

Age Control

In core PC-1, the age control is based on the biostratigraphic study, which are on the basis of first appearance (FAD) and last appearance (LAD) of planktonic foraminifera species namely *Globorotalia (Gr.) tosaensis, Globigerinella Calida* and pink *Globigerinoides ruber*. Based on biostratigraphic datums from tropical oceans (Wade et al., 2011), three datums were identified within the sediment core of PC-1 that correspond to 0.61 Ma (LAD of *Globorotalia (Gr.) tosaensis*) at 18.3 m bsf, 0.22 Ma (FAD of *Globigerinella calida*) at 14.3 m bsf, and 0.12 Ma (LAD of pink *Globigerinoides ruber*) at 3.4 m bsf respectively. Thus, the presence of glass shards at 2.10 m to 2.66 m can be inferred as younger than the 0.12 Ma (Figure 7). This implies that the inferred ash layer may be part of YTT, whereas no such thick unit was observed above 2.10 m, except the presence of thin occurrence of dark brownish green tinted basaltic glass shards at 30 cm bsf. In addition, other thin layer observed below the depth interval between 13.50 m to 14.50 m and 18 m to 24 m, which are potentially correlated to MTT and OTT units (Figure 8). Similar observations were also noticed in the study of Nishimura et al. (1977) and Diehl et al. (1987) suggested eruptions of the Toba caldera at 0.84 Ma and 1.20 Ma respectively. Furthermore, Chesner (1988) also documented several eruptions of the Toba caldera at 0.075, 0.450, 0.840 and 1.2 Ma, which described these layers as the Youngest Toba Tuff (YTT), the Middle Toba Tuff (MTT), the oldest Toba tuff (OTT), and the Haranggoal Dacite Tuff (HDT) respectively. These tephra layers can also be correlated to the sediment core of Site 758 as: YTT to layer A, MTT to layer C, OTT to layer E, and HDT to layer F. Based on previous observations and the present findings, it is possible to correlate that the observed ash layers preserved in the sediment core of PC-1 may be the part of eruptive product of the Toba caldera, such as YTT, MTT and OTT.

CONCLUSIONS

The sediment core PC-1 collected from the South Andaman Sea below the water depth of 3144 m preserved discrete ash layers at various depths, ranging from 2.10 m - 2.66 m, 13.50 m - 14.50 m and 18 m - 24 m. Morphological study of layer-A (56 cm thick) at 2.10 m to 2.66 m represent shards of different varieties with similar glass shards of YTT, as reported from other part of the world. This observation is further corroborated by the biostratigraphic datum, which shows that the layer-A is just above the 0.12 Ma biostratigraphic datum horizons. As a result, the glass shards between 2.10 m to 2.66 m implies YTT and younger than 0.12 Ma. The geochemical composition data obtained from the SEM-EDX analysis suggested high silica and alkali contents indicating rhyolitic composition that display compositional similarity with Toba eruptive products. Further comparative study with IODP core will help to determine the several other eruptive histories, marked as MTT and OTT. Therefore, based on the geochemical composition, morphology and biostratigraphic data, discrete ash layers of PC-1 have similar affinities and possible link to the Toba caldera.

ACKNOWLEDGEMENTS

The authors are grateful to Deputy Director General, M&CSD, ER, GSI for providing all the facilities to complete the objective of cruise SR-03A and Additional Director General, NR, GSI for granting permission to publish this article. Authors express their heartfelt gratitude to Nagendran G., Director and Chief Scientist of the project of SR-03A and SEM Laboratory, GSI, CHQ, Kolkata. Authors would also like to thank the participants of the cruise (SR-03A) for their dedication and hard work throughout the data collection. Special thanks to Late Sanjeev Raghav, Deputy Director General and Supervisory of the project SR-03A for inspiring cruise participants to work beyond the project's established targets and come up with a novel idea to emphasise the said effort.

REFERENCES

Acharyya, S., and Basu, P., 1993. Toba Ash on the Indian Subcontinent and Its Implications for Correlation of Late Pleistocene Alluvium. *Quaternary Research*, 40(1): 10-19.

Basu, P. K., Biswas, S., and Acharyya, S. K., 1989. Late Quaternary ash beds from Son and Narmada basins, Madhya Pradesh. *Indian Minerals*, 41(2): 66–72.

Biswas, S., Basu, P. K., and Sarkar, G. P., 1989: Biostratigraphy of the Quaternary alluvial sediments in the central Narmada basin and the middle Son basin in eastern Madhya Pradesh. *Unpubl. Report Geol. Surv. Ind.* 38p.

Bühring, C., Sarnthein, M., and Leg 184, Shipyard Scientific Party 2000. Toba ash layer in the south China Sea: evidence for contrasting wind directions during eruption Ca. 74 ka. *Geology,* 28(3): 275–278.

Chesner, C. A., 1988. *The Toba Tuff and Caldera Complex, Sumatra, Indonesia: Insight into Magma bodies and Eruptions*. Ph.D. Thesis. Michigan Technology University, Houghton. 428p.

Chesner, C.A., Rose, W.I., 1991. Stratigraphy of the Toba Tuffs and evolution of the Toba Caldera Complex, Sumatra, Indonesia. *Bulletin of Volcanology,* 53: 343-356.

Chesner, C.A., Rose, W.I., Deino, A., Drake, R., 1991. Eruptive history of Earth's largest Quaternary caldera (Toba, Indonesia) clarified. *Geology*. 19(3): 200-203.

Cochran, J. R., 2010. Morphology and tectonics of the Andaman Forearc, northeastern Indian Ocean. *Geophysical Journal International,* 182(2): 631-651.

Curray, J. R., 2005. Tectonics and history of the Andaman Sea region. *Journal of Asian Earth Sciences*, 25(1): 187-232.

Dehn, J., Farrel, J. W., Schmincke, H. U., 1991. Neogene Tephrochronology from site 758 on Northern Nintyeast degree Ridge: Indonesian arc volcanism of past 5 Ma. In: Weissel, J., Peirce, J., et al. (Eds.), *Proceedings of the Ocean Drilling Programme, Scientific Results,* 271: 273-295.

Devdas, V., and Meshram, S. N., 1991. Search for Quaternary ash bed in the Quaternary basins of Orissa. *Records of the Geological Survey of India.* 124(3): 40-42.

Diehl, J.F., Onstott, T.C., Chesner, C.A., Knight, M.D., 1987. No short reversals of Brunhes age recorded in the Toba tuffs, north Sumatra, Indonesia. *Geophysical Research Letters,* 14(7):753-756. https://doi.org/10.1029/GL014i007p00753.

Diehl, T., Waldauser, F., Cochran, J.R., Raju, K.A., Seeber, L., Schaff, D., Eigdahl, E.R., 2013. Back-arc extension in the Andaman Sea: Tectonic and magmatic processes imaged by high precision teleseismic double difference earthquake relocation. *Journal of Geophysical Research: Solid Earth,* 118(5): 2206–2224. 10.1002/jgrb.50192.

Gasparotto, G., Spadafora, E., Summa, V., Tateo, F., 2000. Contribution of grain size and compositional data from the Bengal fan sediment the understanding of Toba Volcanic event. *Marine Geology*, 162(2-4): 561-572.

Izett, G. A., Obradovich, J. D., Naeser, C. W., Cebula, G. T., 1981. Potassium Argon and fission-track zircon ages of Cerro Toledo rhyolite tephra unit in the Jemez mountains, New Mexico; IN Shorter contribution to isotope research in the western United States. *U. S. Geological Survey Professional Paper,* 1199-D: 37-43.

Korisettar, R., Venkatesan, T. R., Misra, S., Rajaguru, S. N., Somayajulu, B. L. K., Tandon, S. K., Gogate, V. D., Ganjoo, R. K., Kale, V. S., 1989. Discovery of a tephra bed in the Quaternary alluvial sediments of Pune district (Maharashtra), Peninsular India. *Curr. Sci*. 58(10): 564–567.

Le Bas, M.J., Le Maitre, R.W., Streckeisen, A. and Zanettin, B., 1986. A Chemical Classification of Volcanic Rocks Based on the Total Alkali-Silica Diagram. *Journal of Petrology,* 27(3): 745-750. https://doi.org/10.1093/petrology/27.3.745.

Le Maitre, R.W., Bateman, P., Dudek, A.J., Keller, M.J., 1989. *A Classification of Igneous Rocks and Glossary of Terms*, Blackwell, Oxford, 193.

Liang, X., Wei, G., Shao, L., Li, X., Wang, R., 2001. Records of Toba eruptions in South China Sea. *Science in China*, 44(10): 871-878. doi:10.1007/bf02907078.

Liu Z., Colin, C., Trentesaux, A., 2006. Major element geochemistry of glass shards and minerals of the Youngest Toba Tephra in the southwestern South China Sea. *J. Asian Earth Sci.* 27(1): 99-107.

McCaffrey, R., 1991. Slip vectors and stretching of the Sumatran fore-arc. *Geology*, 19: 881-884.

Morley, C.K. 2017. Cenozoic rifting, passive margin development and strike-slip faulting in the Andaman Sea: a discussion of established v. new tectonic models. In: Bandopadhyay, P.C. & Carter, A. (eds) The Andaman-Nicobar Accretionary Ridge: Geology, Tectonics and Hazards. *Geological Society London, Memoirs*, 47: 27-50.

Ninkovich, D., Sparks, R.S.J., Ledbetter, M.T., 1978. The exceptional magnitude and intensity of the Toba eruption, Sumatra: an example of the use of deep-sea tephra layers as a geological tool. *Bulletin Volcanologique,* 41(3): 286-298.

Nishimura, S., Abe, E., Yokoyama, T., Wirasantosa, S., Dharma, A., 1977. Danau Toba – The outline of lake Toba, North Sumatra, Indonesia. *Paleolimnology of Lake Biwa and the Japanese. Pleistocene*, 5: 313-332.

Oppenheimer, C., 2002. Limited global change due to largest known Quaternary eruption, Toba w74kyr BP? *Quaternary Science Review,* 21(14-15): 1593-1609.

Pattan J.N., Shane P Banakar V.K., 1999. New occurrence of youngest Toba Tuff in abyssal sediments of the Central Indian Basin. *Marine Geology,* 155(3-4): 243–248.

Pattan, J.N., Pearce, N.J.G., Banakar, V.K., Parhiban, G., 2002. Origin of ash in the CIOB and its implications for the volume estimate of the 74,000yr BP Youngest Toba eruption. *Current Science,* 83(7): 889-893.

Pattan, J.N., Prasad, M.S., Babu, E.V.S.S.K., 2010. Correlation of the oldest Toba Tuff to sediments in the central Indian Ocean Basin. *Journal of Earth Systems Science*, 119(4): 531-539.

Pearce, N.J.G., Westgate, J.A., Gatti, E., Pattan, J.N., Parthiban, G., Achyuthan, H., 2014. Individual glass shard trace element analyses confirm that all known Toba tephra reported from India is from the c.75-ka Youngest Toba eruption. *Journal of Quaternary Science,* 29(8): 729-734.

Rachna Raj., 2008. Occurrence of Volcanic ash in the Quaternary alluvial deposits, lower Narmada basin, Westen India. *Journal of Earth Systems Science*, 117: 41-48.

Robock, A., C. M., Ammann, L., Oman, D., Shindell, S. Levis., G. Stenchikov., 2009. Did the Toba volcanic eruption of 74 ka B.P. produce widespread glaciation? *J. Geophys. Res.,* 114.

Rose, W. I., and Chesner, C. A., 1987. Dispersal of ash in the great Toba eruption, 75 Ka. *Geology*, 15(10): 913-917.

Schulz, H., von Rad, U., Erlenkeuser, H., 1998. Correlation between Arabian Sea and Greenland climate oscillations for the past 110,000 years. *Nature*, 393(6680):54-57.

Shane, P., Westgate, J., Williams, M., & Korisettar, R., 1995. New Geochemical evidence for the Youngest Toba Tuff in India. *Quaternary Research*, 44(2): 200-204. doi:10.1006/qres.1995.1064.

Smith, R.L., Bailey, R.A., 1968. Resurgent cauldrons. In: Coats, R.R., Hay, R.L., Anderson, C.A. (Eds.), Studies in Volcanology. *Geological Society of America*, *Memoir*, 116: 613-662.

Song, S. R., Chen, C-H., Lee, M. Y., Yang, T. F., Iiznka, Y. and Wie, K. Y., 2000. Newly discovered eastern dispersal of the youngest Toba Tuff. *Mar. Geol.,* 167(3-4): 303–312.

Tripathi S. K., Nagendran, G., Karthikeyan, M., Tripathy, S. K., Varghese, S., and Raghav, S., 2018. Morphology of submarine volcanic seamounts from inner volcanic arc of Andaman Sea. *Indian Journal of Geosciences*, 71(3): 451-470.

Wade, B.S., Pearson, P.N., Berggren, W.A., Hälike, H., 2011. Review and revision of Cenozoic tropical planktonic foraminiferal biostratigraphy and calibration to the geomagnetic polarity and astronomical time scale. *Earth-Science Reviews*, 104(1-3): 111–142. https://doi.org/10.1016/j.earscirev.2010.09.003.

Westgate, J. A. and Gorton, M. P., 1981. Correlation techniques in tephra studies. In: Self, S. and Sparks, R. S. J. (Eds), *Tephra Studies. NATO Advanced Study Institutes Series*, 75: 73-94. Springer, Dordrecht. https://doi.org/10.1007/978-94-009-8537-7_5.

William, M. A. J., and Clarke, M. F., 1984. Late Quaternary environments in north-central India. *Nature* 308(5960): 633–635.

William, M. A, J., and Royce, K., 1982. Quaternary geology of the middle Son valley, north central India: implications for prehistoric Archaeology. *Palaeogeography Palaeclimatology Palaeoecology,* 38(3-4): 139-162.

Zielinski, G.A., Mayewski, P.A., Meeker, L.D., Whitlow, S., and Twickler, M.S., 1996. Potential atmospheric impact of the Toba mega-eruption ~71,000 years ago. *Geophysical Research Letters,* 23(8): 837-840.

SEDIMENTATION RATES AND CALCAREOUS NANNOFOSSIL BIOSTRATIGRAPHY OF THE NANGGULAN FORMATION, KULON PROGO, INDONESIA

TINGKAT SEDIMENTASI DAN BIOSTRATIGRAFI NANNOFOSIL FORMASI NANGGULAN, KULON PROGO, INDONESIA

Resti Samyati Jatiningrum[1*], Rivdhal Saputra[2], Gaudensia Phang[1], Tokiyuki Sato[3]

[1] Geological Engineering Program Study, Faculty of Exploration and Production Technology, Universitas Pertamina, Jl. Teuku Nyak Arief, Jakarta 12220, Indonesia

[2] PT. Geoservices, Jalan Minangkabau Barat No. 34, Setiabudi, Jakarta Selatan

[3] Graduate School of International Resource Sciences, Department of Earth Resource Science, Faculty of International Resource Science, Akita University

*Corresponding author: resti.sj@universitaspertamina.ac.id

(Received 28 June 2022; in revised from 30 June 2022; accepted 29 July 2022)

DOI : 10.32693/bomg.37.1.2022.766

ABSTRACT : The Nanggulan Formation is the oldest sedimentary rock of Paleogene age that was deposited in the eastern part of the Southern Central Java Basin. A total of 103 nannofossil samples were taken from two traverses in the study area, i.e., the Watupuru and Jetis Routes. Based on the biodatum identified from the nannofossil samples, the biostratigraphy of the rock formation is divided into five zonations, namely the upper part of Zone NP16, Zone NP17, the lower part of Zone NP18, the upper part of Zone NP22, and the lower part of Zone NP23, expanding from 41.1 Ma to 32.2 Ma of age (Middle Eocene to Early Oligocene). Only Zone NP17 is identified as a complete zone, whereas the other four are observed as partial. The fluctuation of global sea level is believed to be an influence on the deposition of the Nanggulan Formation. The sedimentation rate and the change of nannofossil species shows a decrease of oligotrophic (Sphenolithus) and an increase of eutrophic (Reticulofenestra) taxa, especially in small reticulofenestrids (Reticulofenestra spp.). This occurrence suggests a shift in the environmental conditions from an oligotrophic condition around 41.1 Ma to a eutrophic one, particularly after 40.40 Ma. The enhanced eutrophication in the Watupuru and Jetis Routes was caused by an increasing terrigenous input in 40.40 Ma and after, consequently providing nutrient availability on the water surface. This interpretation is supported by the increase in the sedimentation rate when sea level slightly decreased in 40.40 Ma.

Keywords: Nanggulan formation, calcareous nannofossil, biostratigraphy, sedimentation rate

ABSTRAK*:* Formasi Nanggulan merupakan sedimen berumur Paleogen dan endapan sedimen paling tua di Jawa bagian timur yang diendapkan di Cekungan Jawa Tengah Selatan. Sebanyak 103 sampel nannofosil diambil dari dua lintasan di Formasi Nanggulan: Watupuru dan Jetis. Berdasarkan biodatum yang diidentifikasi dari sampel nannofosil, biostratigrafi Formasi Nanggulan dibagi menjadi 5 zonasi. Terdapat empat zona kisaran sebagian dan satu zona kisaran sebagai berikut: Zona NP16 bagian atas, Zona NP17, Zona NP18 bagian bawah, Zona NP22 bagian atas dan Zona NP23 bagian bawah. Berdasarkan studi biostratigrafi, Formasi Nanggulan diendapkan pada umur 41,1 juta tahun sampai dengan 32,2 juta tahun (Eosen Tengah hingga Oligosen Awal). Menurut distribusi lithofasies secara horizontal, pengendapan Formasi Nanggulan dipengaruhi oleh fluktuasi muka air laut. Laju sedimentasi dan perubahan nannofosil juga dianalisis dalam penelitian ini. Adanya pengurangan taksa oligotrofik (*Sphenolithus*) dan peningkatan taksa eutrofik (*Reticulofenestra*) terutama *Reticulofenestra* berukuran kecil (*Reticulofenestra* spp.) menunjukkan adanya perubahan kondisi lingkungan dari oligotrofik pada umur 41,1 juta tahun menjadi eutrofik pada umur 40,40 juta tahun. Peningkatan eutrofik di rute Watupuru dan Jetis diakibatkan oleh adanya penambahan material darat hasil erosi pada umur 40,40 juta tahun dan setelah umur 40,40 juta tahun sehingga meningkatkan ketersediaan nutrisi di permukaan laut. Interpretasi ini didukung oleh adanya peningkatan laju sedimen ketika permukaan air laut sedikit menurun pada umur 40,40 juta tahun.

Kata Kunci: Formasi Nanggulan, nanofosil gampingan, biostratigrafi, kecepatan sedimentasi

INTRODUCTION

The Nanggulan Formation is reported by Van Bemmelen (1949) and Rahardjo et al. (1977) as Paleogene sedimentary rock. It is known as the oldest sediment of the eastern part of Java that was deposited in the Southern Central Java Basin (Satyana, 2005). The formation outcropped locally in Watupuru and Jetis River in Nanggulan sub-regency, Kulon Progo Regency, Yogyakarta Special Province, approximately 30 kilometers to the west of Yogyakarta (Figure 1). The age of the Nanggulan Formation ranges from Middle Eocene to Early Oligocene (Purnamaningsih and Pringgoprawiro, 1981; Rahardjo et al. 1995; Lelono, 2000; and Widagdo et al., 2016), based upon its microfossil analysis. The lithology in the Nanggulan Formation comprises foraminifera, mollusks, as well as pollen and spores. However, derived from several studies regarding biostratigraphy that have been done in the Nanggulan Formation, calcareous nannofossils are rarely used. The previous studies using calcareous nannofossils in the Nanggulan Formation was carried out by Okada (1981), followed by Lunt and Sugiatno (2003) and Saputra and Akmaluddin (2015).

Through a new high-resolution calcareous nannofossil biostratigraphy and a paleoceanographic interpretation derived from detailed lithostratigraphy and calcareous nannofossil data, as well as sedimentation rates, this study aims to reconstruct the paleoceanographic condition of the Nanggulan Formation within the range of its depositional age.

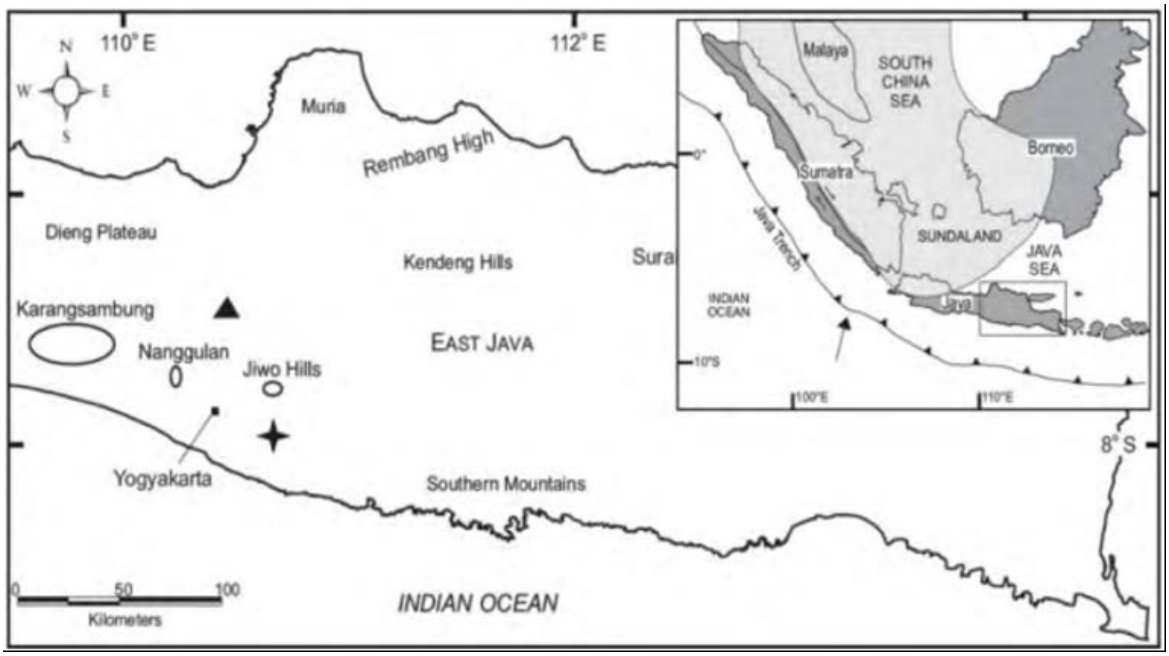

Figure 1. Study area located in the Nanggulan Area. Significant Paleogene sites in the eastern part of Java (Smyth et al. 2008) are marked with ellipse.

sandstones with intercalated lignites, sandy siltstones, claystones with limonite concretions, intercalated marls and limestones, and tuffaceous sandstones. According to Purnamaningsih and Pringgoprawiro (1981), the upper part of this formation consists of marls and calcareous sandstones that are also known as the Seputih Member. The Nanggulan Formation is also a part of the Nanggulan Anticline, which extends relatively north-northeast to south-southwest.

Much extensive research projects have been done in the Nanggulan Formation with regard to sedimentology, geological structure, and palaeontology. According to Saputra and Akmaluddin (2015), the Nanggulan Formation is known for its high variety and good preservation of fossils. Among the varieties of fossils that can be found in this formation include calcareous nannofossil, large benthic foraminifera, benthic

MATERIAL AND METHODS

A total of 103 samples were taken from two traverses: the Watupuru and Jetis Routes. Sampling in the Watupuru Route was accomplished using intervals of ~9 m on average; whereas in the Jetis Route, the sampling was carried out at intervals of ~3 m. Samples for calcareous nannofossil analysis were obtained from fine-grained sedimentary rocks, i.e., claystone, siltstone, sandy siltstone, and very fine sandstone.

Smear slides were prepared from unprocessed sediment samples following the standard technique by Bown and Young (1998) and then were observed under the polarized microscope with immersion oil at 1000x - 1500x magnification. In this study, calcareous nannofossils from each slide were analyzed using a semi-quantitative method. For each smear slide, at least 200 specimens were counted and identified based upon Perch-Nielsen (1985),

Farinacci (1969), and Bown (1998) to comprehend the distribution and relative abundance of nannofossil taxa presented in the smear slide. Two to three additional long traverses were scanned to identify the presence of rare taxa or key species for biostratigraphic study. By this means, the calcareous nannofossil zonation is determined after the standard zonation of Martini (1971), Fornaciari et al. (2010), Agnini et al. (2014), and Fioroni et al. (2015) for deducing their absolute age. The sedimentation rate calculation was attained from the age versus thickness/ depth cross-plot diagram.

RESULTS

Watupuru Route

The Watupuru Route extends from northwest to southeast, consisting of 18 outcrops exposed along the Watupuru River. The total thickness of the outcrops is estimated at around 207 m with an average strike-dip orientation of 215/13.80 NW (Figure 2).

a. Lithofacies

The lithology found along this route (Figure 3) can be divided into lower, middle, and upper parts. The lower part of the route consists of a thin coal bed intercalation, fine to

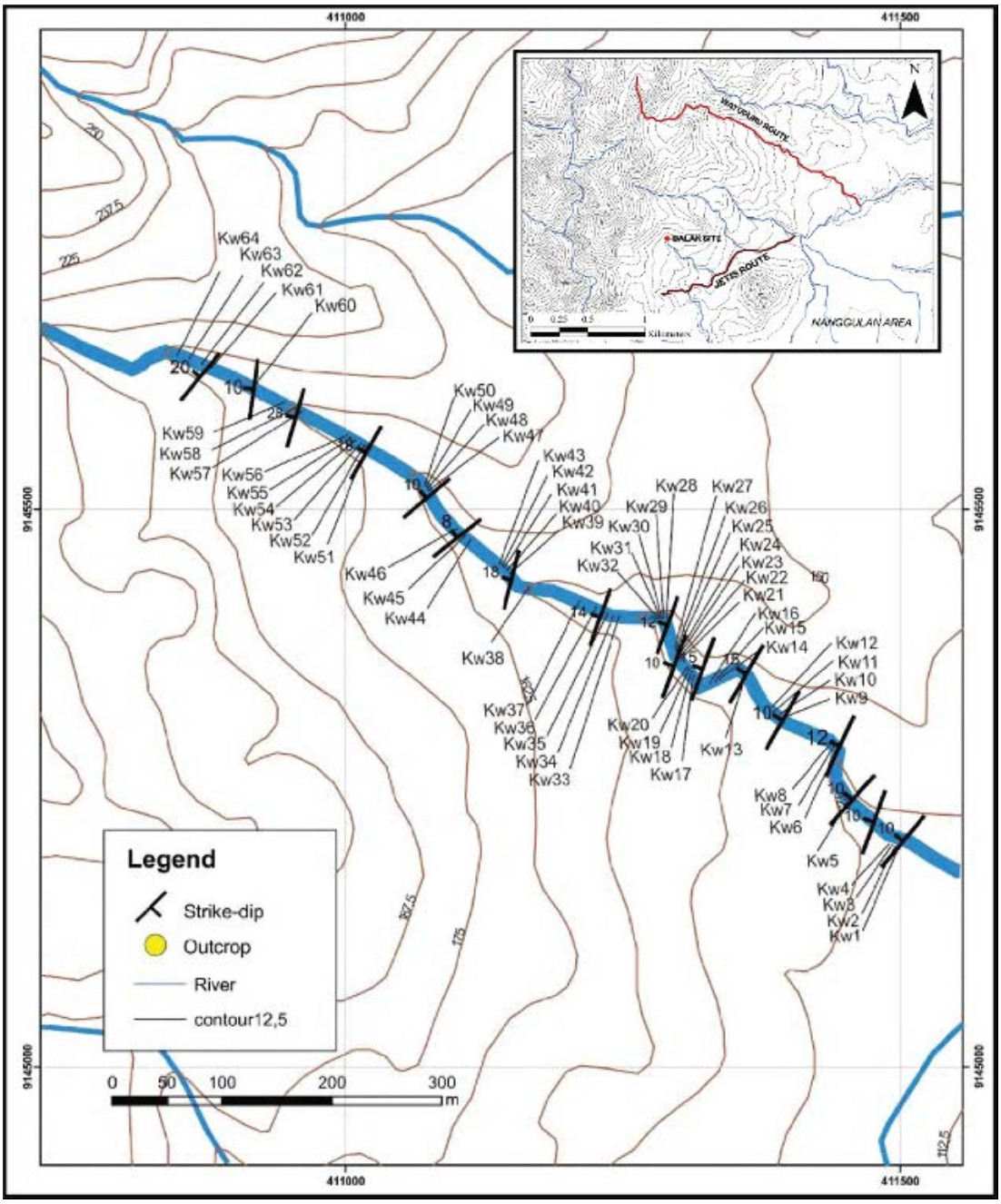

Figure 2. Sample distribution of the Watupuru Route with strike-dip orientation.

very fine sandstones, siltstones, and sandy siltstones. The coal is a lignite type with a thickness of 20 cm and has a black color and a dull luster. The fine sandstone has dark bluish gray to light gray colors with a thickness of around 30 cm to 80 cm. The sedimentary structures present in the sandstones are normal grading, blocky, hummocky cross-stratification, and parallel lamination. The siltstone shows a massive structure with a thickness varying from 30 cm to 120 cm with minor bioturbation and contains mollusks and foraminifera fossils.

The lithology in the middle part of the Watupuru Route generally consists of siltstones with occasional intercalations of sandstones. The siltstone has a dark greenish to bluish-gray color and a massive structure with a thickness of more than 1 m. The bioclast consists of mollusks and foraminifera fragments and is increasing upward. A secondary structure such as concretion is present. The sandstone is generally fine to very fine-grained with a thickness varying from 15 cm to 1 m and contains bioclasts of mollusks and foraminifera with

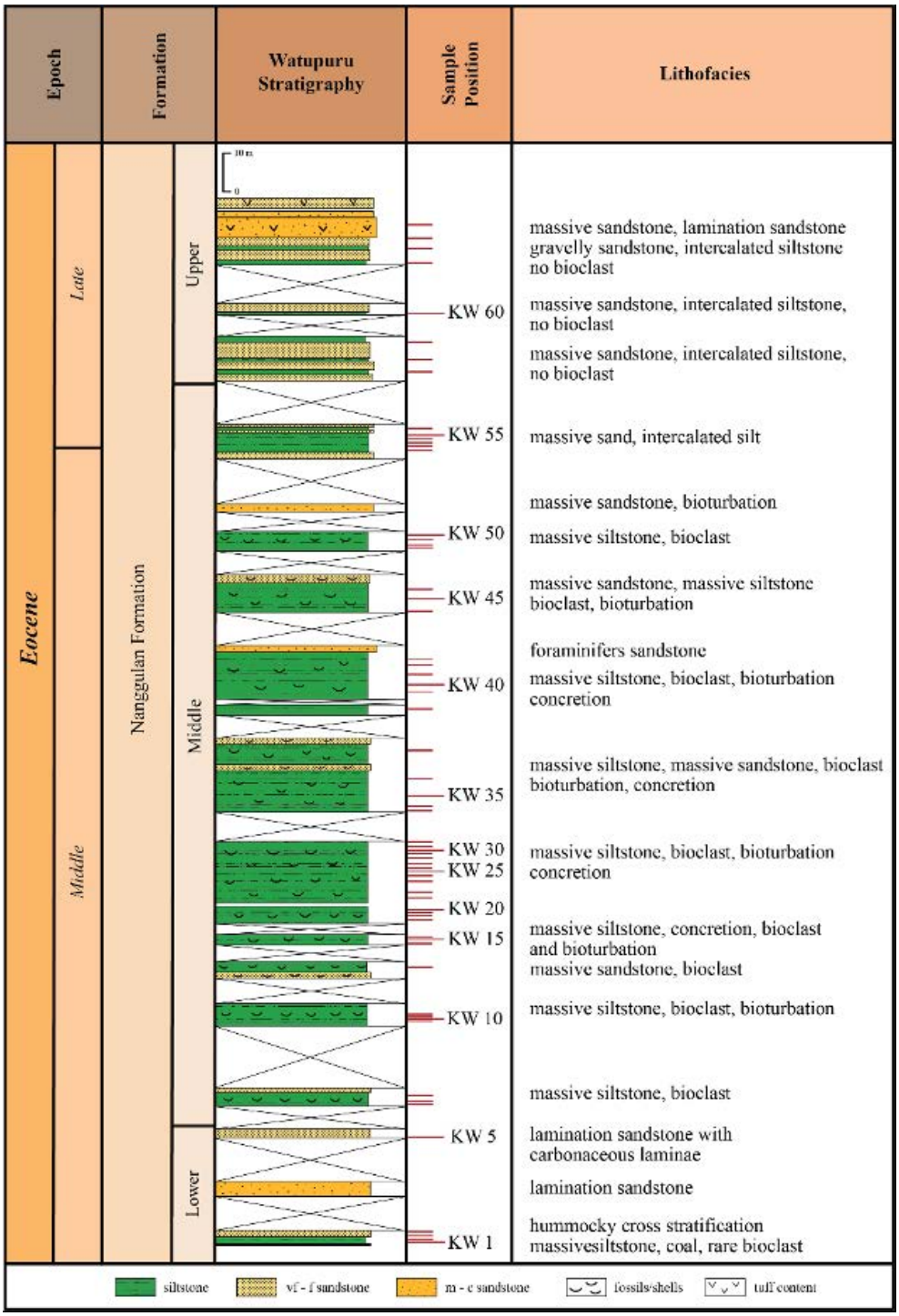

Figure 3. Summary of the Watupuru Route's lithofacies and sampling positions

minor bioturbation. Aside from that, there is also a 2-m-thick coquina-type foraminiferal sandstone with a substantial number of foraminiferal bioclasts.

There is a change of lithology pattern in the upper part of the route. The siltstones are decreasing and sandstones with coarser grains are more dominant. The sandstone is generally medium to coarse-grained with a dark gray color, showing a change in composition. At the uppermost part of the route, gravelly sandstone is present and the bioclast is scarce.

b. Biostratigraphy

The biostratigraphy of this route begins at Zone NP16, which is a partial range zone. The bottom boundary of this zone cannot be identified. The zonal boundary between Zone NP16 and Zone NP17 is detected in the middle part of the section, which is marked by the last occurrence of *Chiasmolithus solitus*. *Dictyococcites bisectus* is also present within this zone. However, the occurrence is delayed until later. The top boundary of Zone NP17 is marked by the last occurrence of *Sphenolithus spiniger*, the last occurrence of *Sphenolithus furcatolithoides*, and the last occurrence of *Chiasmolithus gigas*. Agnini et al. (2014) and Okada & Bukry (1980) marked the boundary between Zone NP17 and Zone NP18 using *Chiasmolithus gigas* as the biodatum, separating the Middle Eocene and the Late Eocene. However, in this study, the presence of this species is not reliable to take into account due to Zone NP18 being a partial range zone with an undefined top boundary. There is no record of nannofossil occurrence in most samples above KW-60 (Figure 4).

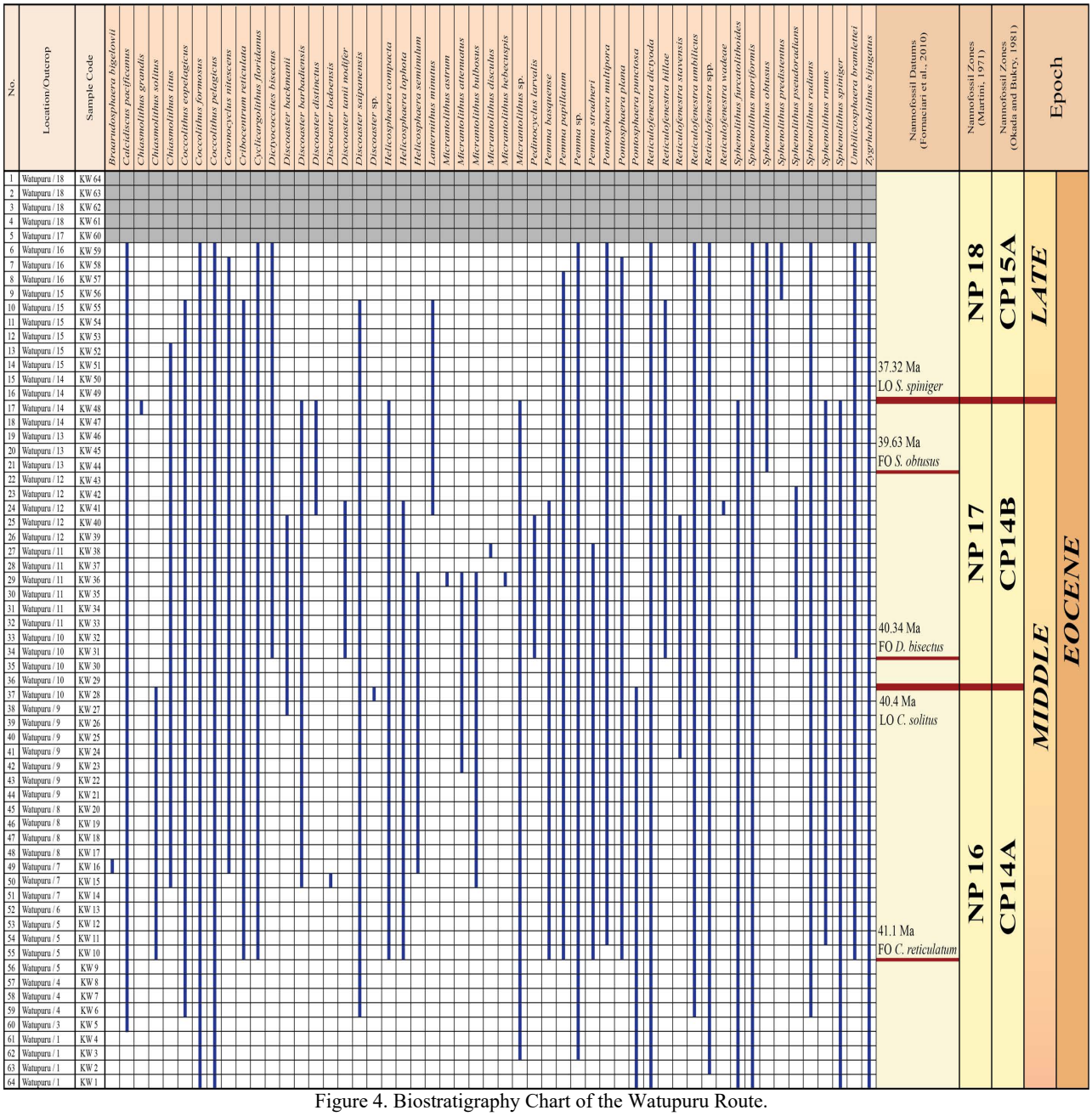

Figure 4. Biostratigraphy Chart of the Watupuru Route.

Table 1. Biodatums and numerical ages used in biostratigraphy study in the Watupuru Route.

Biodatum	Position (Interval)	Age (Ma)			
		Fioroni et al. (2015)	Agnini et al. (2014)	Savian et al. (2013)	Fornaciari et al. (2010)
LO *Sphenolithus spiniger*	137.5 m	-	37.32	-	-
FO *Sphenolithus obtusus*	117 m	39.0	-	-	39.63
FO *Dictyococcites bisectus*	79 m	39.0	40.34	-	-
LO *Chiasmolithus solitus*	77 m	38.7	-	40.40	38.40
FO *Cribocentrum reticulata*	45 m	41.3	42.37	-	41.1

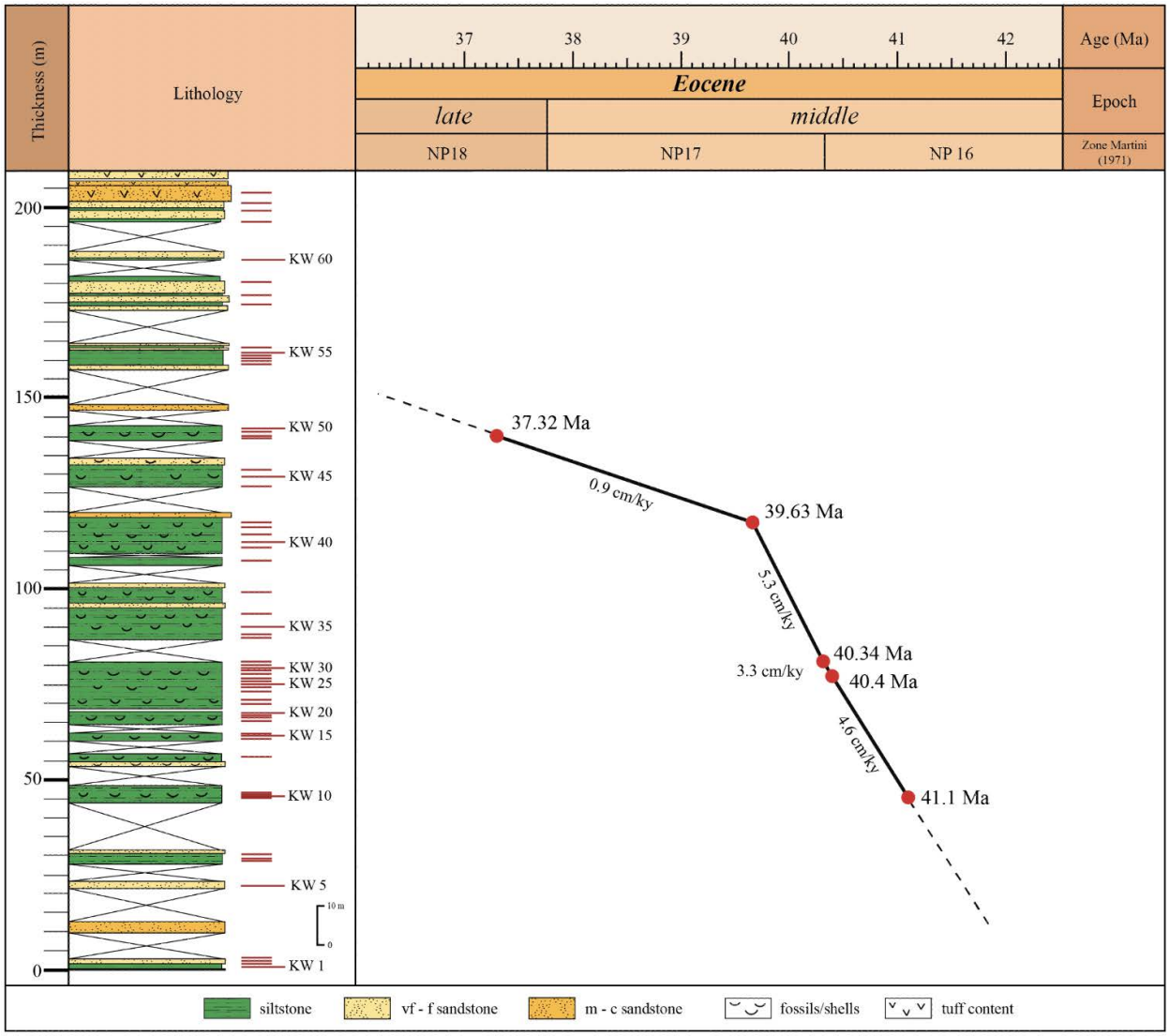

Figure 5. Age versus depth/thickness cross-plot of the Watupuru Route and its sedimentation rates.

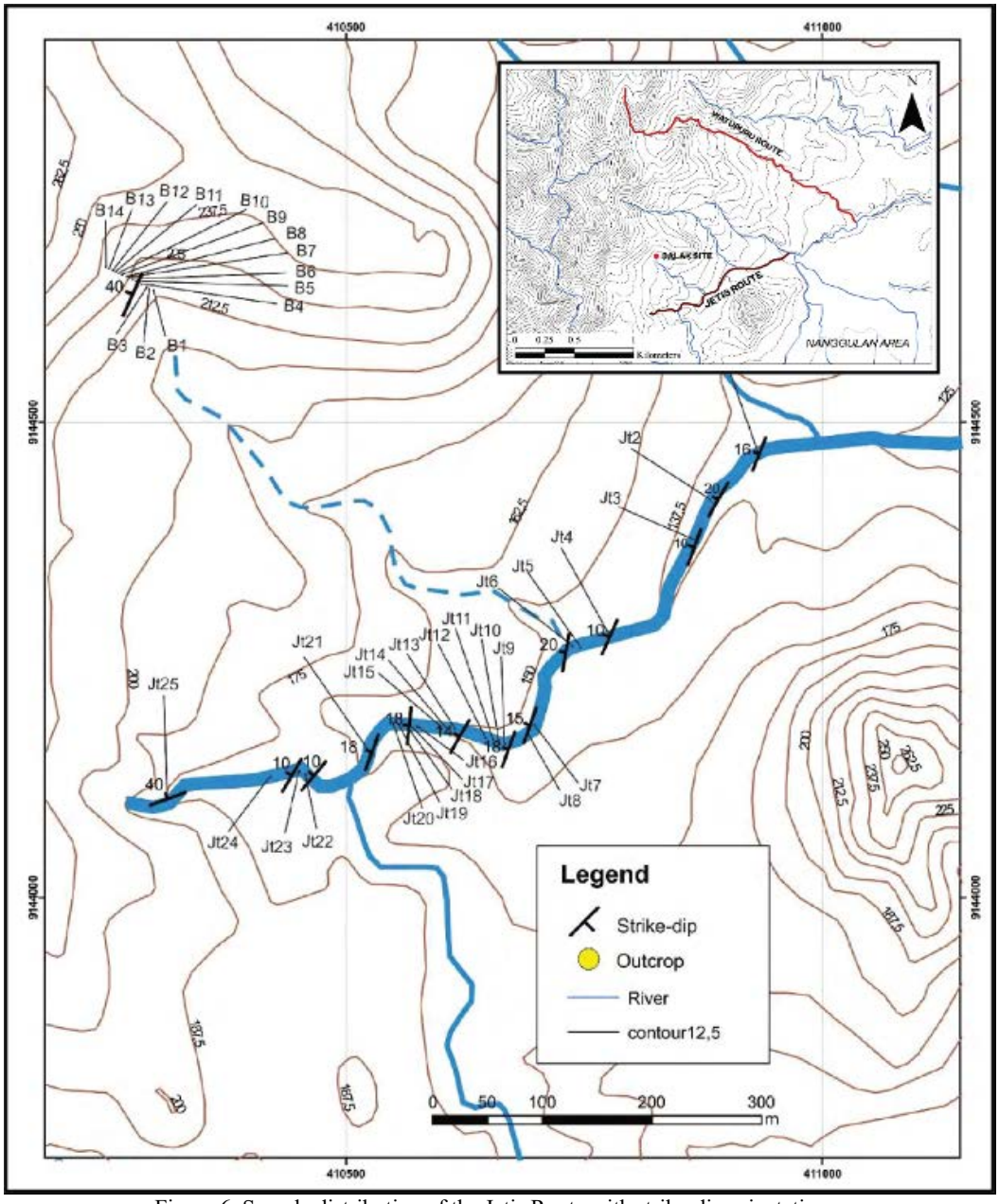

Figure 6. Sample distribution of the Jetis Route with strike-dip orientation.

c. Sedimentation Rate

In accordance with the biodatum identified by calcareous nannofossils taken from the Watupuru Route (Table 1), the sedimentation rates for this section differ, showing four depositional sequences (Figure 5). The first sequence is the 45–77 m interval with the sediment accumulation rate of 4.6 cm/kyr in the age period ranging from 41.1 Ma to 40.40 Ma. The second sequence is the interval of 77–79 m accumulated between 40.40 Ma and 40.34 Ma and has the sediment accumulation rate of 3.3 cm/kyr. The third sequence starts from 79 m to 117 m positions dated 40.34 Ma to 39.63 Ma and reveals the sedimentation rate of 5.3 cm/kyr. The last sequence is in the interval of 117 m to 137.5 m, deposited from 39.63 Ma to 37.32 Ma with the sedimentation rate of 0.9 cm/kyr. The average sedimentation rate of the Watupuru Route is 3.5 cm/kyr, approximately.

Jetis Route

The Jetis Route lengthens from the northwest to southeast, consists of 19 outcrops in which 18 of them are exposed along the Songgo River and Seputih River in Jetis Village and the one outcrop is in Balak (Figure 6). The total thickness of this route is estimated at about 197 m with average strike-dip orientation of 189/17.50 NW.

a. Lithofacies

The lithofacies summary of the Jetis Route is shown in Figure 7. The route is divided into lower, middle, and upper parts. The lower part of the Jetis Route comprises sandstone-siltstone intercalations. The condition of this

part is weathered; thus, some sedimentary structures are not clearly recognizable. The sandstones are generally fine to very fine-grained with light greenish to bluish-gray colors. Their thicknesses vary from 40 cm to 1.5 m. The sedimentary structures noticed in this part are massive structures and laminations. The sandstones contain bioclasts of mollusks and foraminifera with minor bioturbations. The siltstones have dark greenish to bluish-gray colors, and the sedimentary structure of massive structures. Their thicknesses vary from 30 cm to 1 m. Mollusks and foraminifera bioclasts, as well as some minor bioturbations, can be found in the siltstones. The

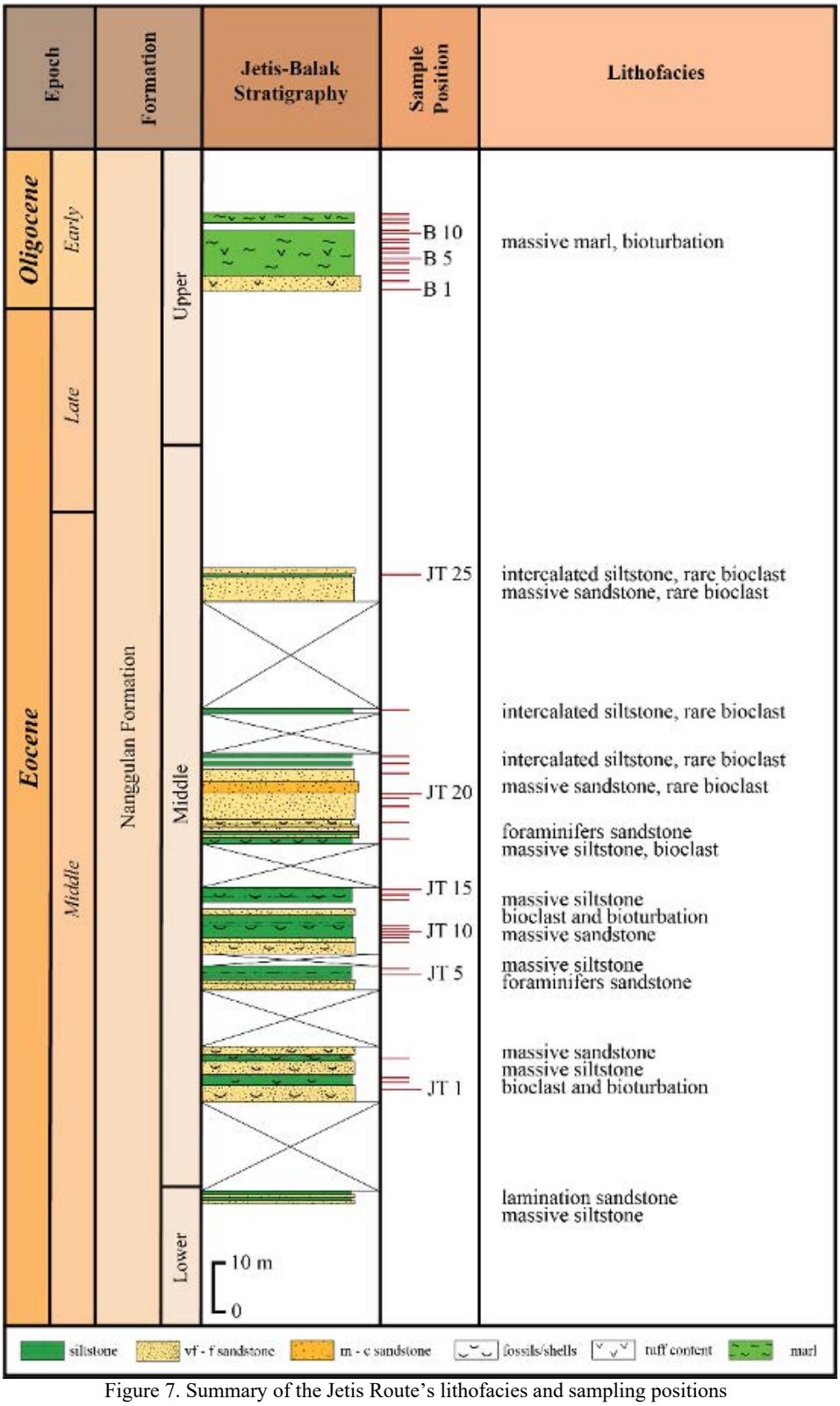

Figure 7. Summary of the Jetis Route's lithofacies and sampling positions

secondary structure of concretions is present in both lithofacies.

The lithofacies in the middle part of the Jetis Route are fairly similar to those in the lower part. However, the occurrence and thickness of the siltstones alternated with sandstones are gradually increasing. In general, the sedimentary structure is massive with minor bioturbations. Concretion is present in both sandstone and siltstone. There is also coquina-type foraminifera sandstone present with a considerable amount of bioclasts, mainly of larger benthic foraminifera, such as *Discocyclina*. The coquina is dark green in color and matrix-supported, with medium sand as the matrix. This type of sandstones develops as of about 1 m-intercalations between the sandstones and siltstones in two of the outcrops.

The upper part of the Jetis Route generally consists of bedded sandstones with intercalations of siltstones. The sandstone is dark gray in color, mostly fine to medium-grained. However, coarse sandstone is also present in some outcrops. The sandstone is massive, laminated, or normal graded with minor bioturbations. The bioclasts are sparse in sandstones. Siltstone appears as intercalations showing massive or blocky structure and commonly has dark greenish to bluish-gray colors with few bioclasts.

The youngest part of this route, the Balak Site, is exposed along the slope of Menoreh Hill, around 500 m to the north of the river. Between the last sampling site of the Jetis Route and the Balak Site, there is no outcrop exposed in the vicinity, which then is interpreted as a gap of time. This site is considered a part of the Jetis Route due to its near-by location and possesses a similar strike-dip orientation in general. The Balak Site consists of marlstones and limestones in gray to white colors. They are rich in carbonate material, and bioturbations are also present. There are no bioclasts or rock fragments found in the outcrop. Their sedimentary structure is mostly massive with the grain size of very fine sand or silt.

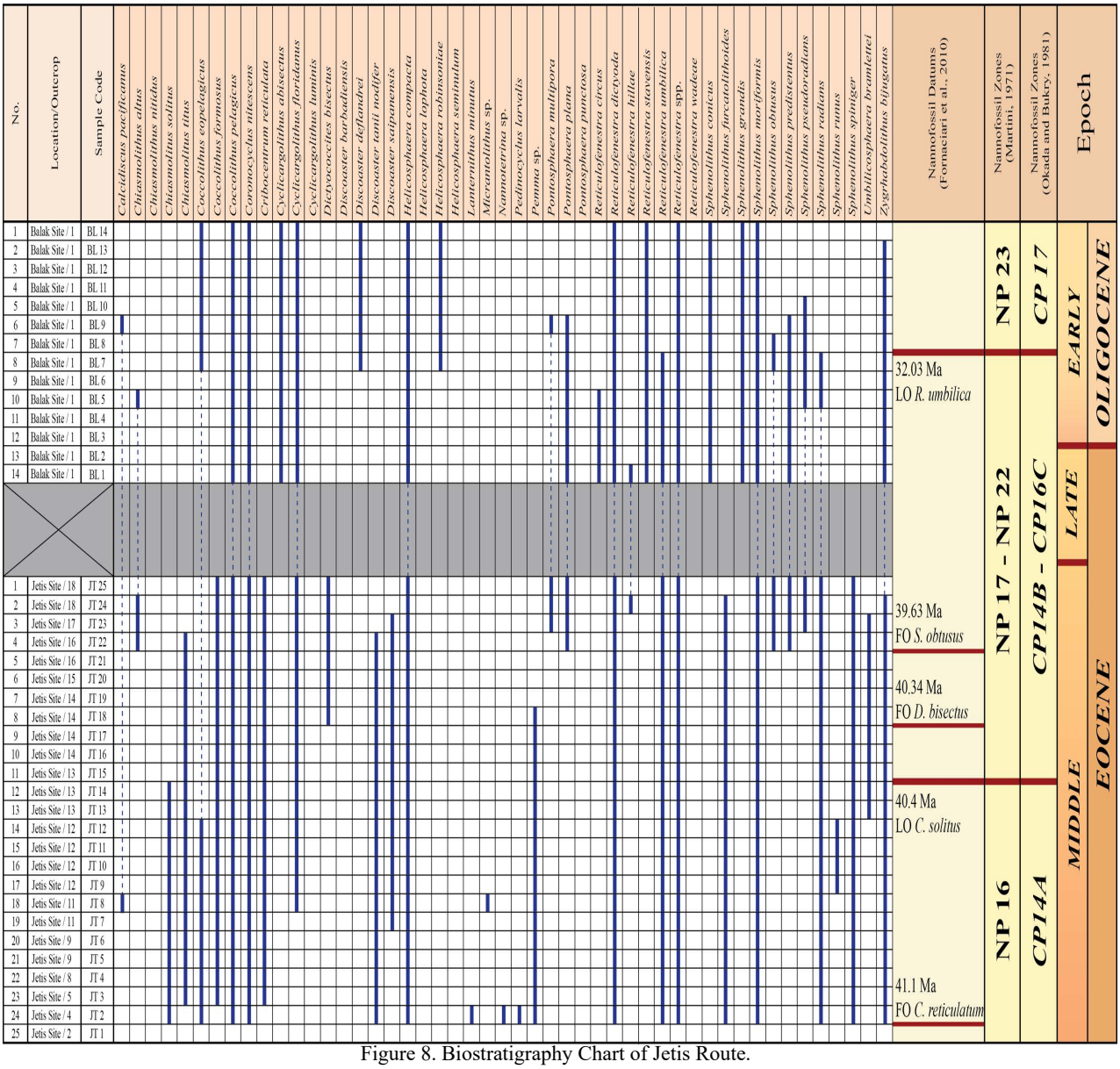

Figure 8. Biostratigraphy Chart of Jetis Route.

Table 2. Biodatum and numerical age used in Jetis Route biostratigraphy study.

Biodatum	Position (Interval)	Age (Ma)			
		Fioroni et al. (2015)	Agnini et al. (2014)	Savian et al. (2013)	Fornaciari et al. (2010)
LO *Reticulofenestra umbilica*	198.5 m	31.05	32.02	32.30	-
FO *Sphenolithus obtusus*	92.4 m	39.0	-	-	39.63
FO *Dictyococcites bisectus*	83.4 m	39.0	40.34	-	-
LO *Chiasmolithus solitus*	57.6 m	38.7	-	40.40	38.40
FO *Cribocentrum reticulata*	25.3 m	41.3	42.37	-	41.1

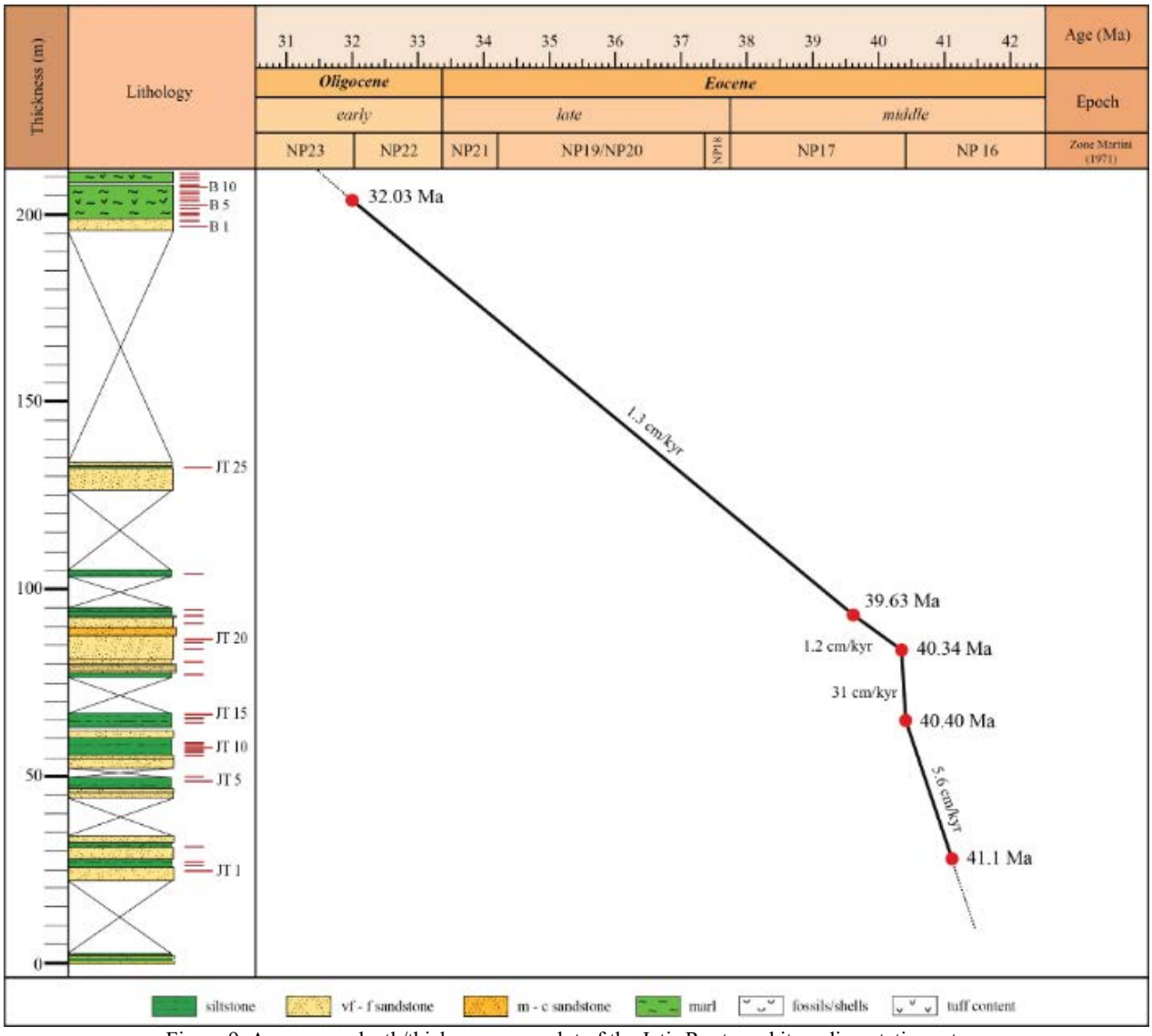

Figure 9. Age versus depth/thickness cross-plot of the Jetis Route and its sedimentation rates.

b. Biostratigraphy

There are two calcareous nannofossil zones identified in the Jetis Route and two additional zones identified in the Balak Site (Figure 8). The Jetis Route's biostratigraphy starts from Zone NP16, indicated by the first occurrence of *Cribocentrum reticulatum*, which is also used as an additional biodatum to characterize the lower part of Zone NP16. The zonal boundary between Zone NP16 and Zone NP17 is observed in the middle part of the section of the Jetis Route, identified by the last occurrence of *Chiasmolithus solitus*. In this section, the first occurrence of *Dictyococcites bisectus* characterizes the base of Zone NP17, whereas the first occurrence of *Sphenolithus obtusus* characterizes the upper part of Zone NP17. Zone NP17 is considered a partial zone since its top boundary cannot be identified.

Between the Jetis Route and the Balak Site, there is a 60 m lithological gap shown by no outcrops present in the upper part of the section. At the Balak Site, the zonal boundary of NP22/NP23 is determined by the last occurrence of *Reticulofenestra umbilica*, hence resulting in NP22 and NP23 as two partial zones. There is only one biodatum identified in this section, indicating a much younger age of Early Oligocene.

c. Sedimentation Rate

Based on the biodatum identified from calcareous nannofossil samples of the Jetis Route (Table 2), the sedimentation rates of this section is divided into four sequences (Figure 9).

The first sequence is from 41.1 Ma to 40.4 Ma, encompassing from 25.3 m to 64.8 m with a sediment accumulation rate of 5.64 cm/kyr. The second sequence is between 40.4 Ma and 40.34 Ma and is situated at 64.8 m to 83.4 m with a sedimentation rate of 31 cm/kyr. The third sequence is located at 83.4 m to 92.4 m, dated 40.34 Ma to 39.63 Ma, and has a sedimentation rate of 1.26 cm/kyr. The fourth sequence's age is 39.63 Ma to 37.7 Ma and was discovered at 92.4 m to 198.5 m, showing a sedimentation rate of 1.39 cm/kyr. The average sedimentation rate of the Jetis route is circa 9.82 cm/kyr.

DISCUSSION

Biostratigraphy of Nanggulan Formation

The biostratigraphy study shows that the Nanggulan Formation was deposited in the Middle Eocene to Early Oligocene, or according to the biozonation of Martini (1971), is equal to NP16 to NP23. It is also equal to CP14A-CP17 which was based on Okada & Bukry (1980), or to CNE15-CNO3, assumed by Agnini et al. (2014) (Figure 9). The result corresponds with the age of the Nanggulan Formation suggested by Purnamaningsih & Pringgoprawiro (1981), Lunt & Sugiatno (2003), and Marliyani (2005). There are three calcareous nannofossil zones identified from the Watupuru Route, namely as follows:

Figure 10. Biostratigraphic correlation of the Jetis, Balak, and Watupuru Routes.

a. *Chiasmolithus solitus* Partial Range Zone

This zone is marked by *Chiasmolithus solitus*'s last occurrence at the top and an undefined bottom border. The zone is represented by samples KW1 to KW28 and is equivalent to NP16 of the zonal division by Martini (1971), as indicated by the first occurrence of *Cribocentrum reticulata* in the lower part.

b. *Chiasmolithus solitus* - *Sphenolithus spiniger* Range Zone

This zone discloses the last occurrence of *Chiasmolithus solitus* as the bottom border and the last occurrence of *Sphenolithus spiniger* as the top one. The zone is determined from samples KW29 to KW48, in which the first occurrences of *Dictyococcites bisectus* and *Sphenolithus obtusus* are observed, equivalent to NP17 according to Martini (1971).

c. *Sphenolithus spiniger* Partial Range Zone

This zone reveals the last occurrence of *Sphenolithus spiniger*, setting a border at the bottom. However, the top border is unclear. The zone is defined by samples KW49 to KW64 and is equivalent to NP18, consistent with Martini (1971).

Based on results from the Jetis and Balak Routes, there are three calcareous nannofossil zones that can be distinguished as follow (figure 10):

a. *Chiasmolithus solitus* Partial Range Zone

The zone is marked by *Chiasmolithus solitus*'s last occurrence at the top border with an undefined bottom one. This zone is represented by samples JT1 to JT14 and equivalent to NP16 by Martini (1971), supported by the first occurrence of *Cribocentrum reticulata* in the lower part of this zone, similar to the Watupuru Route.

b. *Chiasmolithus solitus* - *Reticulofenestra umbilica* Range Zone

The zone is identified by the last occurrence of *Chiasmolithus solitus* at the bottom border of the Jetis Route and the last occurrence of *Reticulofenestra umbilica* at the top border of the Balak Route. The first occurrences of *Dictyococcites bisectus* and *Sphenolithus obtusus* are also found within the zone. This zone is equivalent to NP17-NP22 according to Martini (1971); however, no outcrop reveals in the middle part, showing a data gap like in the upper part of the Jetis Route. This zone is represented by samples JT15 to JT25 and BL1 to BL7.

c. *Reticulofenestra umbilica* Partial Range Zone

The zone is typified by the last occurrence of *Reticulofenestra umbilica* at the bottom border with an undefined top border. This zone is represented by samples BL8 to BL14 and is equivalent to NP23 as described by Martini (1971).

Lithological Changes and Sedimentation Rates

In accordance with the Watupuru and Jetis-Balak Routes, the overall grain size of the facies is decreased in the northward direction, i.e., from dominated sandstone in the Jetis Route to dominated siltstone in the Watupuru Routes. Along with the decreasing grain size, the total thickness of the succession is also increased northerly, indicating the source of sediment supply possibly comes from the direction of the Jetis Route. In consideration of the lithofacies of its depositional environment, the Watupuru Routes is interpreted as an offshore transitional deposition while the Jetis Route is interpreted as a shoreface area. This depositional environmental change suggests that water depth also increases northward in the direction of Watupuru Routes.

a. Sequence before 41.1 Ma

The distribution of lithofacies in the Watupuru Routes was coal, massive siltstones, laminated sandstones, and hummocky cross-stratified sandstones. The variation suggests an increase in water depth from the backshore area into the offshore transition-area. The sandstone and siltstone contained bioclasts of mollusks and foraminifera, while the lithofacies in the Jetis Route are mostly dominated by lamination of sandstone and siltstone.

b. Sequence 41.1 Ma to 40.40 Ma

Between 41.1 Ma and 40.40 Ma, the Watupuru Route has a sedimentation rate of 4.6 cm/kyr and is characterized by the fining-upward pattern. The distribution of siltstone facies is gradually increasing upward and becoming dominant, with occasional layers of fine to very fine-grained sandstone intercalations. In the Jetis Route, the fine to very fine-grained sandstones decrease in quantity, while the massive siltstones increase, alternating with fine to very fine-grained sandstone. The sedimentation rate is 5.6 cm/kyr. The sandstone and siltstone facies also contain bioclasts, consisting of mollusks and foraminifera. The foraminifera sandstones also appear in this section for the first time, possibly as a result of storm events. The overall fining-upward pattern suggests a stable increase in water depth. The low sedimentation rate possibly indicates a low sediment supply along with the extension tectonic period in the Nanggulan region (Prasetyadi, 2008) that contributed to an increase in accommodation.

c. Sequence 40.40 Ma to 40.34 Ma

This period is characterized by a second occurrence of foraminifera sandstones in the Jetis Route with a sedimentation rate of 31 cm/kyr; whereas in the Watupuru Route, massive siltstones are dominant with a sedimentation rate of 3.3 cm/kyr. The coarsening-upward pattern is observed in the Jetis Route, suggesting a decrease in water depth in the upper part of this sequence. Considering the increase in the sedimentation rate as the water depth decreased, the weathering and erosion of exposed outcrops might also intensify, resulting in more

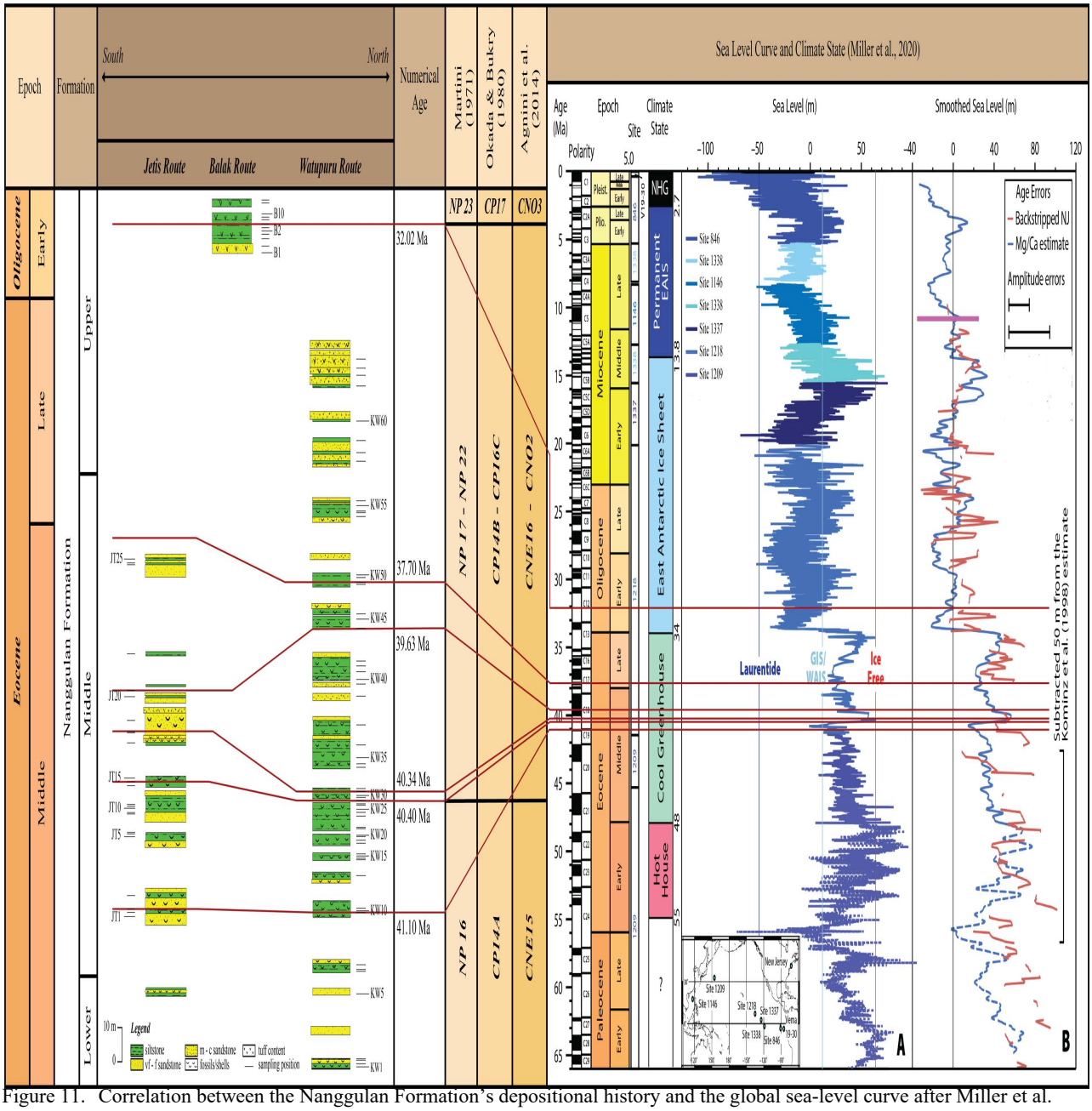

Figure 11. Correlation between the Nanggulan Formation's depositional history and the global sea-level curve after Miller et al. (2020)

sediment supply to deposit, particularly in the Jetis Route. Meanwhile, the increase in sediment supply in the Watupuru Route did not seem to affect the deeper environment.

d. Sequence 40.34 Ma to 39.63 Ma

This period was characterized by an increase in sandstone facies upward in the Watupuru Route with a sedimentation rate of 5.3 cm/kyr. The sandstone facies appear in between the massive siltstone facies that gradually increase upward. Meanwhile, the sedimentation rate of the Jetis Route is 1.2 cm/kyr. The fine to very fine-grained sandstone facies appear dominantly in the base of this sequence, and then abruptly change into a coarse to medium-grained sandstone. The overall pattern in each route is coarsening upward, suggesting a decrease in water depth. There is a significant decrease in sedimentation rate in the Jetis Route, whereas the sedimentation rate of Watupuru Route increases compared to the previous period. This change possibly indicates that the sediment accommodation of the Jetis Route is significantly decreasing, and the deposition of the sediment is directed to the deeper environment, causing the sedimentation rate of the Watupuru Route to increase.

e. Sequence 39.63 Ma to 37.32 Ma

Within this period, the sedimentation rate in the Watupuru Route is 0.9 cm/kyr. The sandstone facies found

in this route also appear increasingly, along with decreasing bioclast content. In overall, grain size becomes coarsening-upward, i.e., from fine to very fine-grained sandstones to coarse to medium-grained sandstones. The third appearance of foraminifera sandstone facies in this sequence indicates a considerable shallower environment in the Watupuru Route. Meanwhile, the appearance of the sandstone facies in the Jetis Route becomes frequent toward the upper part.

f. Sequence after 37.32 Ma

After 37.32 Ma, the appearance of sandstone facies in the Watupuru Route become more frequent. The fine to very fine-grained sandstone facies appeared frequently upward, alternating with coarse to medium-grained sandstone. In the Jetis Route, there are no lithofacies documented after 37.32 Ma. The uneven distribution after 37.32 Ma suggests a significant change in depositional environment. The lithofacies association in the Watupuru Route indicates a shallower environment from upper to lower shoreface, revealing a coarsening-upward pattern toward the end of this sequence.

g. Sequence around 32.03 Ma

In the Jetis Route, this period is characterized by a deposition of marlstone, which indicated an offshore environment. This sequence is entirely separated from the lower sequence due to no outcrop recorded here. There is a

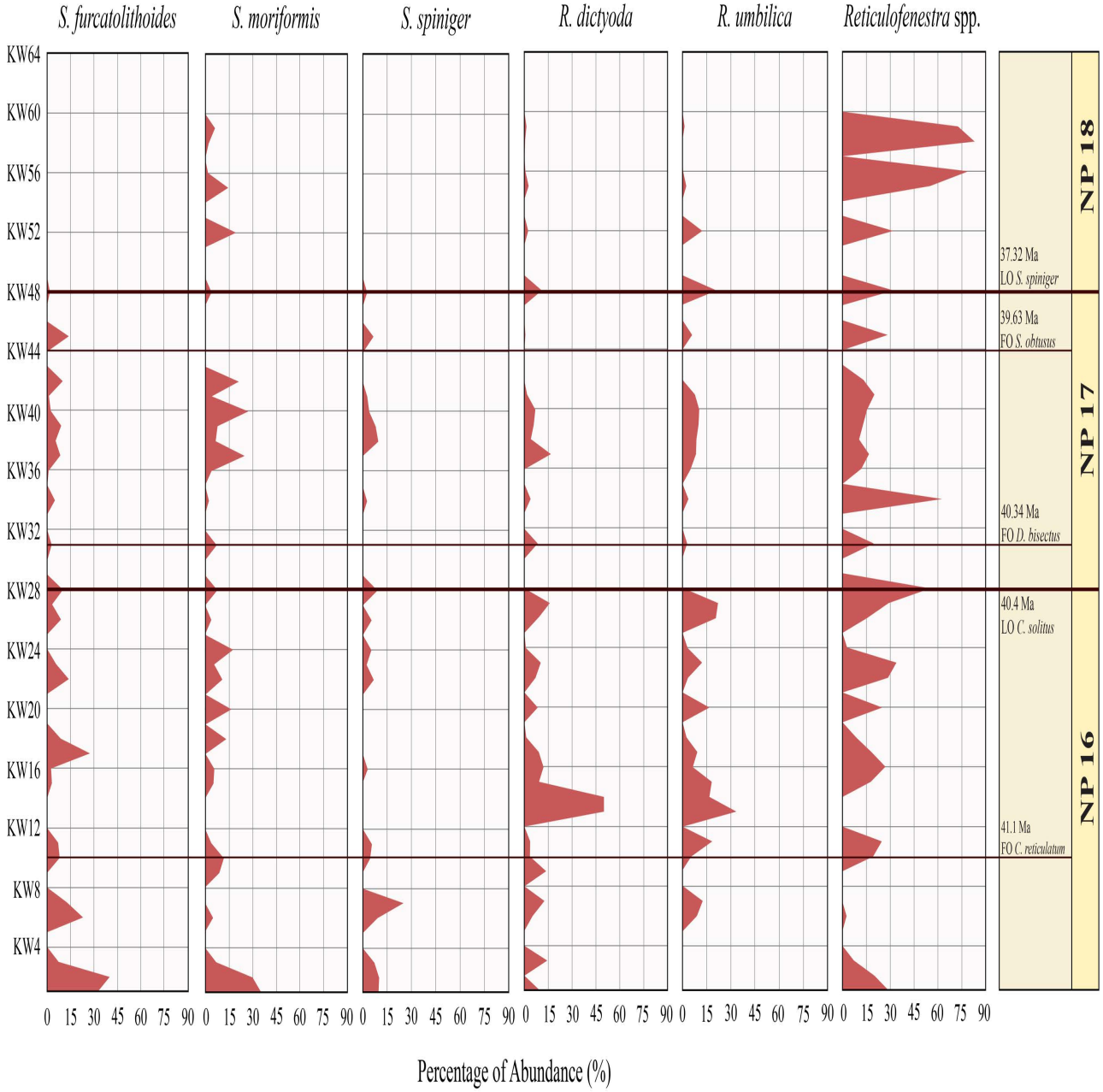

Figure 12. The abundance percentage in *S. furcatolithoides, S. moriformis, S. spiniger, R. dictyoda, R. umbilica,* and *Reticulofenestra* spp. in the Watupuru Route.

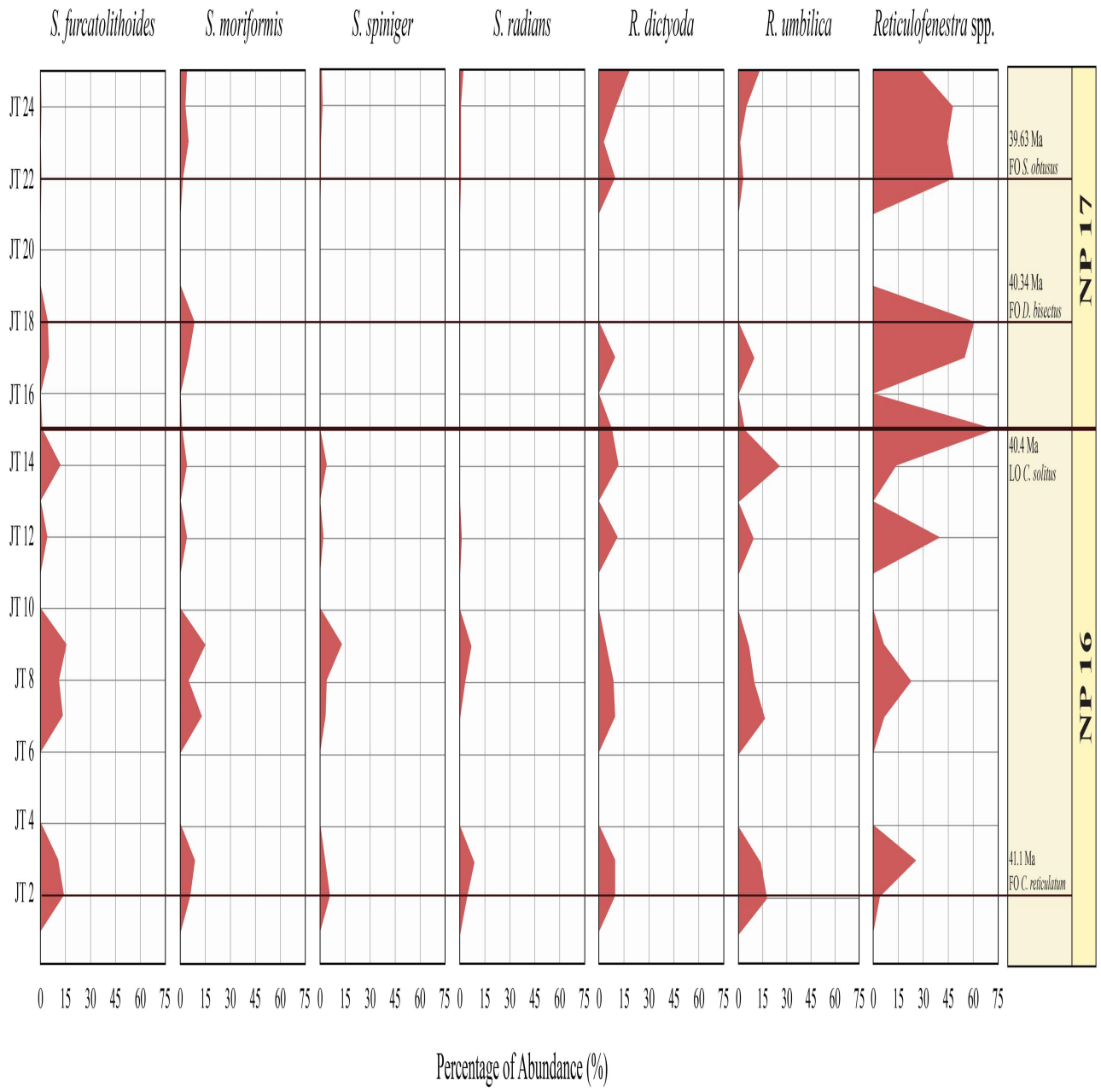

Figure 13. The abundance percentage of *S. furcatolithoides, S. moriformis, S. spiniger*, *R. dictyoda, R. umbilica,* and *Reticulofenestra* spp. in the Jetis Route.

5.29 Ma time gap between the sequence of the Watupuru Route and the sequence in the Jetis Routes. From the period of 39.63 Ma to 32.03 Ma, the sedimentation rate is 1.3 cm/kyr in Jetis Route. The marl shows a slight reduction in grain size from fine to very fine sand to silt-clay size, suggesting an increase in water depth. There is no bioclast content found in this sequence.

The changes in the depositional environment within the study area are interpreted as a result of sea-level fluctuations, suggesting that the deposition of the Nanggulan Formation has been greatly affected by the sea level changes. To confirm this interpretation, the correlation between the Nanggulan Formation's depositional history and the relative sea-level curve was made by utilizing the global sea level curve proposed by Miller et al. (2020) (Figure 11).

From the correlation, it is confirmed that there were significant fluctuations in sea level during the deposition of the Nanggulan Formation. The global sea-level curve showed two cycles of sea-level rise and fall happening during the depositional period, which closely influenced the changes of depositional environment within the study area. Before 41.1 Ma, global sea level rose until 40.7 Ma period before slightly falling toward 40.4 Ma. As a result, the lithofacies show a fining-upward pattern below 40.4 Ma. During the period of 40.4 Ma to 40.34 Ma, global sea level fell slightly, indicated by a coarsening-upward pattern in the Jetis Route and the decrease of siltstone

facies in the Watupuru Route. From 40.34 Ma to 39.8 Ma, sea level was relatively stable but then slightly rose from 39.8 Ma to 39.63 Ma. In the Watupuru Route, the sandstone facies slightly increased but were still dominated by siltstone. In the Jetis Route, the fine to very fine-grained sandstone facies were deposited consistently and then the intercalation of siltstone appeared before 39.63 Ma, confirming the rise of sea level at the upper part of the section.

Within the period of 39.63 Ma to 37.32 Ma, global sea level slowly decreased until 38.7 Ma and then rose slightly to 37.32 Ma. The lithofacies show a coarsening upward pattern, confirming sea level change. In the Watupuru route, the siltstone facies occur alternately with sandstone facies. Meanwhile, there is a slight increase of siltstone intercalations alternated with sandstone facies in the Jetis Route toward the upper part. After 37.32 Ma, global sea level continued to rise. However, the change in lithofacies does not reflect the sea level change. In the Watupuru route, the lithofacies after 37.32 Ma appeared to be dominated by sandstone facies with a coarsening-upward pattern. The distribution of lithofacies and the rising of sea level lead to the interpretation that the sedimentation rate possibly outpaced the rate of sea level rise. In a short period around 32.02 Ma, sea level rose slightly. The fining-upward pattern in the Balak Site possibly related to this sea level change. However, the lack of outcrop distribution inclines this part to be separated completely from the rest of the deposition in the Jetis and Watupuru Routes, although the interpretation might not possibly be accurate.

Indication of environmental changes from nannofossil data

In the Watupuru Route, from 41.1 Ma to 40.40 Ma, there was a slightly increase of percentage abundance from *Reticulofenestra* taxa (Figure 12), especially small *Reticulofenestra* (*Reticulofenestra* spp.). Meanwhile, *Sphenolithus* thrived before 41.1 Ma and their abundance gradually decreased until 40.40 Ma, suggesting a shift from oligotrophic to eutrophic condition at age 41.1 Ma - 40.40 Ma. *Sphenolithus* is taxa that prefers oligotrophic and warm-water condition (Aubry, 1998; Bralower, 2022; Gibbs et al. 2004; Villa et al. 2008; Toffanin et al. 2011; Imai et al. 2015), while small *Reticulofenestra* is considered to be an indicator of eutrophic environment (Takahashi & Okada, 2000; Kameo, 2002; Balleeger et al. 2012; Imai et al. 2015; Hendrizan, 2016) because small placoliths typically flourish in high-productivity areas (Okada and Honjo, 1973; Winter et al. 1994; Okada, 2000; Hagino and Okada, 2000; Toffanin et al. 2011). Small *Reticulofenestra* (*Reticulofenestra* spp.) continued to thrive, especially in Zone NP18. However, *R. dictyoda* and *R. umbilica* decreased after 40.4 Ma. *Sphenolithus* slightly increased in the middle of Zone NP17 before decreasing again after 37.32 Ma.

In the Jetis Route, the percentage abundance of *Reticulofenestra* taxa did not change significantly from 41.1 Ma to 40.40 Ma. However, small *Reticulofenestra* (*Reticulofenestra* spp.) drastically increased in 40.40 Ma and continued to thrive from then on (Figure 13). On the other hand, *Sphenolithus* taxa started thriving from 41.1 Ma. Their abundance decreased slightly before 40.40 Ma and drastically decreased after 40.40 Ma. During and after 40.40 Ma, the low abundance of *Sphenolithus* taxa and the increase of eutrophic taxa, such as *Reticulofenestra,* may be driven by enhanced eutrophy since the sphenoliths prefer oligotrophic and warm-water conditions. The calcareous nannofossil change after 39.63 Ma in the Jetis-Balak Routes cannot be interpreted due to lack of outcrop data.

We suspect that the enhanced eutrophy in the Jetis and Watupuru Routes was caused by the increasing terrigenous input in and after 40.40 Ma, thus providing nutrient availability on the water surface. This interpretation is supported by the abrupt increase in sedimentation rates in the Jetis Route before and after 40.40 Ma, which is from 5.6 cm/kyr to 31 cm/kyr. However, the sedimentation rate in the Watupuru Route is slightly decreased in that age, from 4.6 cm/kyr to 3.3 cm/kyr. It is also confirmed from sea level change that the increase in sedimentation rates was likely influenced by sea level fall in the age of 40.40 Ma to 40.34 Ma.

CONCLUSIONS

Based on the biodatum identified in the study area, the biostratigraphy of the Nanggulan Formation is divided into five zonations following the standard zonation by Martini (1971). There are four partial zones and one complete one, stated as follows: the upper part of Zone NP16, Zone NP17, the lower part of Zone NP18, the upper part of Zone NP22, and the lower part of Zone NP23. Based on the biostratigraphy study, the Nanggulan Formation was deposited at the age of 41.1 Ma to 32.2 Ma (Middle Eocene to Early Oligocene).

According to the horizontal distribution of lithofacies, the depositional environment of the Nanggulan Formation became shallower southward in the Jetis Route and shifted to a deeper environment northward in the Watupuru Route. The deposition of the Nanggulan Formation is strongly believed to be greatly influenced by the fluctuation of global sea level according to sea level change correlation.

The decrease of oligotrophic taxa (*Sphenolithus*) and the increase of eutrophic taxa (*Reticulofenestra*), especially small reticulofenestrids (*Reticulofenestra* spp.), suggest that there was a shift of the environment condition from oligotrophic in around 41.1 Ma to eutrophic condition after 40.40 Ma, particularly. The enhanced eutrophy in Jetis and Watupuru Route is believed as a result of increasing terrigenous input in and after 40.40 Ma, thus providing nutrient availability in the water surface. This interpretation is supported by the increase in

the sedimentation rate when sea level slightly decreased at 40.40 Ma.

REFERENCES

Agnini, C., Fornaciari, E., Raffi, I., Catanzariti, R., Palike, H., Backman, J., and Rio., D. (in press), 2014. Biozonation and biochronology of Paleogene calcareous nannofossils from low and middle latitudes. *Newsletter on Stratigraphy*, 47(2):131-181.

Aubry, M.-P., 1998. *Early Paleogene calcareous nannoplankton evolution: A tale of climatic amelioration*. In: Aubry, M.-P., Lucas, S., Berggren, W. (Eds.), *Late Paleocene–Early Eocene Climatic and Biotic Events in the Marine and Terrestrial Record*. Columbia University Press: 158–203.

Ballegeer, A. M., Flores, J. A., Sierro, F. J., and Andersen, N., 2012. Monitoring fluctuations of the subtropical front in the Tasman Sea between 3.45 and 2.45 Ma (ODP site 1172). *Palaeogeography, Palaeoclimatology, Palaeoecology*, 313-314(1): 215-224.

Bralower, T.J., 2002. Evidence for surface water oligotrophy during the Paleocene–Eocene Thermal Maximum: nannofossil assemblage data from Ocean Drilling Program Site 690, Maud Rise, Weddell Sea. *Paleoceanography*, 17(2): 1023p. doi:10.1029/2001PA000662.

Bown, P.R. and Young, J.R., 1998. Techniques. In: Bown, P.R., Ed., *Calcareous Nannofossil Biostratigraphy (British Micropalaeontological Society Publications Series)*, Chapman and Kluwer Academic, London, 16-28.

Bown, P.R., 1998. *Calcareous Nannofossil Biostratigraphy.* 1st Edition. New York: Springer Science Business Media, LLC.

Farinacci, A., 1969. *Catalogue of Calcareous Nannofossil*. Roma: Instituto di Geologia e Paleontologia Università di Roma.

Fioroni, C., Villa, G., Persico, D., and Jovane, L., 2015. Middle Eocene-Lower Oligocene calcareous nannofossil biostratigraphy and paleoceanographic implications from Site 711 (equatorial Indian Ocean), *Marine Micropaleontology*, 118: 50–62.

Fornaciari, E., Agnini, C., Catanzariti, R., Rio, D., Bolla, E. M., Valvasoni, E., 2010. Mid-Latitude calcareous nannofossil biostratigraphy and biochronology across the middle to late Eocene transition. *Stratigraphy*, 7(4): 229-264, text-figures 1-16, tables 1-3, plates 1-2.

Gibbs, S.J., Shackleton, N.J., Young, J.R., 2004. Orbitally forced climate signals in mid-Pliocene nannofossil assemblages. *Marine Micropaleontology*, 51: 39–56. doi:10.1016/ j.marmicro.2003.09.002.

Hagino, K., Okada, H., and Matsuoka, H., 2000. Spatial dynamics of coccolithophore assemblages in the equatorial Western-Central Pacific Ocean. *Marine Micropaleontology*, 39: 53-72.

Hendrizan, M., 2016. Nutrient level change based on calcareous nannofossil assemblages during Late Miocene in Banyumas Subbasin. *Indonesian Journal on Geoscience*, 3(3): 185-196. DOI: 10.17014/ijog.3.3.185-196.

Imai, R., Farida, M., Sato, T., Iryu, Y., 2015. Evidence for eutrophication in the north western Pacific and eastern Indian oceans during the Miocene to Pleistocene based on the nannofossil accumulation rate, Discoaster abundance, and coccolith size distribution of Reticulofenestra. *Marine Micropaleontology*, 116: 15-27.

Kameo, K., 2002. Late Pliocene Caribbean surface water dynamics and climatic changes based on calcareous nannofossil records. *Palaeogeography, Palaeoclimatology, Palaeoecology*, 179: 211-226.

Lelono, E. B., 2000. *Palynological Study of the Eocene Nanggulan Formation, Central Java, Indonesia*. Unpublished PhD Thesis. University of London.

Lunt, P., Sugiatno, H., 2003. *A review of the Eocene and Oligocene in the Nanggulan Area, South Central Java*. Lundin Banyumas b.y., exploration report of field study in Nanggulan area (unpublished).

Marliyani, G., 2005. *Penentuan Umur dan Paleobatimetri Formasi Nanggulan Bagian Atas Berdasarkan Foraminifera Planktonik dan Bentonik Jalur Balak, Kecamatan Nanggulan, Kulon Progo, DIY*. Universitas Gajah Mada, Yogyakarta.

Martini, E., 1971. Standard Tertiary and Quaternary Calcareous Nannoplankton Biozonation, in: Haq, B.U. (Eds.), *Nannofossil Biostratigraphy*, Hutchinson Ross Publishing Company, Pennsylvania: 264-307.

Miller, K.G., J.V. Browning, W.J. Schmelz, R.E. Kopp, G.S. Mountain, and J.D. Wright, 2020. Cenozoic sea-level and cryospheric evolution from deep-sea geochemical and continental margin records. *Science Advance Geochemistry*, 6(20): 15p.

Okada, H., 1981. Calcareous Nannofossils of Cenozoic formations in Central Java, *in: Saito (Ed.). Micropaleontology, petrography and lithostratigraphy of Cenozoic rocks of the Yogyakarta region, Central Java*. Dept. of Earth Science, Yamagata University.

Okada, H., 2000. Neogene and Quaternary calcareous nannofossils from the Blake Ridge, Sites 994, 995, and 997. In: Paull, C.K., Matsumoto, R., Wallace, P.J., Dillon, W.P. (Eds.), *Proc. ODP, Ocean*

Drilling Program, College Station, TX. Sci. Results, 164: 331–341.

Okada, H., Honjo, S., 1973. *The distribution of oceanic coccolithophorids in the Pacific. Deep Sea Research*, 20: 355–374.

Okada, H. and Bukry, D. 1980. Supplementary Modification and Introduction of Code Numbers to the Low-Latitude Coccolith Biostratigraphic Zonation (Bukry, 1973; 1975), *Marine Micropaleontology,* 5: 321 – 325.

Prasetyadi, C., 2008. Provenan Batupasir Eosen Jawa Bagian Timur. *Proceeding Pertemuan Ilmiah Tahunan IAGI ke-37, pp. 80-97* In: Sasongko, W., Mahendra, F. H. M., Buha, F., Legi, M. R., 2016. Kajian Tatanan Tektonik, Asal Batuan dan Iklim Purba pada Batupasir Formasi Nanggulan berdasarkan Analisis Petrografi. *Proceeding Seminar Nasional Kebumian ke-9 6-7 Oktober 2016; Graha Sabha Pramana.*

Perch-Nielsen, K. 1985. *Cenozoic Calcareous Nannofossils*. In: Bolli, H.M, et al., Eds., *Plankton Stratigraphy*. Cambridge University Press, Cambridge: 427-554.

Purnamaningsih, S. dan Pringgoprawiro, H., 1981. Stratigraphy and Planktonic Foraminifera of the Eocene - Oligocene Nanggulan Formation, Central Java. *Palaeontology Series* 1: 9 - 28.

Rahardjo, W., Sukandarrumidi, and Rosidi, H.M.D., 1977. *Geological map of the Jogjakarta Sheet, Java*. Geological Research and Development Centre, Bandung.

Rahardjo, W., Sukandarrumidi, Rosidi, H.M.D., 1995. *Geological Map of the Yogyakarta Sheet, Java*. Geological Research and Development Center, 2nd Edition, Bandung.

Savian, J.F., Jovane, L., Bohaty, S.M., Wilson, P.A., 2013. Middle Eocene to Early Oligocene magnetostratigraphy of ODP Hole 711A (Leg 115), western equatorial Indian Ocean. *Geology Society London Special Publication*, 373p.

Saputra R. and Akmaluddin., 2015. Biostratigrafi Nannofosil Gampingan Formasi Nanggulan Bagian Bawah berdasarkan Batuan inti dari Kec. Girimulyo dan Kec. Nanggulan, Kab. Kulon Progo, DI Yogyakarta. *Proceeding Seminar Nasional Kebumian ke-8.*

Satyana, A.H., 2005. Oligo-Miocene Carbonates of Java, Indonesia: Tectonic-Volcanic Setting and Petroleum Implication. *Proc. IPA 30th Annual Convention and Exhibition*.

Smyth, H.R., Hall, R. and Nichols, G.J., 2008. Cenozoic volcanic arc history of East Java, Indonesia: the stratigraphic record of eruptions on an active continental margin. *Special Papers-Geological Society of America*, 436: 199.

Takahashi, K. and Okada, H., 2000. The Paleoceanography for the Last 30,000 Years in the Southeastern Indian Ocean by Means of Calcareous Nannofossils. *Marine Micropaleontology*, 40: 83-103. http://dx.doi.org/10.1016/S0377-8398(00)00033-5 .

Toffanin, F., Agnini, C., Fornaciari, E., Rio, D., Giusberti, L., Luciani, V., Spofforth, D.J.A., Pälike, H., 2011. Changes in calcareous nannofossil assemblages during the Middle Eocene Climatic Optimum: Clues from the Central–Western Tethys (Alano section, NE Italy). *Marine Micropaleontology*, 81: 22–31.

Van Bemmelen, R.W., 1949. *The Geology of Indonesia*. Vol. IA, General Geology of Indonesia and Adjacent Archipelagos, Martinus Nijhoff, The Hague, Government Printing Office, Amsterdam.

Villa, G., Fioroni, C., Pea, L., Bohaty, S. M. and Persico, D., 2008. Middle Eocene– Late Oligocene climate variability: Calcareous nannofossil response at Kerguelen Plateau, Site 748. *Marine Micropaleontology*, 69: 173–192.

Widagdo, A., Pramumijoyo, S., Harijoko, A., 2016. Kajian Pendahuluan Kontrol Struktur Geologi Terhadap Sebaran Batuan-Batuan Di Daerah Pegunungan Kulonprogo Yogyakarta. *Proceeding Seminar Nasional Kebumian ke-9*.

Winter, A., Jordan, R.W., Roth, P.H., 1994. Biogeography of living coccolithophores in ocean waters. In: *Coccolithophores* (eds. A. Winter and W.G Siesser). Cambridge Univ. Press: 161-177.

MARINE GEOMAGNETIC ANOMALY BELT AND ITS RELATIONSHIP TO THE REMNANT ARCS IN THE NORTHWESTERN JAVA SEA, INDONESIA

SABUK ANOMALI GEOMAGNETIK KELAUTAN DAN HUBUNGANNYA DENGAN JEJAK BUSUR DI LAUT JAWA BAGIAN BARAT LAUT, INDONESIA

Dida Kusnida[1*] and Lukman Arifin[2]

[1] National Research and Innovation Agency, Jl. Sangkuriang, Dago, Bandung-40135, Indonesia
ORCID https://orcid.org/0000-0001-9766-8143

[2] National Research and Innovation Agency, Jl. Sangkuriang, Dago, Bandung-40135, Indonesia
ORCID https://orcid.org/0000-0002-2493-0785

*Corresponding author: dida0003@brin.go.id

(Received 08 August 2022; in revised from 13 August 2022; accepted 09 September 2022)

DOI : 10.32693/bomg.37.1.2022.773

ABSTRACT : The continuous marine geomagnetic survey within a time interval of 1-second sampling and a precision of 0.1 nT was conducted in the northwestern Java Sea to identify and interpret the general trend of total marine magnetic anomalies and the possibility related to the geological resource potential. These magnetic data were then processed according to the formula corrected and applied to marine magnetic data. The total marine magnetic anomalies of the northwestern Java Sea indicate a well-defined lateral trend belt of anomaly contours. Anomalies are divided into four delineation zones: Zones I, II, III, and IV. A preliminary analysis of these anomalies led to the interpretation, reflecting the residual of a slightly east-west trending geological body underneath. Examination of magnetic anomalies suggests Zone I and IV characterize a basinal area, Zone II depicts a granitic belt, and Zone III describes a Cretaceous magmatic arc system in the east that extends from Middle Java across the Java Sea through Southern Kalimantan. These magnetic anomalies seem to coincide with the free air gravity anomalies data derived from TOPEX satellite data.

Keywords: the northwestern Java Sea, total magnetic anomaly, remnant arc, granite

ABSTRAK*: Survei magnetik kelautan berkesinambungan dengan interval waktu pengambilan sampel 1 detik dan ketelitian 0,1 nT dilaksanakan di baratlaut Laut Jawa untuk mengidentifikasi dan menafsirkan kecenderungan arah anomali magnetik total dan kemungkinan kaitannya dengan potensi sumber daya geologi. Data magnetik ini kemudian diproses sesuai dengan rumus dan koreksi yang umum diterapkan terhadap data magnetik kelautan. Sabuk anomali magnetik total baratlaut Laut Jawa menunjukkan kecenderungan arah lateral yang cukup jelas. Pola anomali magnetik ini dapat dibagi menjadi empat zona: Zona I, II, III, dan IV. Dugaan awal terhadap anomali ini mencerminkan adanya jejak tubuh geologi di bawahnya berarah agak timur-barat. Pengamatan anomali magnetik menunjukkan bahwa Zona I dan IV mencirikan daerah cekungan, Zona II menggambarkan sabuk granit, dan Zona III kemungkinan menggambarkan sistem busur magmatik berumur Kapur yang membentang dari Jawa Tengah melintasi Laut Jawa melalui Kalimantan Selatan. Anomali magnetik dari area studi ini tampak mirip dengan anomali udara bebas dari data satelit TOPEX.*

Kata Kunci: *: Laut Jawa bagian Baratlaut, anomali magnetik total, jejak busur, granit*

Contribution:

D.K. and L.A. conceived and planned the study and performed the marine geomagnetic data acquisition and processing. D.K. took the lead in writing the manuscript. All authors provided critical input, discussed the results, and completed the manuscript.

INTRODUCTION

From 1990 until 2020, systematic marine geomagnetic surveys and mapping in Indonesia were conducted by the Marine Geological Institute of Indonesia (MGI) using RV Geomarin I to cover 64 of 365 quadrangles. This paper discusses a result of ten marine geomagnetic quadrangles compiled by Kusnida et al. (2003), covering the South of Karimata Street and the northwestern Java Sea. Compilation of the total magnetic anomaly map results shows a unique distribution anomaly pattern, forming an arc with an east-west direction and curving to the northeast in the east. However, marine geomagnetic anomaly distribution in this area has never been studied in detail. Many geomagnetic studies confirmed that anomalous geomagnetic variations usually reflect the geological conditions and rock composition underneath (Connelly, 1979; Ferré et al., 1999; Aydin et al., 2007). In addition, many authors have used magnetic susceptibility measurements to delineate petrographic and geochemical variations of granitic plutons (Tarling and Hrouda, 1993, Ishihara et al., 2000, Kusnida et al., 2008).

This study aims to identify and interpret the general trend of total marine magnetic anomalies of the northwestern Java Sea and its surrounding. It is referred to as a remnant arc, such as depicted by the total magnetic anomaly of submerged Belitung Granite (Kusnida et al., 2008) and the marine free air gravity map of the study area (https://topex.ucsd.edu/marine_grav/mar_grav.html), as well as the possibility related to the geological resource potential. However, this paper is still preliminary because magnetic data is a dipole field that causes multiple interpretations of the subsurface geological objects, especially for areas with low magnetic latitudes. Further data processing can be conducted by reducing to poles (RTP) in the future to show a monopole magnetic anomaly.

Regional Settings

The Indonesian archipelago consists of seven orogenic collisions, namely Meratus, Sulawesi, Molucca Sea, Seram, Lengguru, Papua Central Mountains, and Timor Orogens (Satyana et al., 2007). Meratus Orogen in Southeast Kalimantan results from a collision between the continental shield of Schwaner (Southwest Kalimantan) and the continental fragment of Paternosfer. The Schwaner Mountains, the so-called part of Sundaland, is a complex of igneous and metamorphic rocks formed by magmatism due to various tectonic events. In this area, the formation of the A-type granitic rocks is related to the rifting of the Southwest Borneo Block from Northwest Australia during the Jurassic (Auliya et al., 2021).

Sundaland is a geological name to refer to areas in the Southeast Asia peninsula, including the Malacca peninsula, the island of Borneo, Sumatra, and Java. The tectonic evolution of Sundaland is a combination of fragments remnants from the Gondwana continent, which was separated due to the Late Jurassic to the Middle Miocene spreading (Hall et al., 2009; Metcalfe, 2011; Auliya et al., 2021). These parts then merged with part of the Eurasian continent, formed tectonic subduction in southern Eurasia, and changed its movement to what it is today (Figure 1). Tectonically, the study area is divided into the western and eastern parts. The east-west trending Bangka-Belitung controls the western to Schwaner Belt in West Kalimantan, which belongs to the magmatic arc system composed of acid to intermediate rocks. In contrast, the northeast-trending Meratus-Bobaris Complex in South Kalimantan controls the eastern part, consisting of the ophiolite. In the Java Sea, the Karimun Java Arc separates these ranges and the Meratus-Bobaris fault system, which correlated with the Lok-Ulo fault system in Middle Java (Sunarya and Simanjuntak, 1987).

The northern part of the Java Sea, where the study area is located, has an average water depth of 60 - 130 meters. It is a middle or transition zone that separates the South China Sea – the Strait of Karimata from the Banda Sea system. This transition zone is the gateway between West Indonesia and East Indonesia and physiographically covers offshore Bangka-Belitung-South Kalimantan.

DATA ACQUISITION AND METHOD

This study was derived from a geomagnetic survey of RV Geomarin in the northwestern Java Sea area (Figure 2). Magnetic intensity data were collected using the Geometric marine magnetometer. Following a standard operating procedure, before magnetic recording was executed, the parameters were set on a sonar-link acquisition software, such as magnetometer sensor offset to GPS (*Global Positioning System*), sensor cable length (*layback*), and data sampling interval. The marine Geometric G.813 proton magnetometer sensor was hauled 150 meters behind the vessel with the precision of 0.1 nT in each continuous marine magnetic survey within a time interval of 1-second sampling. Magnetic data were observed and recorded by using a Soltec 3314B-MF recorder. Diurnal variation was measured and recorded using a stationary Ground Geometric, G.866 and G.724 Magnetometer operated on land during the cruise. The diurnal and earth's field corrections (International Geomagnetic Reference Field 2005) have been applied to the observed magnetic data. The total magnetic anomaly map subsequently is free from extraneous magnetic effect and primarily indicates the impact of geological structures underneath. Positioning and navigation of the surveyed area using the Global Positioning System (GPS). The marking of time and a fixed point on the recorder were plotted using an Annotator device. The base maps used in marine geomagnetic surveys were 1:250,000 scale using Universal Transverse Mercator (UTM) and Datum WGS-84 at a 5-km traverse interval.

RESULTS AND DISCUSSION

The geomagnetic field intensity measured at the observation point results from various variables, while the geomagnetic survey aims to measure the magnetic

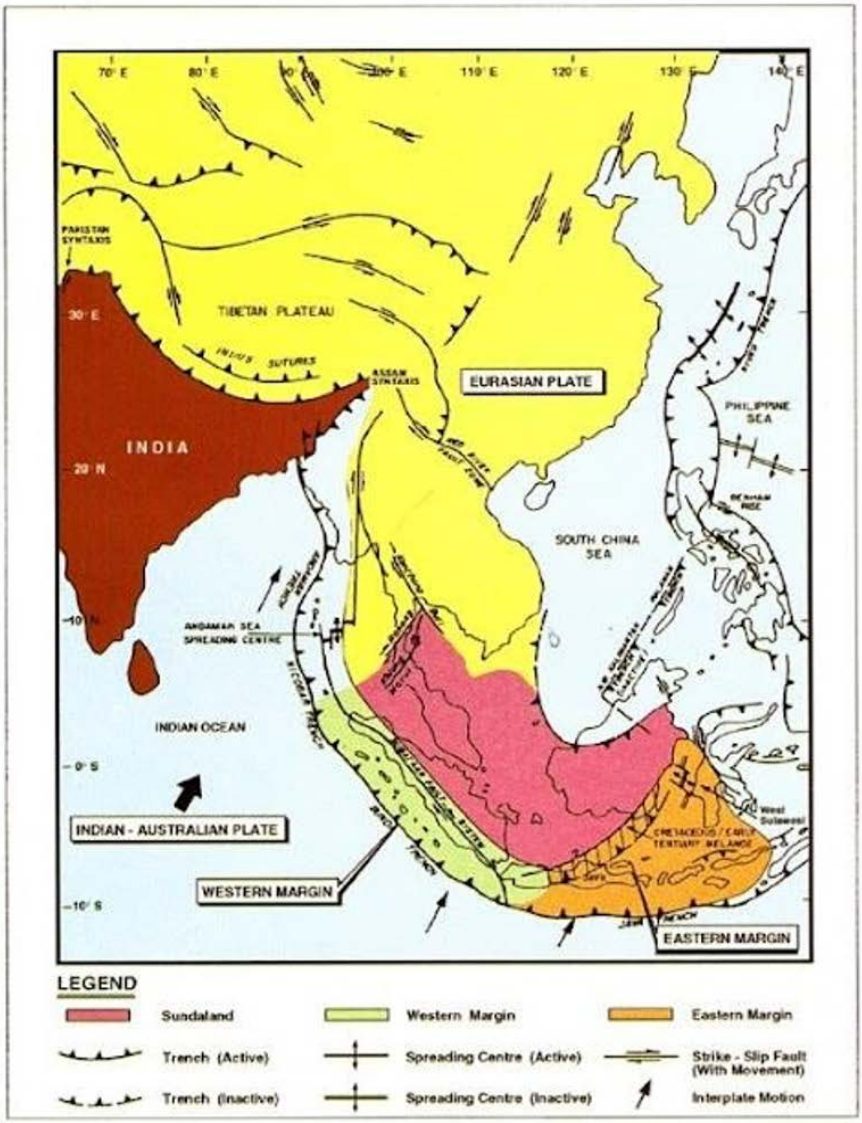

Figure 1. Location of Sundaland and its present developing tectonics (Modification from Davies 1984 in Sudarmono et al., 1997)

induction of the geological body, causing anomalies underneath. Therefore, it is necessary to reduce some variables that affect the measurement results. In a geomagnetic survey, the correction applied is primarily diurnal variations.

The value of the total magnetic anomaly contours in the study area varies between –500 to +400 nT, as described in Kusnida et al. (2003; 2008). The detailed interpretation was carried out from the anomaly values, resulting in the division of the study area into four zones (Figure 2): Zones I (- 50 nT to +400 nT), Zone II (< +50 nT), Zone III (closed by -200 nT), and Zone IV (-100 nT to -300 nT). A preliminary analysis of these anomalies led to the interpretation,which reflects the residual of a slightly east-west trending massive body underneath. Examination of magnetic anomalies suggests Zone I and IV characterize a basinal area, Zone II depicts a granitic belt, and Zone III describes a Cretaceous magmatic arc system in the east that extends from Middle Java across the Java Sea through Southern Kalimantan.

Zone I is characterized by a group of contour pair closures with values between -500 nT and +400 nT in an east-west direction. This pair of contour closures, in the southern part, is gradually adjacent to the homogeneous magnetic anomaly contour of Bangka-Belitung and characterizes the South China Sea and the Karimata Strait. Zone II is characterized by east-west arcuate far apart anomaly contours of <+50 nT representing the surrounding waters of the massive Bangka–Belitung islands. Zone III is characterized by many pairs of dense anomalous shapes trending west-east and then curving to the northeast to form a shield and is limited by a contour value of –200 nT on both sides. This contour pattern is a magnetic anomaly in the form of an arc approaching the island of Southwest Kalimantan. Finally, Zone IV is characterized by an

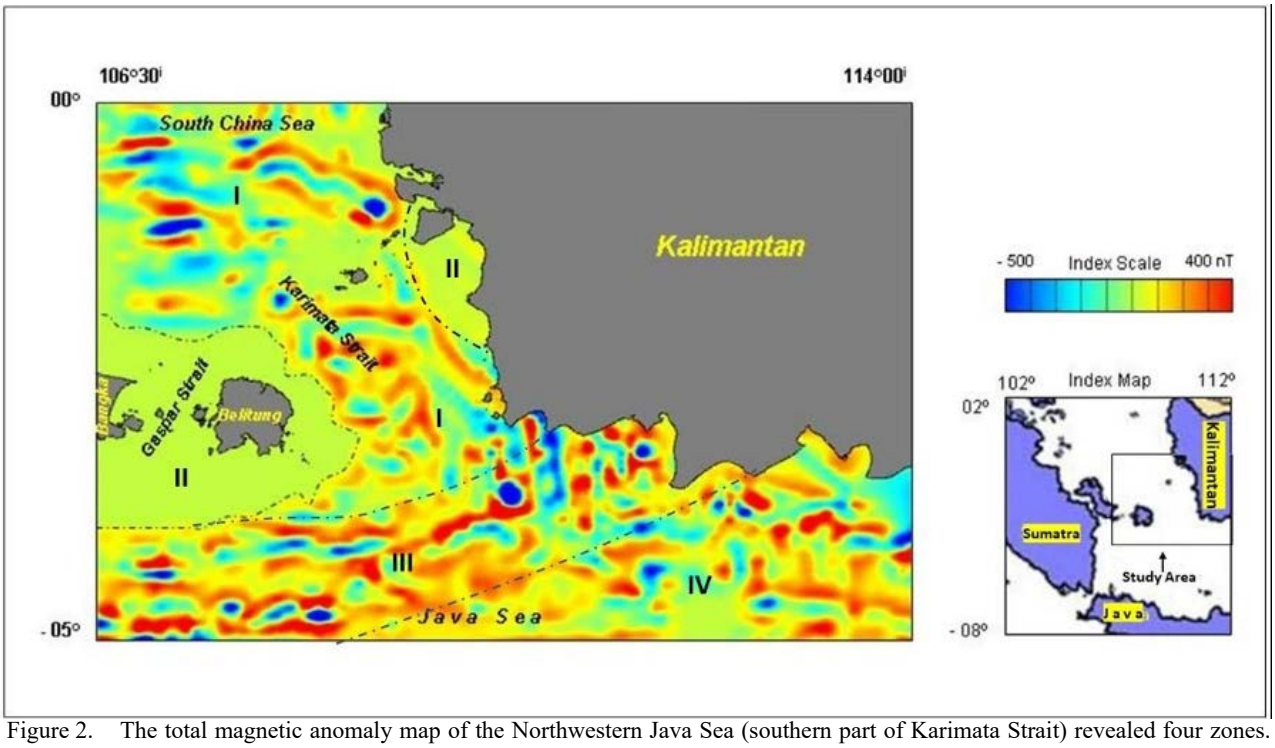

Figure 2. The total magnetic anomaly map of the Northwestern Java Sea (southern part of Karimata Strait) revealed four zones. The submerged Bangka-Belitung plutonic islands are classified as Zone II with magnetic anomaly < 50 nT. (Modified from Kusnida et al., 2008).

unorganized anomaly contours pattern of –100 to –300 nT. This anomaly pattern is believed to be the continuations of the melange-ophiolite complex in Lok Ulo in Middle Java and the Meratus Range of South Kalimantan. Therefore, it can be assumed that although the general trend of the four zones of the anomaly contours in the study area is slightly northeast, the occurrence of high and low closures in each zone indicates the control of the EW to NE structural lineation.

The distribution pattern of the total magnetic anomaly in the study area shows a massive homogeneous anomalous and predominate, expressing the submerged Bangka-Belitung plutonic, characterized by less than <+50 nT, which is also possibly related to the total magnetic anomaly that occurred in the West Kalimantan. Although each exposed intrusive body in Bangka-Belitung Islands has been known as granites, a distinction in the magnetic properties is shown by the variety of magnetic expressions. The susceptibility of submerged Bangka-Belitung is indicated by values ranging from 0.001– 0.003 cgs unit, as described by Kusnida et al. (2008).

The susceptibility values range from 0.001 - 0.05 cgs units confirmed to characterize granite in the eastern Lachlan Fold-Australia (Connelly, 1979). Petrographic study shows that granitic plutons in volcanic arcs are classified as calc-alkaline I-type granitoids with a susceptibility value of 0.001 - 0.03 cgs unit, such as Abukuma granites in Japan (Kamei and Takagi, 2003) and 0.03 – 0.06 cgs unit for Natuna granites (Ben Avraham, 1973). Based on its chemical criteria, granite is grouped into type I (igneous rock of origin), and type S is known to originate from partially melted sedimentary rocks. According to Aryanto et al. (2005), their study on Kelumpang-Belitung Island showed that the type of granite in the area is a biotite-granite type I and is associated with cassiterite minerals. Therefore, it is suspected that the magnetic anomalies of the submerged Bangka-Belitung pluton in West Kalimantan could be due to this type of granite.

Although the early tectonic history is poorly defined by magnetic dipole anomaly, the structural trend of basement rocks is well-exhibited by marine free-air gravity data (Figure 3). Free-air anomaly patterns in the east–northeast direction are expected to be geologically related to gently-cratonized Late Mesozoic (?) along ten to hundreds of kilometres. Compared with the magnetic dipole anomaly in the study area, the free-air gravity anomaly strengthens the dipole image's magnetic path. The positive free-air gravity anomaly with a value of >30 mGal is also distributed in the direction of E-W to NE-SW in pairs parallel to the free-air gravity anomaly with a value of <30 mGal. In general, the free-air anomaly contour pattern reflects the lineament of the rock mass distribution underneath with an almost uniform density, both in the form of height and low. A comparison of the free-air gravity anomaly distribution pattern with the magnetic dipole anomaly in the study area shows a unidirectional tendency in the form of the arcs.

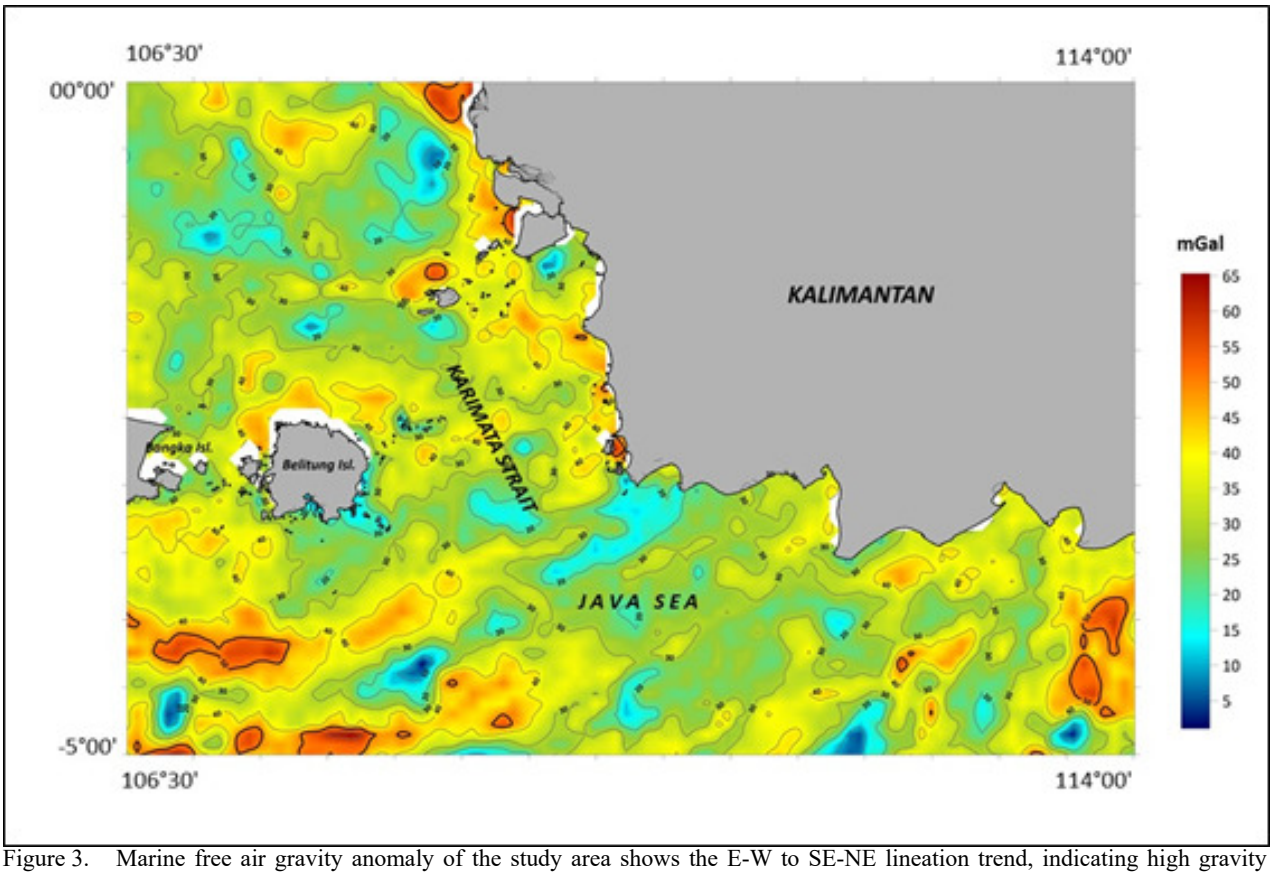

Figure 3. Marine free air gravity anomaly of the study area shows the E-W to SE-NE lineation trend, indicating high gravity anomaly lineation (>30 mGal) and low (<30 mGal) contour values (Source:https://topex.ucsd.edu/marine_grav/mar_grav.html).

CONCLUSIONS

The study area is characterized by magnetic anomaly values ranging from –500 nT to +400 nT. Regional negative values dominate the study area, except for the southwestern part near Sumatera Island; the anomaly tends to be positive. In general, the negative anomalies occupy the eastern and southern part of the study area and demonstrate only minor closures. The total marine geomagnetic anomalies of the northwestern Java Sea indicate a well-defined lateral trend belt of anomaly contours. They can be divided into four zones: zones I (- 50 nT to +400 nT), II (< +50 nT), III (closed by -200 nT), and IV (-100 nT to -300 nT). A preliminary evaluation of these anomalies led to the interpretation, reflecting the residual of a slightly east-west trending massive body underneath. Examination of magnetic anomalies suggests Zone I and IV characterize a basinal area, Zone II depicts a granitic belt, and Zone III describes a Cretaceous magmatic arc system in the east that extends from Middle Java across the Java Sea through Southern Kalimantan. A comparison of the free-air gravity anomaly distribution pattern with the magnetic dipole anomaly in the study area shows a coincides unidirectional anomaly contours tendency in the form of the arcs.

ACKNOWLEDGEMENTS

The authors would like to thank the Head of the Marine Geological Institute for allowing the writing of this paper. Thanks are also directed to the team members and technicians for cooperation during magnetic data acquisition and processing. Special thanks are directed to Sonny Mawardi and Ali Albab from the Marine Geological Institute for their help during the correction of this paper.

REFERENCES

Aryanto, N.C.D., Nasrun, Sianipar, A.H., and Sarmili, L., 2005. Granit Kelumpang sebagai granite tipe-I di Pantai Teluk Balok, Belitung. *Jurnal Geologi Kelautan*, 3(1): 19-27.

Auliya, I., Ramadhan, A., Darmaputra, M.K.M., Najah M.B., and Sucipta, I.G.B.E., 2021. Geochemical Characteristics of Schwaner Mountains Granitoids and their Relationship to Magmatism in the Southwest Borneo Block. *Proceedings of Joint Convention Bandung (JCB) 2021*: 775-778.

Aydin, A., Ferré, E.C. and Aslan, Z., 2007. The magnetic susceptibility of granitic rock as a proxy for geochemical composition: Example from the

Saruhan granitoids, NE Turkey. *Tectonophysics*, 441: 85-95.

Ben-Avraham, Z., 1973. *Structural framework of the Sunda shelf and vicinity.* PhD Thesis, Woods Hole Oceanographic Institute & MIT, 269 pp.

Connelly, J.B., 1979. Interpretation of subsurface shape of granites in the eastern Lachlan fold belt using aeromagnetic data. *Bulletin of the Australian Society of Exploration Geophysicists*, 10 (1): 92-95.

Ferré, E.C., Wilson, J. and Gleizes, G., 1999. Magnetic susceptibility and AMS of the Bushveld alkaline granites, South Africa. *Tectonophysics*, 307: 113-133.

<https://topex.ucsd.edu/marine_grav/mar_grav.html> [Accessed on August 29, 2022]

Hall, R., Clements, B., and Smyth, H.R., 2009. Sundaland: Basement character, structure and plate tectonic development. *Proceedings Indonesian Petroleum Associatio*n, 33rd Annual Convention: IPA09-G-134.

Ishihara, S., Hashimoto, M. and Machida, M., 2000. Magnetite/ilmenite series classification and magnetic susceptibility of the Mesozoic-Cenozoic plutons in Peru. *Resource Geology*, 50 (2): 123-129.

Kamei, A., & Takagi, T., 2003. Geology and petrography of the Abukuma granites in the Funehiki area, Fukushima Prefecture, NE Japan. The Journal of the Geological Society of Japan, 109(4): 234–251. doi:10.5575/geosoc.109.234

Kusnida, D., Azis, T. and Yuningsih, A., 2003. Total Magnetic Anomaly Map of Selat Karimata and Surroundings, Scale 1:1.000.000. *Marine Geological Institute of Indonesia.*

Kusnida, D., Astjario, P., and Nirwana, B., 2008. Magnetic Susceptibilities Distribution and Its Possibly Geological Significance of Submerged Belitung Granite. *Indonesian Mining Journal*, (11): 24 – 31.

Metcalfe, I., 2011. *Palaeozoic–Mesozoic history of SE Asia. Geological Society,* London, Special Publications, 355(1): 7–35. doi:10.1144/sp355.2

Satyana, A. H., Tarigan, R. L., Armandita, C., 2007. Collisional Orogens in Indonesia: Origin, Anatomy, and nature of Deformation. *Proceedings Joint Convention Bali,* The 32nd HAGI, The 36th IAGI, and the 29th IATMI Annual Conference and Exhibition.

Sudarmono, Suherman, T, and Eza, B., 1997. Paleogene basin development in Sundaland and its role to the petroleum systems in Western Indonesia. *Proc. Indon. Petrol. Assoc.,* International Conference on Petroleum Systems of SE Asia and Australasia, 545-560.

Sunarya, Y. and Simanjuntak, W. 1987. Mineral Prospects in Southern Kalimantan Offshore. *Proceedings of the 24th CCOP Session,* 33-39.

Tarling, D.H. and Hrouda, F., 1993. *The magnetic anisotropy of rocks*. Chapman & Hall, London, 217p.

PB RATIO ANALYSIS OF FORAMINIFERA TO OBSERVE PALEOCEANOGRAPHIC CHANGES DURING HOLOCENE IN ARAFURA SEA

ANALISIS PB RASIO FORAMINIFERA UNTUK MENGAMATI PERUBAHAN PALEOSEANOGRAFI SELAMA HOLOSEN DI LAUT ARAFURA

Swasty Aninda Piranti[1,2*], Luli Gustiantini[2], Shaska R. Zulivandama[2], Catur Purwanto[2], Lia Jurnaliah[3], Budi Muljana[3], Rina Zuraida[4], Sangmin Hyun[5]

[1] Study Program of Master, Faculty of Geological Engineering, Padjadjaran University, Jl. Raya Bandung Sumedang KM 21, Jatinangor – Indonesia, 45363

[2] Marine Geological Institute of Indonesia, Geological Agency – Ministry of Energy and Mineral Resources, Jl. Dr. Junjunan no. 236, Bandung, West Java - Indonesia, 40174

[3] Faculty of Geological Engineering, Padjadjaran University, Jl. Raya Bandung Sumedang KM 21, Jatinangor – Indonesia, 45363

[4] Research Center for Climate and Atmosphere, Research Organization for Earth Sciences and Maritime (ORKM), National Research and Innovation Agency (BRIN), Indonesia, Jl. Dr. Djundjunan No. 133, Bandung, West Java - Indonesia

[5] Marine Geology & Geophysics Division, Korea Institute of Ocean Science & Technology (KIOST), 385, Haeyang-ro, Yeongdo-gu, Busan Metropolitan City, 49111 KOREA

*Corresponding author: swasty20001@mail.unpad.ac.id

(Received 19 July 2022; in revised from 09 August 2022; accepted 24 October 2022)

DOI : 10.32693/bomg.37.1.2022.771

ABSTRACT: Arafura Sea is influenced by several climatic dynamics, it is also a part of the coral triangle that provides most of marine organism diversity of the world. Therefore, this area is an important waters that impact the climatic dynamic so its paleoceanographic changes need to be understood. For that, we analyzed the foraminiferal PB ratio from marine sediment core ARAFURA-24 with a core length of 179 cm, collected from 47.4 m water depth, combined with that of Aru-07, taken from 276 m water depth (core length 152 cm). Both sediment cores were collected from the Arafura Sea using a gravity corer on board Geomarin III. ARAFURA-24 was sub-sampling in every 20 cm interval, while Aru-07 had been prepared in every 10 cm interval. PB Ratio values from ARAFURA-24 and Aru-07 ranged from 0,56% - 7,43% and from 29,89% to 82,66%, respectively. The age model was reconstructed by ^{14}C radiocarbon dating derived from organic sediment, combined with tie points of PB ratio records. The result indicates that ARAFURA-24 has been sedimented since the last 9.7 kyr BP. PB ratio records reveal three maximum sea level rises, which are before 7.4 kyr BP, at 5.86 kyr, and after 3 kyr BP (approximately at 2 kyr BP at Aru-07). From the age model reconstruction, sedimentation during the last 3 kyr BP was relatively slower than that in the older period. It can be concluded that the foraminiferal PB ratio during Late Holocene was not significantly impacted by sedimentation rate (hence detrital influence), in contrast, during Mid-Holocene detrital influence had more impact on the PB ratio record.

Keywords: Arafura Sea; foraminifera; PB ratio analysis; paleoceanographic changes; Holocene

ABSTRAK: *Laut Arafura dipengaruhi oleh beberapa dinamika iklim, dan juga merupakan bagian dari segitiga terumbu karang yang menyediakan sebagian besar keanekaragaman organisme laut dunia. Oleh karena itu, daerah ini merupakan perairan penting yang mempengaruhi dinamika iklim sehingga perubahan paleoceanografinya perlu dipahami. Untuk itu, kami menganalisis PB rasio foraminifera dari inti sedimen laut ARAFURA-24 dengan panjang inti 179 cm, diambil dari kedalaman air 47,4 m, dikorelasikan dengan inti sedimen Aru-07, yang diambil dari kedalaman air 276 m (panjang inti 152 cm). Kedua inti sedimen diambil dari Laut Arafura dengan menggunakan penginti jatuh bebas dari kapal Geomarin III. ARAFURA-24 dicuplik setiap interval 20 cm, sedangkan Aru-07 dicuplik setiap interval 10 cm (telah dilakukan oleh peneliti terdahulu). Nilai PB Ratio dari ARAFURA-24 dan Aru-07 masing-masing berkisar antara 0,56% - 7,43% dan dari 29,89% hingga 82,66%. Model umur direkonstruksi dengan*

penanggalan radiokarbon ^{14}C yang diukur dari sedimen organik, dikorelasikan dengan titik ikat nilai PB rasio. Hasilnya menunjukkan bahwa ARAFURA-24 telah terendapkan sejak 9,7 kyr BP. perhitungan PB rasio mengungkapkan tiga kenaikan permukaan laut maksimum, yaitu sebelum 7,4 kyr BP, pada 5,86 kyr, dan setelah 3 kyr BP (sekitar 2 kyr BP di Aru-07). Dari rekonstruksi model umur, sedimentasi selama 3 kyr BP terakhir relatif lebih lambat dibandingkan dengan periode waktu yang lebih tua. Dapat disimpulkan bahwa PB rasio foraminifera pada masa Holosen Akhir tidak terlalu dipengaruhi oleh laju sedimentasi (karena pengaruh detrital), sebaliknya pada masa Mid-Holosen pengaruh detrital memberikan dampak lebih besar terhadap perhitungan PB rasio.
***Kata Kunci:** : Laut Arafura; foraminifera; analisis PB rasio; perubahan paleoseanografi; Holosen*

INTRODUCTION

Indonesian waters are known as a "mixed-master" that modify water mass derived from both north and south Pacific Oceans to feed the Indian Ocean (Gordon, 2005). The mixing process occurs in every sill of Indonesian water resulting in low salinity water characteristic of the Indonesian throughflow (ITF) that alters the Indian Ocean (Gordon et al., 2003; Talley and Sprintal, 2005). The ITF originated from both North and South Pacific Water, within the Indonesian sea are modified by vertical tidal mixing, upwelling, air-sea fluxes and freshwater fluxes before being exerted to the Indian Ocean (Ffield and Gordon, 1992; Koch-Larrouy et al., 2007). Intense vertical mixing has been observed particularly at Lifamatola Passage, over the Halmahera sill, the Aru Basin, Seram Sea, and between the Flores and western Banda Sea basins (Talley and Sprintal, 2005 and references therein). The ITF within Indonesian waters also interact with ENSO and Asian monsoon (Gordon and Tillinger, 2010) (Figure 1). As a consequence, a relatively isohaline Indonesian sea profile from the thermocline to near the bottom was formed altering the Indian Ocean (Ffield and Gordon, 1992; Waworuntu et al., 2000; Gordon et al., 2003; Koch-Larrouy et al., 2007).

Arafura, Timor, and the Banda Sea are known to have a high productivity level as sources for major fisheries, due to the upwelling process particularly induced by the northern part of the Sahul continental shelf (Wyrtki, 1961; Ilahude et al., 1990; Atmadipoera et al., 2009; Alongi et al., 2011; Basit et al., 2022). Upwelling in the Arafura Sea is assumed as seasonal coastal upwelling that mostly occurs during the southeast monsoon (Wyrtki, 1961). Southeasterly monsoon wind leads to the westward and southwestward flow of the surface layer, thus colder water that is deeper and rich in nutrients would be upwelled to fill the void in the surface. As a consequence, it provides a large number of nutrients and food for marine organisms so that increases productivity. In contrast, during the Northwest monsoon (December-February), northwesterly wind induces downwelling in the Arafura and Banda Sea that allowing deep ocean oxygenation (>200 m depth), providing dissolve oxygen for benthic organism (van der Zwaan et al., 1990; Basit et al., 2022). In addition to that Arafura Sea is also a part of the Coral Triangle, the epicenter of all marine organism and diversity, Indonesia is considered the largest coral reef area in Southeast Asia (Allen & Werner, 2002; Coral Triangle Initiative, 2014). However, the Arafura Sea is also considered the most endangered tropical coastal and marine ecosystems in the world (Alongi et al., 2011).

The Arafura Sea also provides non-living marine resources, particularly oil and gas resources (e.g. Abadi and Tangguh gas field, Roberts et al., 2011). It is also a part

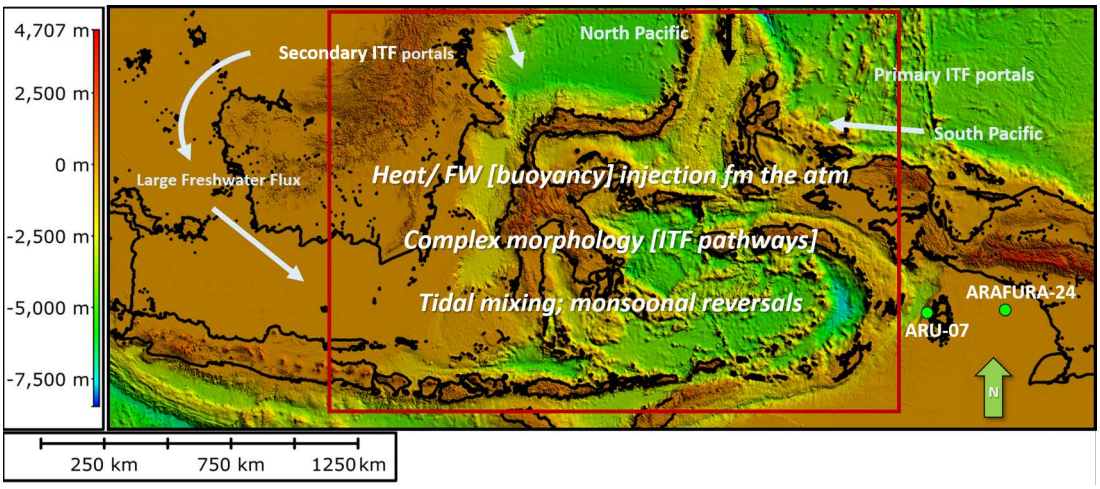

Figure 1. The Indonesian Throughflow routes, western route via South China Sea into Java Sea carrying freshwater altering the ITF in the eastern route at the Banda Sea. Green circle is the sediment core for this study (Modification from Gordon et al., 2005; 2010), on Indonesian bathymetric map (http://batnas.big.go.id/)

of important shipping routes, connecting some Australian ports to the Southeast and Northeast Asian ports, and the northern Pacific Ocean, and a major part of the maritime boundary between Australia, Indonesia, Timor Leste and Papua New Guinea (Alongi et al., 2011). We noticed that the Arafura Sea greatly impacts various aspects, including biodiversity, oceanography, economy and politics, that draw attention from many parties in the world. Therefore, we study marine sediment core from the Arafura Sea, to understand the paleoceanographic condition of eastern Indonesia, by studying PB ratio of marine organisms, particularly foraminifera.

Foraminifera is a single marine organism that exhibits a high response to environmental changes, hence it is a great proxy for paleoceanographic reconstruction and has been widely used in paleoceanography and paleoclimatological study. It is found very abundant in marine sediments, with low cost and simple sample preparation. Geochemistry of foraminiferal shells is the most basic for paleoclimatological proxy, particularly their shells oxygen isotope record which coupled with their Mg/Ca ratio value, may represent seawater temperature and salinity, revealing the air-sea interaction and their correlation to the global climate (e.g. Anand et al., 2008; Elderfield & Ganssen, 2000; Gustiantini, 2018; Hollstein et al., 2017; Zuraida et al., 2009). Furthermore, foraminiferal assemblages also provide comprehensive data for determining paleoceanographic reconstruction. Singh et al. (2017) reconstructed fertility variation in the Sulu Sea from foraminiferal assemblages during 40 kyr BP, resulting in eutrophic conditions during 26 – 17 kyr and Holocene. Ding et al. (2006) revealed significant differences in foraminiferal assemblages group occupying different marine conditions (Java upwelling region, Java – Banda region, Indian monsoon Sumatra region, Timor region, and NW Australian margin region). The previous study of paleoceanographic reconstruction of Arafura Sea derived from foraminiferal assemblages (Gustiantini et al., 2018, will be discussed further later) also resulted in a significantly different group of foraminifera representing distinctive different paleoceanographic condition during older than 3.9 ka BP, 3.9 – 2 ka BP, and younger than 2 ka BP. PB ratio analysis is one statistical analysis of foraminifera that calculate the percentage of planktonic type to the total of benthic and planktonic foraminifera (in %). PB ratio has been known related to water depths (Phleger and parker, 1951; van Marle et al., 1987; van der Zwaan et al., 1990). Furthermore, the PB ratio is also known related to productivity and organic matter flux (Berger and Diester-Haass, 1988; van der Zwaan et al., 1990), and in modern studies, the PB ratio is considered a

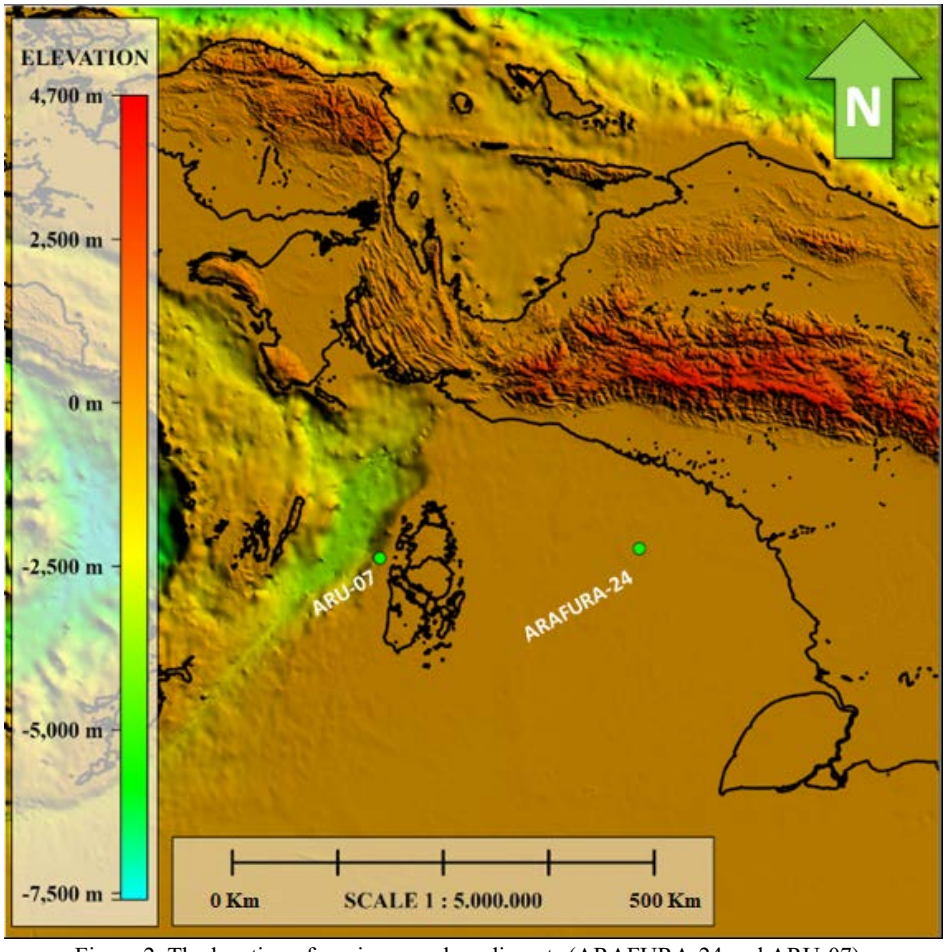

Figure 2. The location of marine sample sediments (ARAFURA-24 and ARU-07)

potential proxy for sea ice indicator (Polyak et al., 2013; Almgren, 2020).

METHODS

This research was analyzed from one marine sediment core ARAFURA-24 (Figure 2). This marine sediment sample was taken from a water depth of 47.4 meters with a core length of 179 cm, located in the northeast of Aru Island, Arafura waters (coordinate of 136° 21' 54.81" E and 5° 49' 38.79" S). The marine sediment core was collected by using a gravity corer on board Geomarin III Vessel in 2017, by the investigation team of the Marine Geological Institute. To have a better comprehension result, we also analyzed marine sediment core ARU-07, which have been collected from nearby location (coordinate of 134° 00' 33.6" E and 5° 55' 51.59" S), from a water depth of 276 meters with a core length of 152 cm, located on the west of Aru Island, Arafura. Foraminiferal assemblages from this marine sediment core has been published (Gustiantini et al., 2018).

Before further analysis, sediment core ARAFURA-24 was sampled at 20 cm intervals using syringe method, which gives a total of 10 subsamples that must be prepared first. The preparatory stage was continued by washing with flowing water and sieved through a 4 phi sieve. Furthermore, the samples were dried at < 60^{o} C temperature for 24 hours. Afterward, we started to pick foraminifera (± 300 individu) from the sample using a binocular microscope, at this stage the separation between foraminifera from other grains was carried out using a small brush. If the sample volumes are too large, the samples were firstly splitted several times until they contained only approximately 300 individu of foraminifera, picked foraminiferal test will be multiplied by the split number afterwards. The number of foraminiferal abundant was then applied to the planktonic benthic ratio (PB ratio) equation:

$$\textbf{PB ratio (\%)} = \textbf{P/(P+B) x 100\%}$$

P = Total Planktonic,

B = Total Benthic.

PB ratio is the planktonic percentage of the total foraminiferal community. PB ratio of foraminifera gives information about seawater depth, which at normal marine conditions, the deep water PB ratio will have a higher value than in shallower water (Table 1).

The geochronology of the sediment was estimated based on radiocarbon AMS ^{14}C dating, analyzed from organic samples collected from 1 sample horizon (163-179cm). It was carried out at the Quaternary laboratory of Center for Geological Survey, Ministry of Energy and Mineral Resources, and has been described in Tim Arafura report (2017).

To refine the age model, we analyzed PB ratio data from sediment core ARU-07, located to the west of the studied core, whose age model has been reconstructed (Gustiantini et al., 2018). The Geochronology of ARU-07 was also estimated based on radiocarbon AMS ^{14}C dating, and also analyzed on organic sediments. The calendar age from ARU-07 was calculated by CALIB 7.0.4 (in 2018, Stuiver et al., 2018, the latest version is Calib 8 which uses the 2020 international dataset), an online software by Stuiver and Reimer (1993) can be downloaded at http://calib.org/calib/download/. This software used the Intcal13 calibration data set (Reimer et al., 2013, in conjunction with Stuiver and Reimer, 1993). Intcal13 is commonly used for the no-marine sample, derived calendar age is presented in Before Present (BP), where "present time" is defined as AD 1950 (Currie, 2004; Reimer et al., 2013). According to the age model, ARU-07 was deposited since the last 8000 BP (Gustiantini et al., 2018).

PB ratio data from this studied core ARAFURA-24 will be correlated to that of the ARU-07 sediment core. We correlated similar events of both PB ratio pattern, to get the age derived from the ARU-07 age model. The calendar age of those similar events will be used as a tie point. Combined with radiocarbon dating data of this core, we further interpolate and extrapolate the age to reconstruct the age model.

Table 1. Environmental Classification based on PB ratio (modified from Grimsdale and Morkhovern, 1955 in Manuhuwa et al., 2021)

PB RATIO	ENVIRONMENT	Depth
< 20 %	Inner Neritic	0 – 50 m
20 – 60 %	Middle Neritic	50 -100 m
40 – 70 %	Outer Neritic	100 – 200 m
> 70%	Upper Bathyal	200 – 1000 m
> 95%	Lower Bathyal	1000 – 1500 m

RESULTS AND DISCUSSION

PB ratio of Foraminifera

The results indicated that the 10 sediment samples of core ARAFURA-24 contained foraminifera with benthic foraminifera type is more abundant and dominant than planktonic foraminifera. The total number of foraminifera obtained from the core sediment of ARAFURA-24 was 8768 individual foraminifera with the number of benthic foraminifera approximately 8468 individuals and the

number of planktonic foraminifera as many as 282 individuals.

Based on the PB ratio calculation of the sediment core ARAFURA-24 (Table 2, figure 3), the minimum value with the percentage of 0.56% occurred at 160 cm depth interval, and at 20 cm depth interval with PB ratio of 1.32%. The maximum value is observed at the top of the core (depth interval 0 cm) with a percentage of 7.43%, at a depth interval of 80 cm (PB ratio 6.55%), and at the bottom of the core (179 cm depth interval) with PB ratio 5.77%. This finding indicates that the depositional environment of the area is an inner neritic marine environment.

Furthermore, PB ratio calculations from 16 samples of core sediment ARU-07 (Table 3, figure 3) show the minimum value of 29.89% at 110 cm depth interval. Another minimum PB ratio value is recognized at 30, 80 and 122 cm depth intervals with PB ratio value of 44.09%, 42.12%, and 41.96% respectively. While the maximum value is observed at a 10 cm depth interval with PB ratio value of 82.66%. Relatively other higher value of PB ratio is identified at three depth intervals, which are the core top (0 cm), 70 cm, and 140 cm, with PB ratio of 67.51%, 65.31%, and 68.8% respectively. This indicates the depositional environment of the area is mostly middle to outer neritic, except the depth interval of 10 cm indicates an upper bathyal marine environment.

Table 2. PB ratio of ARAFURA-24

NO	DEPTH (m)	DEPTH INTERVAL (cm)	PB RATIO (%)	Interpolated AGE (kyr BP)
1	47.4	0	7.43	0
2	47.6	20	1.37	3.28
3	47.8	40	2.6	4.14
4	48	60	2.92	5.0
5	48.2	80	6.55	5.86
6	48.4	100	3.12	6.27
7	48.6	120	1.74	6.67
8	48.8	140	2.12	7.07
9	49	160	0.56	7.47
10	49.19	163-179 (171)	5.77	9,71

Table 3. PB ratio of ARU-07

NO	DEPTH (m)	DEPTH INTERVAL (cm)	PB RATIO (%)	AGE (kyr BP) Gustiantini et al., 2018
1	276	0	67.51	0
2	276.1	10	82.66	2.02
3	276.2	20	53.3	3.28
4	276.3	30	44.09	3.95
5	276.34	34	47.38	4.18
6	276.4	40	58.06	4.51
7	276.5	50	47.56	5.01
8	276.6	60	53.62	5.46
9	276.7	70	65.31	5.86
10	276.8	80	42.12	6.23
11	277	100	45.96	6.87
12	277.1	110	29.89	7.14
13	277.2	120	48.66	7.40
14	277.22	122	41.96	7.45
15	277.4	140	68.8	7.88
16	277.5	150	53.36	8.12

Geochronology

The age result from the radiocarbon dating analysis conducted from intervals 163 - 179 cm of ARAFURA-24 indicates the age of 9710 BP. As mentioned before, we correlated the PB ratio from the studied core to ARU-07 (Figure 4). We correlate similar patterns, that consider

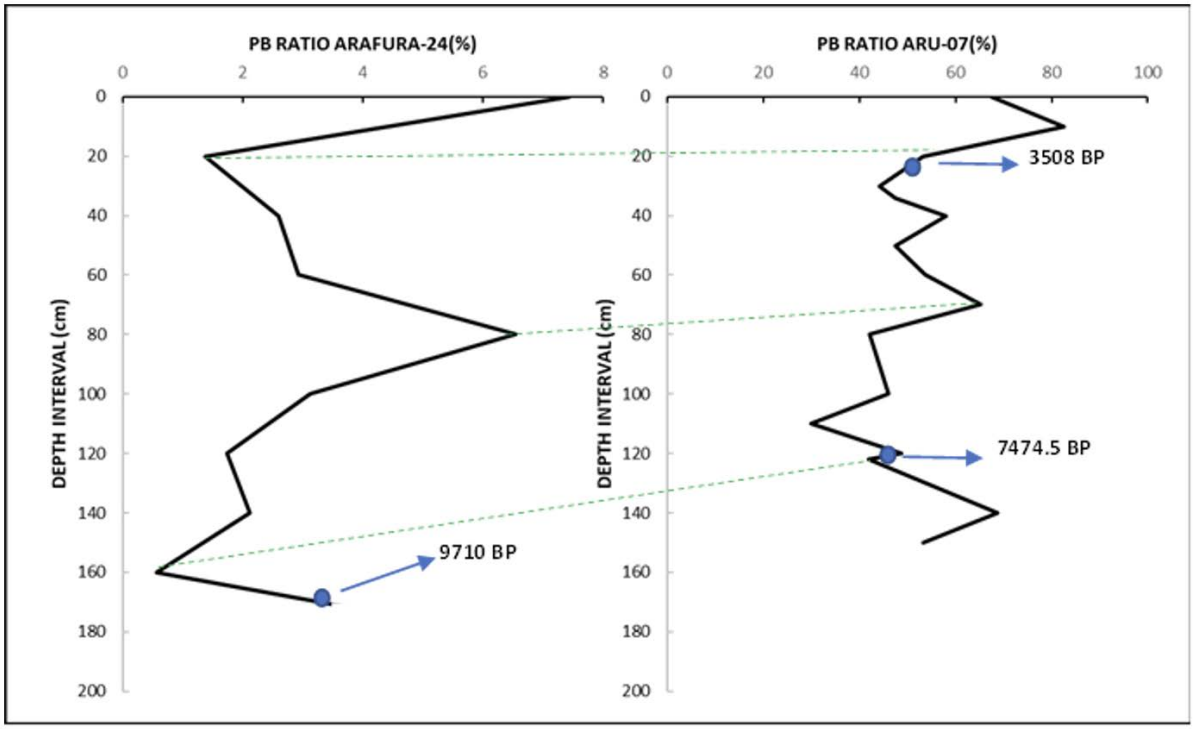

Figure 3. PB ratio versus depth interval at marine sediment core ARAFURA-24 and ARU-07, blue dots are interval sample for 14C dates analysis and the ages are indicated, dash green lines connecting tie points.

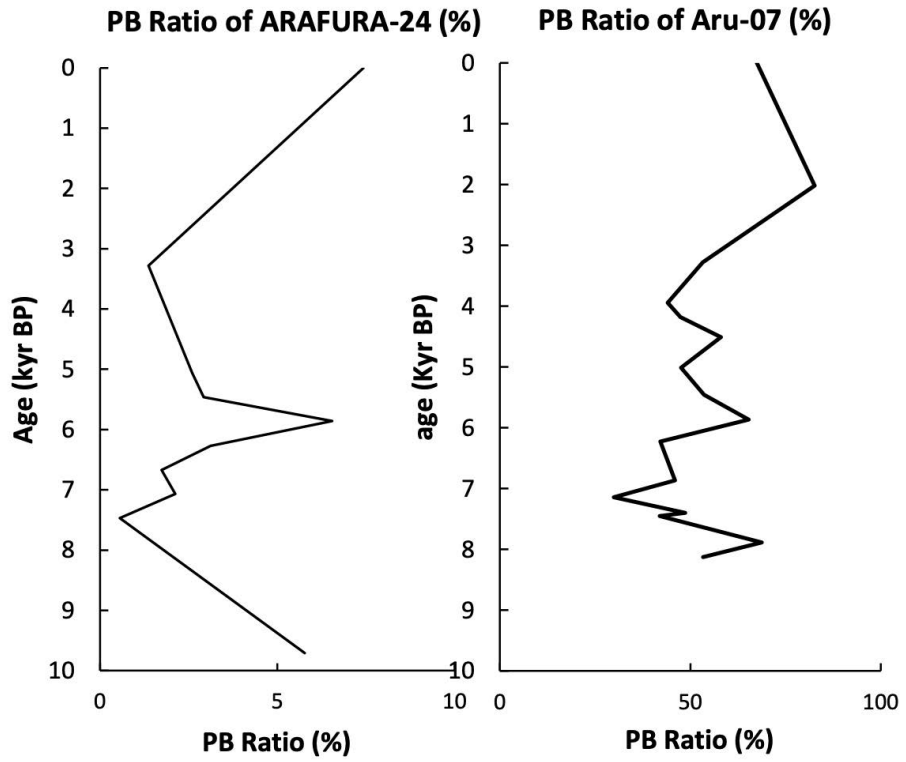

Figure 4. PB ratio of ARAFURA-24 vs interpolated calendar ages, correlated to that of ARU-07

representing similar events as tie points. From the figure, it is observed that intervals 20, 80 and 160 cm of ARAFURA-24 indicate a similar significant increase pattern in PB ratio with that of ARU-07 (interval depths of 20, 70, and 122 cm, respectively). According to ARU-07 calendar age, the age of the 20 cm depth interval is 3.28 kyr BP, depth interval of 80 cm indicates calendar age of 5.8 kyr BP, all tie points are displayed in Table 4. Then the age of the whole interval of the ARAFURA-24 was reconstructed by interpolating and extrapolating depth interval and radiocarbon dating using a linear regression equation (Table 2).

Table 4. Age and sedimentation rate estimation, derived from radiocarbon dating and correlation between ARAFURA-24 and ARU-07

NO	SAMPLE INTERVAL (cm)	CALENDAR AGE (Kyr BP)	REFERENCES	SEDIMENTATION RATE (cm/Kyr BP)
A	20 cm	3.2	Tie point, PB ratio of Aru-07	6.10
B	80 cm	5.86	Tie point, PB ratio of Aru-07	23.21
C	160 cm	7.45	Tie point, PB ratio of Aru-07	50.39
D	171 cm (163 - 179 cm)	9.7	Organic sediment dating	4.87
Average Sedimentation Rate				**21.14**

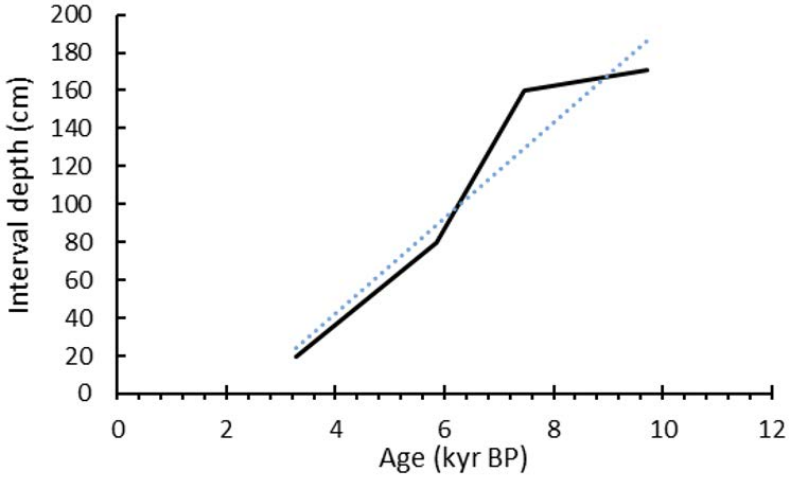

Figure 5. Age model reconstruction of marine sediment at core ARAFURA-24

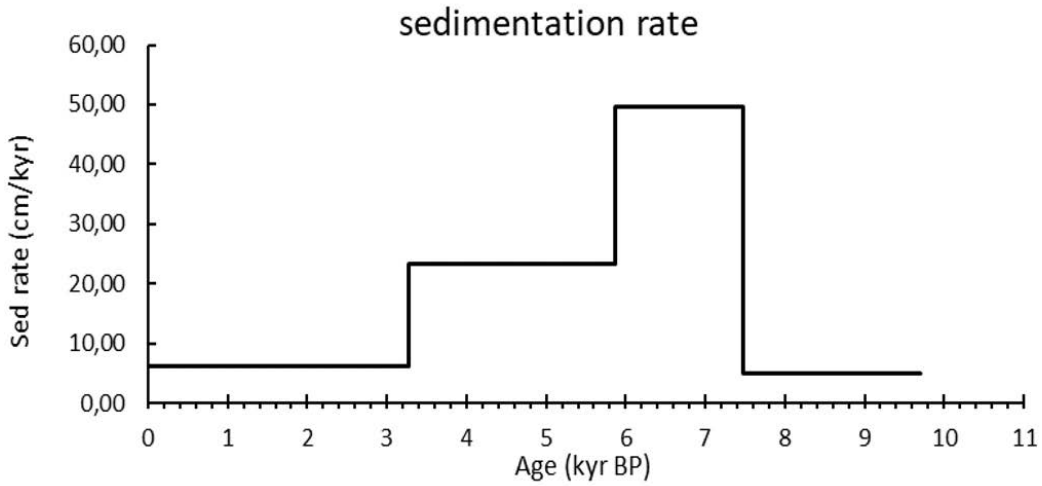

Figure 6. Sedimentation rate of marine sediment at core ARAFURA-24

The age model reconstruction and sedimentation rate estimation reveal that at the age of 3.28 kyr BP the average sedimentation rate was 6.10 cm/Kyr BP, then increased rapidly at 5.86 kyr BP to 23.22 cm/kyr BP. At the age of 7.45 kyr BP the sediment rate was 50.39 cm/kyr and 4.87 cm/kyr in the year 9.71 kyr BP (Table 4, Figure 5 and 6).

DISCUSSION

Marine sample sediment core ARAFURA-24 was acquired at a depth of 47.4 m, categorized as the inner neritic zone, while ARU-07 was classified as a bathyal zone taken at a depth of 276 m. Despite these two marine sediment samples were taken from different zone of water depths leads to different oceanography and marine ecology, both cores demonstrate similar PB ratio and sedimentation rate variability. The distance between the two cores is relatively close (307.3 km), thus both core parameters (particularly PB ratio and sediment geochemistry) apparently preserved the impact of global paleoceanography and paleoclimatic dynamics very well, although some local forcing modified the records. It is observed that before 3.28 kyr BP, the sedimentation rate average of ARAFURA-24 was 26.16 cm/kyr, with distinct slower sedimentation rate before 7.4 kyr BP (sedimentation rate was 4.87 cm/kyr), which is rather similar with that of younger than 3 kyr BP (sedimentation rate was 6.10 cm/kyr). This indicates that the sedimentation rate of ARAFURA-24 after 3.2 kyr BP was relatively slower compared to that before 3.2 kyr BP. This variability is similar to the finding of ARU-07, which indicated a sedimentation rate of 6.56 cm/kyr BP during 3.5 kyr, clearly lower than before 3.5 kyr BP with sedimentation rate of 25.2 cm/kyr BP (Gustiantini et al., 2018). Similar variability of sedimentation rate was also observed from the south of Sumba Islands, as described by Ardi et al. (2021), which revealed relatively slower sedimentation rate (7.602 cm/kyr) at the depth interval 0 – 25 cm (which corresponds to calendar age younger than ~3.2 kyr), compared to that from depth interval samples between 25 – 105 cm (~3.2 kyr – 6.97 kyr) with sedimentation rate 17.28 – 24.8 cm/kyr. Hyun et al. (2018) described that between ~7 – 3 kyr BP in Aru Sea (from similar core used in this study, ARU-07) and in Mahakam Delta were highly influenced by riverine input or influx of terrestrial organic matter, revealed from relatively high CPI (Carbon Preference Index) value, that may be related to paleoclimatic variability.

Another proxy that clearly preserves the impact of similar global paleoceanography and paleoclimatic dynamics of both cores (ARAFURA-24 and ARU-07) is the elemental composition, particularly the log ratio of Ti/Ca (Piranti, in press; and Zuraida et al., in press). We compared both records as displayed in Figure 7. From the figure, both graphs demonstrate relatively coherent variability, which is relative increase down the core. Thus, this data corroborates the hypothesis that global impact clearly influences the two areas and well preserved in the proxy.

Furthermore, we still could reconstruct the sea level changes during the 9 kyr BP, it is observed three times of maximum sea level rises, before 7.4 kyr BP (at 7.8 kyr BP at ARU-07), at 5.82 kyr, and after 3.28 kyr BP

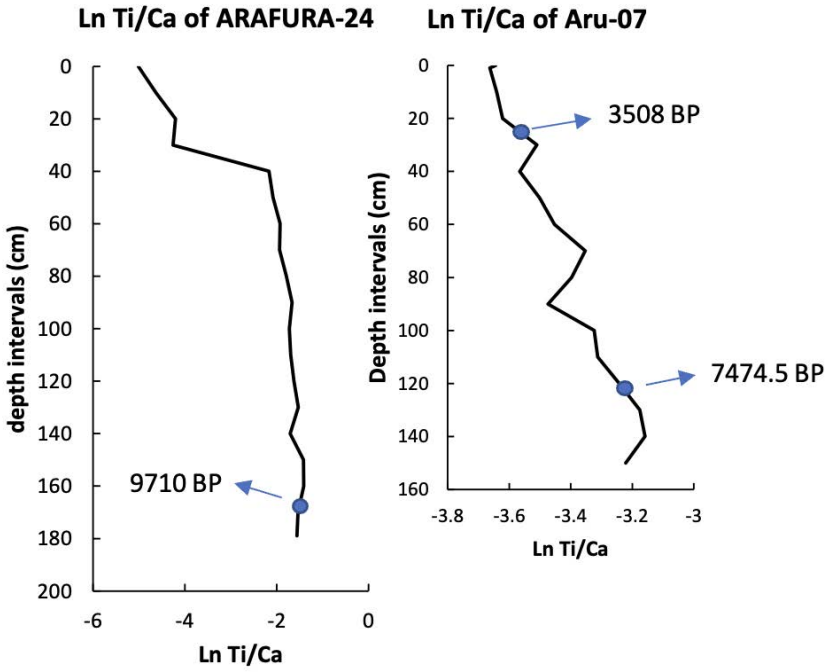

Figure 7. Comparation of elemental proxy (Ln Ti/Ca) from ARAFURA-24 (Piranti, in press) and Aru-07 (Zuraida et al., in press) which demonstrate coherent variability.

(approximately at 2 kyr BP at ARU-07). Significant sea level rise occurred after 3.28 kyr BP which transformed the outer neritic bathymetry zone into a bathyal zone at ARU-07. In contrast, the sedimentation rate decreased after this time and became slower compared to the older time period. This indicates that the sedimentation rate (hence detrital influence) does not significantly impact the PB ratio during Late Holocene, which is mostly more impacted by sea level changes at the Arafura Sea. However, at the time ~7.5 kyr BP, the PB Ratio of Arafura Sea demonstrates relatively abrupt increase trend until ~6 kyr BP, then abruptly decrease up to ~3.2 kyr BP, this pattern displays rather coherent with the increase of sedimentation rate during this interval time. This time interval might represent the warm middle Holocene global climate (Walker et al., 2012). According to Stott et al., (2004) observed from Western Pacific (MD98-2176 at the eastern Banda Sea), during this middle Holocene, particularly before 5 ka, persisted La Niña like condition occurred. NOAA (2021) also reported that sometime during mid-Holocene (7 – 6 ka) the climate was warmer than today.

Van Marle et al.(1987) noted that various parameter influence foraminifera PB ratio, including salinity decrease by river input, turbidity, downslope transport, productivity, sediment accumulation rates, current transport, etc., that might be some factors lead to the discrepancy between paleodepth estimation with the actual water depth. The author described how upwelling leads to nutrient enrichment and could increase planktonic foraminiferal abundance, in contrast this condition might lead to oxygen depletion at the bottom water, which might decrease benthic type abundance. Or vice versa, the upwelling process could increase typical species of benthic that favourable from eutrophic and anoxic conditions (e.g. *Bolivina, Bulimina, Uvigerina*) (e.g. Boltovskoy and Wright, 1976; Jorissen, 1987; Murray, 1991; Bernhard and Sen Gupta, 1999; Fontanier et al., 2003; Martins et al. 2015; etc.), in contrast decrease typical species of planktonic that prefer to live in oligotrophic condition, such as *Globigerinoides ruber* and *Globigerinoides sacculifer* (e.g. Fairbanks et al., 1982; Field D.B., 2004; Ding et al., 2006). Therefore, it is actually will be better to compare the PB ratio analysis result with the study of both benthic and planktonic taxonomy (Van Marle et al., 1987).

CONCLUSIONS

The relatively coherent pattern of the PB ratio of ARAFURA-24 to that of ARU-07 gives us access to be able to reconstruct the age model of ARAFURA-24 by correlating tie points of similar events combined with dating data from both cores. Therefore, we are very optimistic with our age models, however further analysis is necessary to get a better result of age model reconstruction.

PB ratio result indicates three times of maximum sea level rises, which are before 7.4 kyr BP (at 7.8 kyr BP at ARU-07), at 5.86 kyr, and after 3.28 kyr BP (approximately at 2 kyr BP at ARU-07). While sedimentation rate reconstruction exhibits a slower rate value after 3.28 kyr BP compared to that of the older time period. Thus, it can be concluded that during Late Holocene, the sedimentation rate (hence detrital influence) does not significantly impact the foraminiferal PB ratio at the Arafura Sea. Furthermore, during Mid-Holocene, sedimentation rate more influence foraminiferal PB ratio.

ACKNOWLEDGEMENTS

We would like to thank the team members of Arafura and Aru surveys for acquiring these marine sediment cores and other data. Our gratitude to the Captain and crew of vessel Geomarin III. We also acknowledge the MGI staff in Cirebon and Bandung who assisted in sample preparation. This study would not have been realized without the contribution and support of the Director of the Marine Geological Institute. This study was funded by Marine Geological Institute of Indonesia and Korea Institute of Ocean Science and Technology (Kiost).

REFERENCES

Allen, G.R., & Werner, T.B., 2002. Coral reef fish assessment in the “coral triangle” of southeastern Asia. *Environmental Biology of Fishes*, 65(2): 209–214. https://doi.org/10.1023/A:1020093012502.

Almgren, A., 2020. Comparing planktonic-to-benthic (P/B) ratio signals to modern sea ice proxies at the Yermak Plateau, Arctic Ocean, during the last 160 ka. Stockholm universitet. Stockholms, Sweden. *Unpublished Master’s Thesis*.

Alongi, D.M., Edyvane, K., do Ceu Guterres, M.O., Pranowo, W.S., Wirasantosa, S., & Wasson, R., 2011. *Biophysical Profile of the Arafura and Timor Seas Report for the Transboundary Diagnostic Analysis component of the Arafura and Timor Seas Ecosystem Action Program*. 32.

Anand, P., Elderfield., H., and Conte, M.H., 2003. Calibration of Mg/Ca thermometry in planktonic foraminifera from a sediment trap time series, *Paleoceanography*, 18 (2): 15p. 1050, doi:10.1029/2002PA000846.

Atmadipoera A.R, Molcard, G., Madec, S., Wijffels, J., Sprintall, A., Koch-Larrouy, I., Jaya, and Supangat, A., 2009. Characteristics and variability of the Indonesian throughflow water at the Outflow Straits. Deep-Sea Res. I, 56(1): 1942–1954.

Ardi, R.D.W., Aswan, Maryunani, K.A., Yulianto E., Putra, P.S., and Nugroho, S.H., 2021. Changes of Thermocline Depth at the Sumba Island Offshore

Based on Planktonic Foraminiferal Assemblages and Its Implication to Eutrophication since the Last Deglaciation (~18 Ka Bp): A Preliminary Study. *Rudarsko Geolosko Naftni Zbornik,* 36 (3): 31–45. https://doi.org/10.17794/rgn.2021.3.3.

Basit, A., Mayer, B., & Pohlmann, T., 2022. The Effects of the Indonesian Throughflow, River, and Tide on Physical and Hydrodynamic Conditions During the Wind- Driven Upwelling Period North of the Aru Islands. *Pertanika Journal of Science and Technology*, 30(2): 1689–1716. https://doi.org/10.47836/pjst.30.2.45.

Berger, W.H., Diester-Haass, L., 1988. Paleoproductivity: The benthic/planktonic ratio in foraminifera as a productivity index, *Marine Geology*,81(1-4): 15-25.

Bernhard, J.M. and Sen Gupta, B.K., 1999. Foraminifera in Oxygen-Depleted Environments. In: Sen Gupta, B.K., Ed., *Modern Foraminifera*, Kluwer, Dordrecht, 201-216.http://dx.doi.org/10.1007/0-306-48104-9_12.

Boltovskoy, E. and Wright, R., 1976. *Recent foraminifera*, Dr. W. Junk, The Hague, Boston, 515p.

Coral Triangle Initiative CTI-CFF., 2014. *State of the Coral Triangle: Indonesia. Manila: Asian Development Bank.*

Currie, L.A., 2004. The remarkable metrological history of radiocarbon dating [II]*, Journal of Research of the National Institute of Standards and Technology*, 109(2): 185-217.

Ding, X., Bassinot, F., Guichard, F., Li, Q.Y., Fang, N.Q., Labeyrie, L., Xin, R.C., Adisaputra, M.K., and Hardjawidjaksana, K., 2006. Distribution and ecology of planktonic foraminifera from the seas around the Indonesian Archipelago, *Marine Micropaleontology*, 58: 114– 134.

Elderfield, H., & Ganssen, G., 2000. Past temperature and $\delta^{18}O$ of surface ocean waters inferred from foraminiferal Mg/Ca ratios. *Nature*, 405(6,785): 442–445. https://doi.org/10.1038/35013033.

Fairbanks, R. G., 1982. The origin of continental shelf and slope water in the New York Bight of Maine: Evidence from $H_2{}^{18}O/H_2{}^{16}O$ ratio measurements. *Journal of Geophysical Research*, 87(C8), 5796–5808. https://doi.org/10.1029/JC087iC08p05796

Ffield, A., and Gordon, A.L., 1992. Vertical mixing in the Indonesian thermocline. *Journal of Physical Oceanography,* 22 (2): 184–195.

Field, D.B., 2004: Variability in vertical distributions of planktonic foraminifera in the California Current: Relationships to vertical ocean structure, *Paleoceanography* 19: 1 – 22.

Fontanier, C., Jorissen, F.J., Chaillou, G., David, C., Anschutz, P., and Lafon, V., 2003. Seasonal and interannual variability of benthic foraminiferal faunas at 550 m depth in the Bay of Biscay. *Deep-Sea Res*. I, 50: 457–494.

Gordon, A. L., 2005. Oceanography of the Indonesian seas and their throughflow. *Oceanography*, 18: 14-27. https://doi.org/10.5670/oceanog.2005.0

Gordon, A. L. & Tillinger, D., (2010). Transport weighted temperature and internal energy transport of the Indonesian throughflow. *Dynamics of Atmospheres and Oceans*, 50(2): 224–232. doi: 10.1016/j.dynatmoce.2010.01.002

Gordon, A. L., Giulivi, C.F., and Ilahude, A.G. 2003. Deep topographic barriers within the Indonesian seas, *Deep Sea Res*., *Part II*, 50: 2205 – 2228.

Gustiantini, L., Piranti, S.A., Zuraida, R., Hyun, S., Ranawijaya, D.A. S., & Prabowo, F. X. H. H., 2018. Foraminiferal Analysis Related to Paleoceanographic Changes of Arafura Sea and Surrounding during Holocene. *Bulletin of the Marine Geology*, 33(2): 105–118. https://doi.org/10.32693/bomg.33.2.2018.571.

Hollstein, M., Mohtadi, M., Rosenthal, Y., Moffa Sanchez, P., Oppo, D., Martínez-Méndez, G., Steinke, S., & Hebbeln, D., 2017. Stable oxygen isotopes and Mg/Ca in Planktonic foraminifera from modern surface sediments of the Western Pacific Warm Pool: Implications for thermocline reconstructions. *Paleoceanography*, 32:1174–1194. https://doi.org/10.1002/2017PA003122.

http://batnas.big.go.id/, accessed, in 2022.

http://calib.org/calib/download/, accessed in 2018.

Hyun, S., Zuraida, R., and Ranawijaya, D.A., 2018. Carbon Isotope and n -Alkanes Records from the Nearby Mahakam Delta and Arafura Sea, Indonesia: Implications of Holocene Paleoenvironmental Changes, *Poster session at 9th ICAMGS21-PO2-A2266*.

Ilahude, A.G., Komar, & Mardanis, 1990. On the hydrology and productivity of the northern Arafura Sea. *Netherlands Journal of Sea Research*, 25(4): 573-582. https://doi.org/10.1016/0077-7579(90)90079-V.

Jorissen, F.J., 1987. The distribution of benthic foraminifera in the Adriatic Sea*, Marine Micropaleontology*, 12: 21-48.

Koch-Larrouy, A., Madec, G., Bouruet-Aubertot, P., Gerkema, T., Bessières, L., & Molcard, R., 2007. On the transformation of Pacific water into Indonesian throughflow water by internal tidal mixing. *Geophysical Research Letters*, 34(4): 1-6. http://dx.doi.org/10.1029/ 2006GL028405.

Martins, M.V.A., Quintino, V., Tentúgal, R.M., Frontalini, F., Miranda, P., Laut, L.L.M., Martins, R., and Rodrigues, A.M., 2015. Characterization

of bottom hydrodynamic conditions on the Central Western Portuguese Continental Shelf based on benthic foraminifera and sedimentary parameters, *Marine Environmental Research*, 109: 52-68.

Murray, J.W., 1991. *Ecology and palaeoecology of benthic foraminifera.* Longman Scientific and Technical, London. 397 pp.

NOAA, 2021. Paleoclimate Data Before 2,000 Years Ago, *NOAA National Centers For Environmental Information*. ncei.noaa.gov/products/paleoclimatology/paleo-perspectives. Downloaded in Oct. 2021.

Phleger, F.B., and Parker, F.L., 1951. Foraminiferal Distribution, Pt. l, Ecology of Foraminifera, Northwest Gulf of Mexico, *The Geological Society of American Memoir*, 46: 88p.

Polyak, L., Lazar, K.B., Crawford, K.A., Council, E., & St-Onge, G., 2013. Quaternary history of sea ice in the western Arctic Ocean based on foraminifera. *Quaternary Science Reviews*, 79. 10.1016/j.quascirev.2012.12.018.

Reimer, P.J., Bard, E., Bayliss, A., Beck, J.W., Blackwell, P.G., Bronk Ramsey, C., Buck, C.E., Cheng, H., Edwards, R.L., Friedrich, M., Grootes, P.M., Guilderson, T.P., Haflidason, H., Hajdas, I., Hatté, C., Heaton, T.J., Hogg, A.G., Hughen, K.A., Kaiser, K.F., Kromer, B., Manning, S.W., Niu, M., Reimer, R.W., Richards, D.A., Scott, E.M., Southon, J.R., Turney, C.S.M., and van der Plicht, J., 2013. IntCal13 and MARINE13 radiocarbon age calibration curves 0-50000 years calBP, *Radiocarbon*, 55 (4): DOI: 10.2458/azu_js_rc.55.16947.

Roberts, G., Ramsden, C., Christoffersen, T., Wagimin, N., and Muzaffar, Y., 2011. East Indonesia: Plays and Prospectivity of the West Aru, Kai Besar and Tanimbar Area - Identified from New Long Offset Seismic Data, *expanded abstract presentation at AAPG Annual Convention and Exhibition*, Houston, Texas, USA, April 10-13, 2011.

Singh, V., Singh, A.K., Sinha, D.K., & Mallick, K.R., 2017. Planktonic Foraminifera as Indicators of Paleoceanographic Changes in The Sulu Sea During Late Quaternary. *VISTAS IN GEOLOGICAL RESEARCH (ISBN: 81-900907-0-4) U.U. Special Publication in Geology,* 15:132-139.

Stott, L., Cannariato, K., Thunell, R., Haug, G.H., Koutavas, A., and Lund, S., 2004. Decline of Surface Temperature and Salinity in the Western Tropical Pacific Ocean in the Holocene Epoch. *Nature* 431 (7004): 56–59. 13 of https://doi.org/10.1038/nature02903.

Stuiver, M. and Reimer, P.J., 1993. Extended ^{14}C database and revised CALIB radiocarbon calibration program, *Radiocarbon*, 35: 215-230.

Stuiver, M., Reimer, P.J., and Reimer, R.W. 2018. CALIB 7.1 [WWW program] at http://calib.org, accessed 2018-4-10.

Talley, L.D., & Sprintall, J., 2005. Deep expression of the Indonesian Throughflow: Indonesian Intermediate Water in the South Equatorial Current. *Journal of Geophysical Research*: Oceans, 110(10): 1-30. https://doi.org/10.1029/2004JC002826.

Tim Arafura., 2017. *Laporan Penelitian Cekungan dan Pengembangan Model Geologi Hidrokarbon Untuk Mendukung Wilayah Kerja Migas di Wilayah Perairan Arafura Papua*, *Internal Report of Marine Geological Institute*, Ministry of Energy and Mineral Resources Republic of Indonesia. *Unpublished.*

Van der Zwaan, G. J., Jorissen, F.J., and de Stigter, H.C., 1990. The Depth Dependency of Planktonic/Benthic Foraminiferal Ratios: Constraints and Applications. *Marine Geology,* 95 (1): 1–16. https://doi.org/10.1016/0025-3227(90)90016-D.

Van Marle, L. J., Van Hinte, J. E., & Nederbragt, A. J., 1987. Plankton percentage of the foraminiferal fauna in seafloor samples from the Australian-Irian Jaya continental margin, eastern Indonesia. *Marine Geology*, 77(1–2): 151–156. https://doi.org/10.1016/0025-3227(87)90089-2.

Walker, M.J.C., Berkelhammer, M., Björck, S., Cwynar, L.C., Fisher, D.A., Long, A.J., Lowe, J.J., Newnham, R.M., Rasmussen, S.O., and Weiss, H., 2012. Formal Subdivision of the Holocene Series/Epoch: A Discussion Paper by a Working Group of INTIMATE (Integration of Ice-Core, Marine and Terrestrial Records) and the Subcommission on Quaternary Stratigraphy (International Commission on Stratigraphy). *Journal of Quaternary Science* 27 (7): 649–59. https://doi.org/10.1002/jqs.2565.

Waworuntu, J., Fine, R., Olson, D., Gordon, A.L., 2000. Recipe for Banda Sea water. *Journal of Marine Research* 58: 547–569.

Wyrtki, K., 1961. Scientific results of marine investigations of the South China Sea and the Gulf of Thailand 1959-1961, *Naga Report vol. 2. The University of California press*. https://doi.org/10.1017/S0025315400054370.

Zuraida, R., Holbourn, A., Nürnberg, D., Kuhnt, W., Dürkop, A., and Erichsen, A., 2009. Evidence for Indonesian Throughflow slowdown during Heinrich events 3–5, *Paleoceanography*, 24: 1 – 15.

Guide for Authors - Geoscience Publications
Bulletin of the Marine Geology

Writing should be submitted according to the following restrictions:

1. Manuscript should be written in English and be submitted online via journal website http://ejournal.mgi.esdm.go.id. Online Submission will be free. The author must login in order to make submission.
2. Manuscript should contains at least 2.000 words and at least 8 pages of manuscript that including embedded figures and tables, without any appendix, and the file should be in Microsoft Office (.doc/.docx) format. It should be prepared in A4 paper (21cm x 29.7cm) using 2.5 cm for left and right margins and 2 cm for top and bottom margins, additionally the paragraph should be used 1 line spacing, 11 TNR.
3. Title, Abstract, and Keywords should be written in English
   - Abstract should be written in English and Bahasa Indonesia version
   - Title should be less than 15 words, title case, small caps, centered, bold, font type Times New Roman (TNR), font size 16, and single spaced.
   - Abstract contains neither pictures nor tables, justified, in 11 TNR, single spaced, and should not exceed 250 words.
   - Keywords contain four to six words/phrases separated with coma and should be justified, 10 TNR and single spaced.
   - Please provide all email address of all authors for our database concern, however, in the published version, only the email address of the first author will be appeared.
4. Manuscript body consists of: Introduction, Method, Result, Discussion, and Conclusion completed by Acknowledgment and References in capital and bold.
5. Heading should be made in four levels. Level five cannot be accepted.
   - Heading 1: title caps, left aligned, bold, 14 TNR, single spaced
   - Heading 2: title case, left aligned, bold, 11 TNR, single spaced
   - Heading 3: title case, left aligned, italic, 11 TNR, single spaced
   - Heading 4 is not recommended, however, it could still be accepted with the format of: sentence case, left indent 5 mm, hanging indent 5 mm, italic, 11 TNR, single spaced
   - Heading 5 cannot be accepted in the manuscript.
6. Figure and table can be either in black and white or in color, they should be clearly readable and in a proportional measure to the overall page. Caption should be numbered, in 9 TNR and single spaced. For lay outing purpose, please provide the respective captioned figure/table with extension .tif/.jpg/.jpeg within a particular folder apart from the manuscript. Please note the figure source/citation/reference if it is taken and/or modified from previous publication.
7. Mathematical equation should be clearly written, numbered orderly, and accompanied with any information needed.
8. Header and footer including page number must not be used. All hypertext links and section bookmarks will be removed from papers. If you need to refer to an Internet email address or URL in your paper, you must type out the address or URL fully in Regular font.
9. Citation and Reference. Following are the detail organization of the references guidelines:
   a. References are written in alphabetical order according to the family name of the first author.
   b. If there is more than one references made by similar author, References are arranged in order of time, and then in alphabetical order.
   c. All the references should be cited in the text. In the text, reference is cited with author family name and the year of publication. If it is written by 2 authors, the family name of both authors are noted, followed by the year of publication, if it is written by more than 2 authors, the reference is cited with the first author family name, followed by *et al.,* and the year of publication. For example: (Kennett, 1981); (Usman and Panuju, 2013); (Susilohadi *et al.*, 2009). Several references are written in alphabetical order, for example: (Kennett, 1981; Susilohadi *et al.,* 2009; and Usman and Panuju, 2013).
   d. References are consist of paper, proceeding, or book that are published, or unpublished report including internal report, dissertation, or thesis.
   e. References can be taken from website, by writing the hyperlink, and the time when it is accessed. Wikipedia, personal blog, or non scientific website is not allowed to be taken into account.

f. References should be ten references in minimum, at least two of them were published in the last five years.

g. Only the family name of the authors are written, followed by the abbreviation of their first name and middle name (if available). If the reference is written by more than one author, all authors should be written, abbreviation (e.g. dkk, *et al,* or drr) is not allowed..

h. All the information of the references must be noted, including publisher, journal volume, number (if available), and page number.

- For book, the book title should be written in italic, for example:

  Kennett, J.P., 1981. *Marine Geology.* Prentice Hall, 813p.

- For periodicals, the name of the journal should be written in italic, for example:

  Susilohadi, S., Gaedicke, C., and Djajadihardja, Y.S., 2009. Structures and sedimentary deposition in the Sunda Strait, Indonesia, *Tectonophysics,* 467 (1): 55-71.

- (Tectonophysics is the name of the journal, 467 is the volume, 1 is issued number, 55 – 71 is page number)

  Usman, E., and Panuju, 2013. Study of Gas Potency Based on Gravity Anomaly Modeling And Seismic Profile Analysis at Banggai-Sula Basin. *Bulletin of the Marine Geology,* 28 (2): 51-60.

- For edited symposia, special issues, etc. published in periodical:

  Kenneth, S. J., 2009. Marine biogeochemistry in 2025. In: D. Glickson (Editor), *Oceanography in 2025: Proceedings of a workshop.* The National Academic Press, Washington D. C.: 130 – 134.

- For websites:

  <http://palaeo-electronica.org/2003_1/benthic/issue1_03.htm> [Accessed on 30 November 2011].

- Unpublished references:

  Darlan, Y., Kamiludin, U., Kurnio, H., Rahardian, R., Hutagaol, J. P., Sianipar, A. H., and Sinaga, A. C., 2005. *Eksplorasi prospektif gas biogenik kelautan di Perairan Muara Kakap dan sekitarnya - Kalimantan Barat.* Pusat Penelitian dan Pengembangan Geologi Kelautan, Bandung, Badan Penelitian dan Pengembangan Energi dan Sumberdaya Mineral, Departemen Energi dan Sumberdaya Mineral. Internal report, 104p. Unpublished.

SERTIFIKAT

Direktorat Jenderal Penguatan Riset dan Pengembangan,
Kementerian Riset, Teknologi, dan Pendidikan Tinggi

RISTEKDIKTI

Kutipan dari Keputusan Direktur Jenderal Penguatan Riset dan Pengembangan,
Kementerian Riset, Teknologi, dan Pendidikan Tinggi Republik Indonesia
Nomor: 21/E/KPT/2018, Tanggal 9 Juli 2018
Tentang Hasil Akreditasi Jurnal Ilmiah Periode I Tahun 2018

Nama Jurnal Imiah

Bulletin of the Marine Geology

E-ISSN: 2527-8843
Penerbit: Puslitbang Geologi Kelautan, Kementerian ESDM

Ditetapkan sebagai Jurnal Ilmiah

TERAKREDITASI PERINGKAT 2

TERAKREDITASI

Akreditasi berlaku selama 5 (lima) tahun, yaitu
Volume 31 Nomor 1 Tahun 2016 sampai Volume 35 Nomor 2 Tahun 2020

Jakarta, 9 Juli 2018
Direktur Jenderal Penguatan Riset dan Pengembangan

Dr. Muhammad Dimyati
NIP. 195912171984021001

MARINE GEOLOGICAL INSTITUTE

GEOLOGICAL AGENCY
MINISTRY OF ENERGY AND MINERAL RESOURCES

Jl. Dr. Djunjunan No. 236, Bandung - 40174. Indonesia
http://www.mgi.esdm.go.id, Email : ejournal.p3gl@gmail.com